

THESIS FOR THE DEGREE OF DOCTOR OF PHILOSOPHY

Microscopic Theory of Charge Complexes in Atomically-Thin Materials

Raul Perea-Causin

Department of Physics

CHALMERS UNIVERSITY OF TECHNOLOGY

Göteborg, Sweden 2023

Microscopic Theory of Charge Complexes in Atomically-Thin Materials
Raul Perea-Causin

© Raul Perea-Causin, 2023.

ISBN 978-91-7905-877-7

Doktorsavhandlingar vid Chalmers tekniska högskola. Ny serie nr 5343

ISSN 0346-718X

Department of Physics
Chalmers University of Technology
SE-412 96 Göteborg Sweden
Telephone + 46 (0)31-772 1000

Cover: Artistic illustration of charge complexes formed by electrons and holes in an atomically-thin material.

Chalmers digitaltryck
Göteborg, Sweden 2023

Microscopic Theory of Charge Complexes in Atomically-Thin Materials

Raul Perea-Causin

Department of Physics

Chalmers University of Technology

Abstract

Atomically-thin materials have emerged as the most promising two-dimensional platform for future optoelectronic applications and for the study of quantum many-body physics. In particular, transition metal dichalcogenides (TMDs) exhibit strong Coulomb interaction, resulting in the formation of tightly-bound electron-hole complexes that dominate optics, dynamics, and transport. In the neutral regime, excitons—bound electron-hole pairs—constitute the dominating many-particle species from low to moderate photoexcitation densities. In the presence of doping, however, excitons can bind to additional charges and form trions. In order to achieve an efficient and controllable implementation of TMDs in novel devices, understanding the fundamental properties of excitons and trions in these materials is crucial.

The aim of this thesis is to provide a microscopic understanding of the underlying many-particle mechanisms in TMD optoelectronic devices. Based on the density-matrix formalism, we describe the dynamics in a system of interacting electrons, holes, phonons, and photons. We model the excitonic features of optical absorption spectra and reveal how they are influenced by the excitation density. We unveil the formation dynamics of dark excitons after photoexcitation and resolve the main pathways of phonon-assisted dissociation. Furthermore, we tackle exciton diffusion, tracing the emergence of photoluminescence halos back to the large heating and thermal drift of excitons at strong excitation. Finally, we consider doped TMDs and investigate the trion dynamics, including diffusion and photoluminescence. In particular, we predict so far unobserved luminescence signatures that could shed light on the internal structure of trions.

Overall, this work provides microscopic insights into many-particle processes governing the optics, dynamics, and transport in atomically thin semiconductors.

Keywords: excitons, trions, phonons, 2D materials, many-body physics, propagation, dynamics, dissociation, photoluminescence.

List of publications

This thesis consists of an introductory text and the following papers:

- I. **Exciton propagation and halo formation in two-dimensional materials**
R. Perea-Causín, S. Brem, R. Rosati, R. Jago, M. Kulig, J. D. Ziegler, J. Zipfel, A. Chernikov, E. Malic
 Nano Letters 19 (10), 7317 (2019)
- II. **Microscopic modeling of pump–probe spectroscopy and population inversion in transition metal dichalcogenides**
R. Perea-Causín, S. Brem, E. Malic
 Physica status solidi (b) 257, 2000223 (2020)
- III. **Momentum-resolved observation of exciton formation dynamics in monolayer WS₂**
 R. Wallauer, **R. Perea-Causin**, L. Münster, S. Zajusch, S. Brem, J. Gütde, K. Tanimura, K. Lin, R. Huber, E. Malic, U. Höfer
 Nano Letters 21 (13), 5867 (2021)
- IV. **Phonon-assisted exciton dissociation in transition metal dichalcogenides**
R. Perea-Causín, S. Brem, E. Malic
 Nanoscale 13, 1884 (2021)
- V. **Trion-phonon interaction in atomically-thin semiconductors**
R. Perea-Causin, S. Brem, E. Malic
 Physical Review B 106, 115407 (2022)
- VI. **Trion photoluminescence and trion stability in atomically thin semiconductors**
R. Perea-Causin, S. Brem, O. Schmidt, E. Malic
 In manuscript (2023)

My contribution to the appended publications

As first author in papers I-II and IV-VI, I developed the theoretical model, performed the numerical evaluations, analyzed the results and wrote the manuscripts with the aid of my main supervisor. In paper III, I developed the theoretical model, performed the numerical evaluations, and analyzed

the results as the leading theory author.

Publications not appended in this thesis:

- VIII. **Spatio-temporal dynamics in graphene**
R. Jago, **R. Perea-Causin**, S. Brem, and E. Malic
Nanoscale 11, 10017 (2019)
- IX. **Negative effective excitonic diffusion in monolayer transition metal dichalcogenides**
R. Rosati, **R. Perea-Causin**, S. Brem, E. Malic
Nanoscale 12, 356 (2020)
- X. **Exciton diffusion in monolayer semiconductors with suppressed disorder**
J. Zipfel, M. Kulig, **R. Perea-Causin**, S. Brem, J. D. Ziegler, R. Rosati, T. Taniguchi, K. Watanabe, M. M. Glazov, E. Malic, A. Chernikov
Physical Review B 101, 115430 (2020) [editor's suggestion]
- XI. **Temporal evolution of low-temperature phonon sidebands in transition metal dichalcogenides**
R. Rosati, K. Wagner, S. Brem, **R. Perea-Causin**, E. Wietek, J. Zipfel, J. D. Ziegler, M. Selig, T. Taniguchi, K. Watanabe, A. Knorr, A. Chernikov, E. Malic
ACS Photonics 7 (10), 2756 (2020)
- XII. **Microscopic picture of electron-phonon interaction in two-dimensional halide perovskites**
D. Feldstein, **R. Perea-Causin**, S. Wang, M. Dyksik, K. Watanabe, T. Taniguchi, P. Plochocka, E. Malic
The Journal of Physical Chemistry Letters 11 (23), 9975 (2020)
- XIII. **Strain-dependent exciton diffusion in transition metal dichalcogenides**
R. Rosati, S. Brem, **R. Perea-Causin**, R. Schmidt, I. Niehues, S. M. de Vasconcellos, R. Bratschitsch, E. Malic
2D Materials 8, 015030 (2021)
- XIV. **The art of constructing black phosphorus nanosheet based heterostructures: from 2D to 3D**

S. Thurakkal, D. Feldstein, **R. Perea-Causin**, E. Malic, X. Zhang
Advanced Materials 33, 2005254 (2021)

- XV. **Microscopic understanding of ultrafast charge transfer in van der Waals heterostructures**
R. Krause, S. Aeschlimann, M. Chavez-Cervantes, **R. Perea-Causin**, S. Brem, E. Malic, S. Forti, F. Fabbri, C. Coletti, I. Gierz
Physical Review Letters 127, 276401 (2021)
- XVI. **Dark exciton anti-funneling in atomically thin semiconductors**
R. Rosati, R. Schmidt, S. Brem, **R. Perea-Causin**, I. Niehues, J. Kern, J. Preuß, R. Schneider, S. M.de Vasconcellos, R. Bratschitsch, E. Malic
Nature Communications 12, 7221 (2021)
- XVII. **Non-classical exciton diffusion in monolayer WSe₂**
K. Wagner, J. Zipfel, R. Rosati, E. Wietek, J. D. Ziegler, S. Brem, **R. Perea-Causin**, T. Taniguchi, K. Watanabe, M. M. Glazov, E. Malic, A. Chernikov
Physical Review Letters 127, 076801 (2021) [editor's suggestion]
- XVIII. **Non-equilibrium diffusion of dark excitons in atomically thin semiconductors**
R. Rosati, K. Wagner, S. Brem, **R. Perea-Causin**, J. D. Ziegler, J. Zipfel, T. Taniguchi, K. Watanabe, A. Chernikov, E. Malic
Nanoscale 13, 19966 (2021)
- XIX. **Dark exciton-exciton annihilation in monolayer transition-metal dichalcogenides**
D. Erkensten, S. Brem, K. Wagner, R. Gillen, **R. Perea-Causin**, J. D. Ziegler, J. Maultzsch, A. Chernikov, E. Malic
Physical Review B 104, L241406 (2021) [editor's suggestion]
- XX. **Ultrafast nanoscopy of high-density exciton phases in WSe₂**
T. Siday, F. Sandner, S. Brem, M. Zizlsperger, **R. Perea-Causin**, F. Schiegl, S. Nerreter, M. Plankl, P. Merkl, F. Mooshammer, M. A. Huber, E. Malic, and R. Huber
Nano Letters 22 (6), 2561 (2022) [on the cover]
- XXI. **Microscopic origin of anomalous interlayer exciton transport in van der Waals heterostructures**

D. Erkensten, **R. Perea-Causin**, S. Brem, E. Malic
Physical Review Materials 6, 094006 (2022)

- XXII. **Exciton optics, dynamics, and transport in atomically thin semiconductors**
R. Perea-Causin, D. Erkensten, J. M. Fitzgerald, J. J. P. Thompson, R. Rosati, S. Brem, E. Malic
APL Materials 10, 100801 (2022) [featured]
- XXIII. **Flat-band-induced many-body interactions and exciton complexes in a layered semiconductor**
G. Pasquale, Z. Sun, K. Cernevs, **R. Perea-Causin**, F. Tagarelli, K. Watanabe, T. Taniguchi, E. Malic, O. V. Yazyev, A. Kis
Nano Letters 22 (22), 8883 (2022)
- XXIV. **Electrical control of hybrid exciton transport in a van der Waals heterostructure**
F. Tagarelli, E. Lopriore, D. Erkensten, **R. Perea-Causin**, S. Brem, J. Hagel, Z. Sun, G. Pasquale, K. Watanabe, T. Taniguchi, E. Malic, A. Kis
Nature Photonics (2023)
- XXV. **Ultrafast hot electron-hole plasma photoluminescence in two-dimensional semiconductors**
F. B. Sousa, **R. Perea-Causin**, S. Brem, S. Hartman, L. Lafeta, B. Rosa, S. Reitzenstein, A. Hartschuh, E. Malic, L. M. Malard
Nanoscale 15, 7154 (2023)
- XXVI. **Link between interlayer hybridization and ultrafast charge transfer in WS₂-graphene heterostructures**
N. Hofmann, L. Weigl, J. Gradl, N. Mishra, G. Orlandini, S. Forti, C. Coletti, S. Latini, L. Xian, A. Rubio, D. Perez-Paredes, **R. Perea-Causin**, S. Brem, E. Malic, and I. Gierz
2D Materials (2023)
- XXVII. **Exciton transport in atomically thin semiconductors**
E. Malic, **R. Perea-Causin**, D. Erkensten, R. Rosati, and S. Brem
Nature Communications (2023)

XXVIII. Fermi-pressure and Coulomb repulsion driven rapid hot plasma expansion in a van der Waals heterostructure

J. Choi, J. Embley, D. D. Blach, **R. Perea-Causin**, D. Erkensten, D. S. Kim, L. Yuan, W. Y. Yoon, T. Taniguchi, K. Watanabe, K. Ueno, E. Tutuc, S. Brem, E. Malic, X. Li, and L. Huang
Nano Letters 23 (10), 4399 (2023)

XXIX. Electrically tunable dipolar interactions between layer-hybridized excitons

D. Erkensten, S. Brem, **R. Perea-Causin**, J. Hagel, F. Tagarelli, E. Lopriore, A. Kis, E. Malic
arXiv:2305.01845 (2023)

XXX. Ultrafast direct imaging of the complete excitonic landscape in WS₂

L. Münster, **R. Perea-Causin**, S. Zajusch, S. Brem, J. GÜdde, K. Tanimura, Y. Gerasimenko, R. Huber, E. Malic, R. Wallauer, and U. Höfer
In preparation (2023)

My contribution to the non-appended publications

In papers X, XV, XXV, XXVIII, and XXX I developed the theoretical model, performed the numerical evaluations, and analyzed the results as one of the leading theory authors. In the other publications, I took part in developing the theoretical models and analyzing the results during the supervision or in collaboration with the leading theory authors.

Contents

1	Introduction	1
2	Theoretical framework	7
2.1	Second quantization formalism	7
2.2	Many-particle Hamiltonian	8
2.3	Equation of motion	15
2.4	Effective few-body Hamiltonian	18
3	Optical response — Excitons and Mott transition	21
3.1	Excitonic optical spectra	21
3.2	Density-dependent spectra and the Mott transition	26
4	Exciton dynamics — Thermalization, dissociation, and propagation	33
4.1	Exciton-phonon scattering	34
4.2	Exciton thermalization	36
4.3	Phonon-assisted exciton dissociation	39
4.4	Exciton propagation	43

5	Trion dynamics — Trion–phonon scattering, transport, and photoluminescence	51
5.1	Trion–phonon scattering and transport	52
5.2	Trion photoluminescence	57
6	Conclusion and outlook	67
	Bibliography	71

CHAPTER 1

Introduction

The isolation and characterization of graphene—a single layer of graphite—in 2004 [1] marked the beginning of one of the most exciting journeys in modern physics. This work, which was recognised with the Nobel prize in 2010, constituted the first experimental realization of a stable atomically-thin material and opened the way for the study of a large variety of two-dimensional materials that exhibit a plethora of exotic properties [2–8]. Among them, semiconducting transition-metal dichalcogenides (TMDs) stand out as very promising candidates for applications in optoelectronic devices owing to their strong optical absorption/emission and large tunability [5, 9–13]. These materials have the composition MX_2 and consist of a layer of transition metal atoms ($\text{M}=\text{Mo}, \text{W}$) sandwiched between two layers of chalcogen atoms ($\text{X}=\text{S}, \text{Se}$), overall forming a honeycomb lattice (c.f. Fig. 1.1).

A particular feature of TMDs, and atomically-thin semiconductors in general, is the prominent role of excitons [11–16]. When a photon with sufficiently large energy hits the semiconductor, an electron from the valence band is

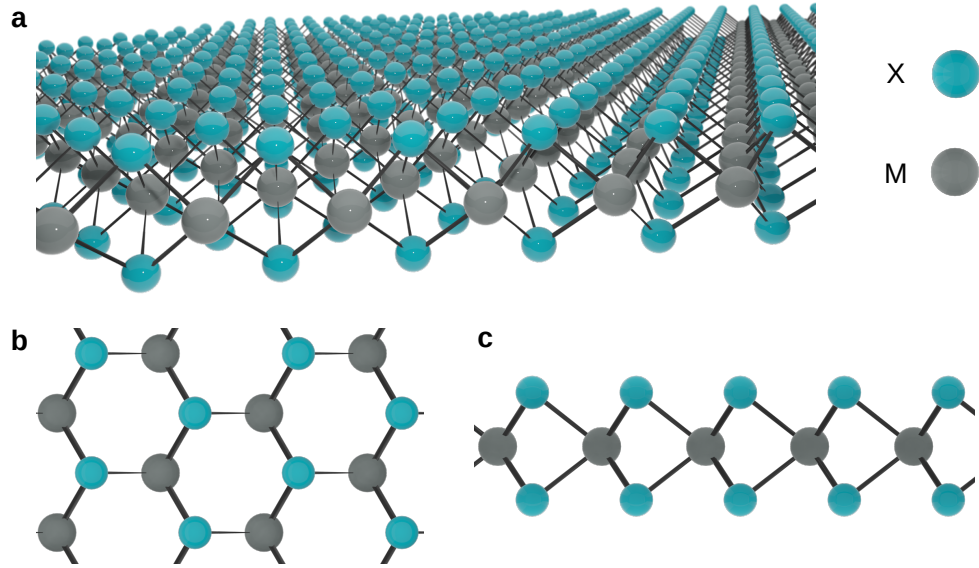


Figure 1.1: **a**: Three-dimensional representation of the atomic structure of a TMD monolayer (MX_2 , with $\text{M}=\text{Mo}, \text{W}$ and $\text{X}=\text{S}, \text{Se}$). **b**: Top and **c**: side perspectives.

promoted to the conduction band, leaving behind a positively-charged hole. The photoexcited electron-hole pair becomes tightly bound by the attractive Coulomb interaction, forming a quasi-particle—the exciton—which has an energy lower than that of a free electron-hole pair. In bulk semiconductors, excitons play a minor role due to the strong screening of the Coulomb interaction by the charges present in the material. In contrast, the interaction strength in atomically-thin materials can be greatly enhanced by the lower dielectric screening of the surroundings, as illustrated in Fig. 1.2a. As a consequence, excitons acquire binding energies of hundreds of meV [14, 15] and are therefore thermally stable even at room temperature. Tightly bound excitons are responsible for the exceptionally large optical absorption and emission of TMD monolayers [3, 17] (cf. exciton peak in Fig. 1.2b), making these materials particularly interesting for applications in atomically-thin photodetectors, solar cells, and light-emitting devices [11, 12, 18].

An effective utilization of TMDs relies on the accurate control of any conditions that may modify the optical and transport properties of the material. In particular, the density of photoexcited electron-hole pairs and doping determines the relevance of different interaction mechanisms and the presence

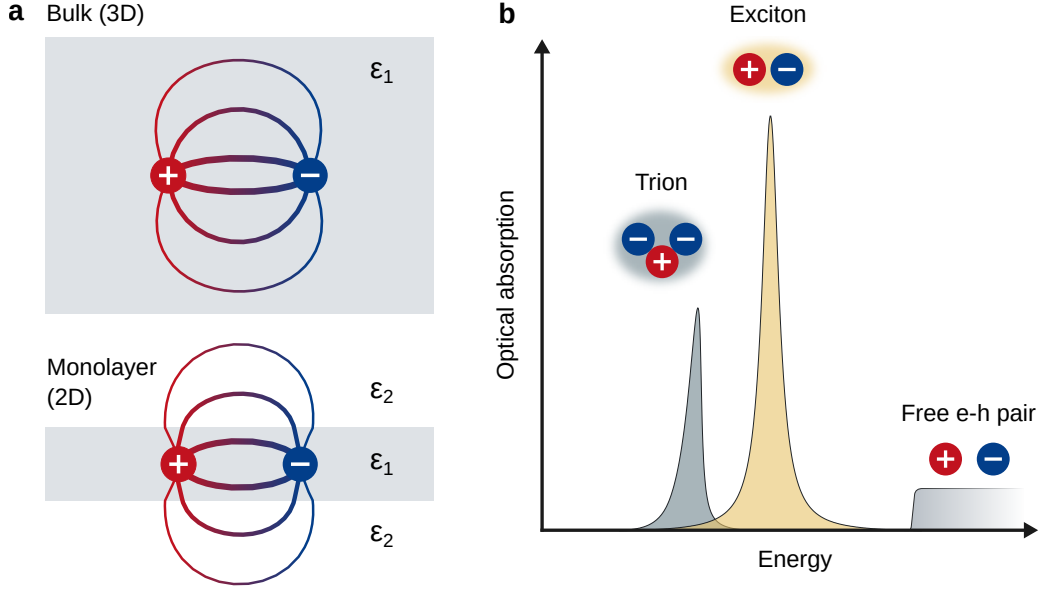


Figure 1.2: **a**: Dielectric screening of the Coulomb interaction in bulk and monolayers [14]. In the monolayer case, the electric field lines extend to the surrounding materials with low dielectric constant ($\epsilon_2 < \epsilon_1$), resulting in weaker dielectric screening. **b**: Schematic illustration of the optical absorption spectrum in TMDs with exciton and trion resonances, as well as the above-bandgap continuum of free electron-hole pairs.

of charge complexes beyond excitons. For example, a large photoexcitation density leads to the emergence of exciton–exciton interactions [19–22], the formation of biexcitons (bound two-exciton compounds) [23–25], and eventually to the Mott transition into an electron-hole plasma [26]. On the other hand, doping the material with additional electrons or holes enables the formation of trions—three-particle compounds formed by a photoexcited electron-hole pair bound to a doping charge. These different effects have distinct signatures in absorption and photoluminescence spectra, such as spectral broadening and shifts of excitonic resonances, and the emergence of new resonances originating from the creation or recombination of higher-order charge complexes (see trion peak in Fig. 1.2b) [27, 28]. Furthermore, the density of electrons and holes can significantly impact the transport properties of the material. For example, electric transport in undoped TMDs is very inefficient as excitons have a neutral charge. Transport of excitons therefore relies on alterna-

tive approaches such as strain or dielectric engineering [29–31]. In contrast, trions possess a finite charge and can hence be easily directed by an external electric field [32, 33], making them suitable for electric transport. A thorough understanding of the influence of different charge complexes on the material properties is crucial for the technological application of atomically-thin semiconductors.

In this thesis, we provide microscopic insights on the impact of charge complexes such as excitons and trions on the optics, thermalization dynamics, and transport in TMDs. The theoretical framework used here is based on the density-matrix formalism and the Heisenberg equation of motion combined with the cluster expansion method, allowing us to describe the dynamics of relevant quantities (e.g. exciton occupation, phonon and photon number). Importantly, we make use of the Fock space truncation scheme to set up effective Hamiltonians describing excitons and trions. The microscopic theory introduced in Chapter 2 enables the study of charge complexes in TMDs. First, we investigate how excitation density affects the excitonic features of optical absorption (Chapter 3). After that, we model the exciton formation, dissociation, and propagation dynamics that occur after photoexcitation (Chapter 4). Finally, we extend our model to doped samples and study trion dynamics, focusing on transport and recombination processes (Chapter 5). The main results of this thesis are listed and summarized below:

Paper I. Together with experimental support, we trace the emergence of photoluminescence halos back to the formation of a substantial temperature gradient in the exciton gas after intense photoexcitation.

The concepts and methods used to describe spatiotemporal dynamics in this work have been extended to describe various other phenomena such as electron diffusion in graphene, exciton diffusion including non-equilibrium effects and strain engineering (Papers IX, X, XIII, XVI, XVII, XVIII), anomalous diffusion of interlayer excitons (Papers XXI, XXIV, and XXIV), and the ultra-fast propagation of a degenerate hole gas (Paper XXVIII).

Paper II. We predict the optical signatures in pump-probe spectroscopy caused by large photoexcitation densities, tracking the evolution of the system from an exciton gas to an electron-hole plasma

through the Mott transition.

The insights gained in this work also led to a better understanding of the Mott transition (Papers XX and XXV) and band renormalization (Paper XXIII) resolved in experiments.

Paper III. In this joint theory–experiment study, we resolve the exciton thermalization dynamics immediately after an optical excitation and track the ultra-fast formation of optically inactive (dark) excitons. Our theoretical support provides insights into the role of exciton–phonon scattering and the impact of off-resonant excitation.

A continuation of this work reveals the underlying mechanisms in the spin relaxation dynamics (Paper XXX). We have also resolved exciton thermalization and the role of dark excitons in photoluminescence spectra (Paper XI).

Paper IV. We disentangle the underlying mechanisms in phonon-assisted exciton dissociation and predict the fundamental limitations of the photoresponse in TMD-based devices.

Paper V. We investigate the trion-phonon interaction as well as its impact on trion transport, and predict the enhancement of trion diffusion due to the build-up of Fermi pressure in the degenerate trion gas.

Paper VI. We model the trion photoluminescence originating from direct and phonon-assisted recombination, shedding light on the optical signatures of bright and dark trions, and predicting the important role of trions with an electron at the Λ point of the Brillouin zone.

CHAPTER 2

Theoretical framework

In this Chapter, we introduce the theoretical framework that allows us to study a many-particle quantum system. First, we present the second quantization formalism and introduce the Hamiltonian of the system. After that, we describe how to obtain solvable equations of motion for relevant microscopic quantities such as microscopic polarization and particle occupation. At the end, we outline how one can derive an effective few-particle Hamiltonian to describe the dynamics of charge complexes by truncating the Fock space to the relevant subspaces.

2.1 Second quantization formalism

An intuitive and convenient treatment of a many-particle quantum system can be obtained by means of the second quantization formalism [34–38], where states are represented in the occupation number basis. In this formalism, any many-particle state can be described as a set of creation (a_i^\dagger)

and annihilation (a_i) operators acting on the ground state of the system, with each of these operators acting on the single-particle state $|i\rangle$. The fermionic or bosonic character of the particle described by these operators is encoded in the commutation relations

$$\left[a_i, a_j \right]_{\pm} = \left[a_i^{\dagger}, a_j^{\dagger} \right]_{\pm} = 0, \quad (2.1)$$

$$\left[a_i, a_j^{\dagger} \right]_{\pm} = \delta_{ij}, \quad (2.2)$$

where $- (+)$ indicates (anti-)commutation of bosons (fermions). In this framework, any single-particle and two-particle operators can be respectively expressed as

$$\hat{O}^{(1)} = \sum_{ij} \langle i | \hat{o}^{(1)} | j \rangle a_i^{\dagger} a_j, \quad (2.3)$$

$$\hat{O}^{(2)} = \frac{1}{2} \sum_{ijklm} \langle i, j | \hat{o}^{(2)} | l, m \rangle a_i^{\dagger} a_j^{\dagger} a_l a_m, \quad (2.4)$$

where $\hat{o}^{(1)}$ and $\hat{o}^{(2)}$ are the “first-quantized” operators. This approach will prove particularly useful for setting up the Hamiltonian of the system and defining microscopic quantities in a very intuitive way. For further details on the second quantization formalism we refer the reader to Refs. [34–38].

2.2 Many-particle Hamiltonian

The Hamiltonian is of crucial importance for describing the eigenstates and time evolution of a system. Throughout this work, we consider the scenario of electrons in a solid that is photoexcited by a laser, i.e. a many-particle problem of interacting electrons, phonons, and photons. Here, we introduce the different parts of the Hamiltonian,

$$H = H_{e,0} + H_{\text{phon},0} + H_{\text{phot},0} + H_{e-e} + H_{e-\text{phon}} + H_{e-\text{light}} + H_{e-\text{phot}}, \quad (2.5)$$

describing quasi-free electrons in a crystal lattice ($H_{e,0}$), phonons ($H_{\text{phon},0}$), photons ($H_{\text{phot},0}$), and the electron-electron (H_{e-e}), electron-phonon ($H_{e-\text{phon}}$), semiclassical electron-light ($H_{e-\text{light}}$), and quantum-mechanical electron-photon ($H_{e-\text{phot}}$) interactions.

Quasi-free electrons in a lattice

The common approach to treating electrons in a crystal is to consider the influence of the potential generated by a static lattice of ions and reduce the many-electron system into a single-electron problem [39]. Electrons in this system are characterized by a set of single-particle energies $E_{\lambda\mathbf{k}}$ that form the band structure of the material, where λ is the band index (containing also the electron spin) and \mathbf{k} is the wave number or momentum, which is here restricted to the 2D plane of the monolayer material. The Hamiltonian describing this simple scenario is

$$H_{e,0} = \sum_{\lambda\mathbf{k}} E_{\lambda\mathbf{k}} a_{\lambda\mathbf{k}}^\dagger a_{\lambda\mathbf{k}}, \quad (2.6)$$

where $a_{\lambda\mathbf{k}}^{(\dagger)}$ is the fermionic annihilation (creation) operator for an electron in the state $|\lambda, \mathbf{k}\rangle$.

The typical band structure of semiconducting TMDs is usually computed via density functional theory, resulting in the conduction and valence bands sketched in Fig. 2.1a. In general, we are interested in the regions near minima and maxima of the conduction and valence bands, respectively, where photoexcitation and thermalization processes take place. Minima and maxima of the bands occur at the symmetry points of the Brillouin zone denoted by Γ , $\Lambda^{(\cdot)}$ and $K^{(\cdot)}$. The band structure around these points can be well approximated with a parabolic dispersion, $E_{\lambda\mathbf{k}} = E_{\lambda 0} + \hbar^2 \mathbf{k}^2 / (2m)$, meaning that the electron behaves as a free particle with an effective mass m that reflects the curvature of the band. The parabolic band around a symmetry point is commonly denoted as valley. Throughout this work, we consider the band structure of TMDs via the effective mass approach as illustrated in Fig 2.1b, where the spin ordering in K and K' (as well as Λ and Λ') is flipped due to time reversal symmetry. This approach allows us to take into account the multi-valley band structure, including spin-splitting of the bands, in a simple way. We extract the effective masses and relative energies from density functional theory calculations in Ref. [40]. Furthermore, we approximate the dispersion around the $\Lambda^{(\cdot)}$ as isotropic by averaging the effective mass over the x and y directions.

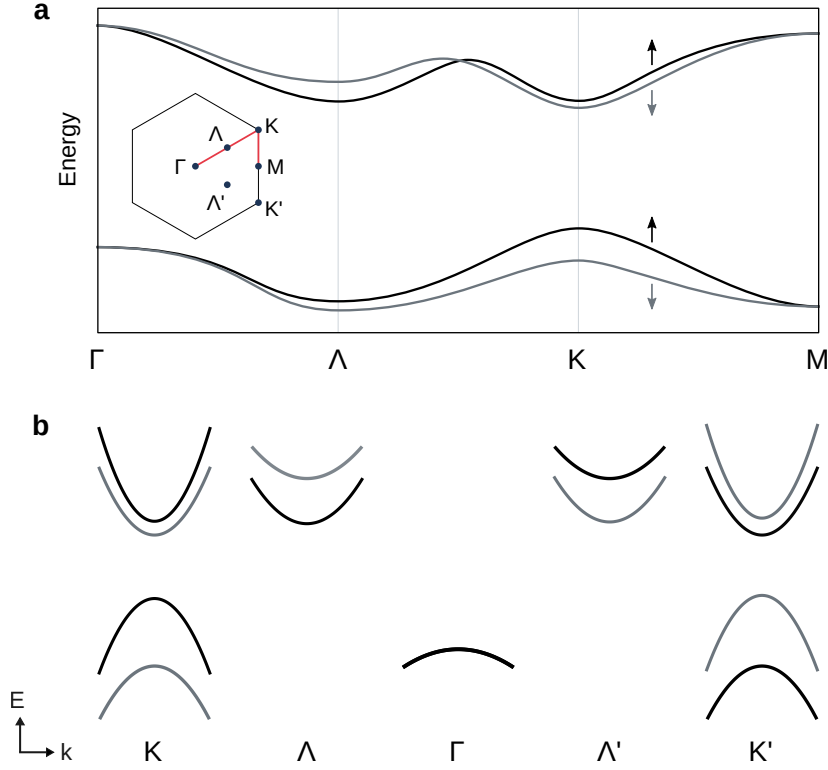


Figure 2.1: **a**: Sketch of the conduction and valence bands of semiconducting TMD monolayers [40] along the path denoted by the red line in the Brillouin zone. **b**: Illustration of the multi-valley effective mass approach to the band structure.

Phonons

Phonons are energy quanta of harmonic lattice vibrations. Throughout this work, we will see that phonons play an essential role in the relaxation dynamics, assisting quasiparticles in reaching a thermal distribution, and can even assist the recombination of otherwise dark charge complexes. Non-interacting phonons are described by the free-particle Hamiltonian [38]

$$H_{\text{phon},0} = \sum_{j\mathbf{q}} \hbar\Omega_{j\mathbf{q}} \left(b_{j\mathbf{q}}^\dagger b_{j\mathbf{q}} + \frac{1}{2} \right), \quad (2.7)$$

where we have introduced the phonon energy $\hbar\Omega_{j\mathbf{q}}$ and the bosonic annihilation (creation) operator $b_{j\mathbf{q}}^{(\dagger)}$ acting on a phonon of mode j with momen-

tum \mathbf{q} . The phonon energy $\hbar\Omega_{j\mathbf{q}}$ is usually obtained by diagonalizing the so-called dynamical matrix, which contains the interatomic force constants resulting from the Coulomb interaction between ions [41, 42]. While in general the phonon dispersion can look rather complex, we limit ourselves to momenta around the Γ , $K^{(i)}$, $\Lambda^{(i)}$, and M high-symmetry points. Phonons in these regions will assist the main intra- and intervalley electronic transitions. Moreover, the dispersion around these points can be conveniently described as linear in the case of long wavelength (Γ -point) acoustic phonons with velocity v , that is $\Omega_{j\mathbf{q}} \approx v|\mathbf{q}|$, or constant otherwise, $\Omega_{j\mathbf{q}} \approx \Omega_{j0}$, in analogy to the Debye and Einstein models. The energies and sound velocities needed to parametrize the dispersion in this manner are extracted from *ab initio* calculations in Ref. [43]. While there are 9 phonon modes present in a TMD, Ref. [43] shows that the only modes relevant for electron-phonon scattering are the longitudinal and transversal acoustic and optical modes (LA, TA, LO, TO), and the out-of-plane A_1 mode.

Photons

Photons are energy quanta of the electromagnetic field. Exploiting the fact that the electromagnetic field can be described as a set of independent harmonic oscillators, the photon Hamiltonian can be written as [38, 44]

$$H_{\text{phot},0} = \sum_{\sigma\boldsymbol{\kappa}} \hbar\omega_{\sigma\boldsymbol{\kappa}} \left(c_{\sigma\boldsymbol{\kappa}}^\dagger c_{\sigma\boldsymbol{\kappa}} + \frac{1}{2} \right), \quad (2.8)$$

where we have introduced the annihilation (creation) operator $c_{\sigma\boldsymbol{\kappa}}^{(\dagger)}$ for a photon with mode or polarization σ and momentum $\boldsymbol{\kappa}$. The photon energy is given by the light-cone dispersion $\omega_{\sigma\boldsymbol{\kappa}} = c|\boldsymbol{\kappa}|$, with c being the speed of light in the medium surrounding the TMD layer.

Electron-electron interaction

The electron-electron interaction is responsible for the formation of bound charge complexes, and can also lead to significant energy renormalization and scattering rates. The two-particle Hamiltonian describing this interaction

reads

$$H_{\text{e-e}} = \frac{1}{2} \sum_{ijlm} V_{lm}^{ij} a_i^\dagger a_j^\dagger a_l a_m. \quad (2.9)$$

Here we introduced the Coulomb matrix element $V_{lm}^{ij} = \langle i, j | V(\mathbf{r} - \mathbf{r}') | l, m \rangle$, with $V(\mathbf{r})$ being the Coulomb potential and i, j, l, m being compound indices containing both band index λ and momentum \mathbf{k} . In the following we outline how this expression can be simplified to model a realistic system. By exploiting the Fourier transform of the Coulomb potential, $V(\mathbf{r}) = \sum_{\mathbf{q}} e^{i\mathbf{q}\cdot\mathbf{r}} V_{\mathbf{q}}$, the Coulomb matrix element can be written as

$$V_{lm}^{ij} = \sum_{\mathbf{q}} V_{\mathbf{q}} \langle i | e^{i\mathbf{q}\cdot\mathbf{r}} | m \rangle \langle j | e^{-i\mathbf{q}\cdot\mathbf{r}} | l \rangle.$$

One can further show that $\langle i | e^{i\mathbf{q}\cdot\mathbf{r}} | m \rangle = \sum_{\mathbf{G}} \delta_{\mathbf{k}_m + \mathbf{q} - \mathbf{k}_i, \mathbf{G}} \int_{\text{u.c.}} d^2\mathbf{r} u_i^*(\mathbf{r}) u_m(\mathbf{r})$, where \mathbf{G} is the reciprocal lattice vector and the integral over Bloch factors $u_i(\mathbf{r})$ is carried out in the unit cell. Since \mathbf{k} is restricted to the first Brillouin zone and $V_{\mathbf{q}}$ decays quickly with \mathbf{q} , only the term $\mathbf{G} = 0$ is relevant. Moreover, considering only intra-band processes¹ ($\lambda_i = \lambda_m, \lambda_j = \lambda_l$) with small momentum transfer \mathbf{q} , the Hamiltonian can be written as

$$H_{\text{e-e}} = \frac{1}{2} \sum_{\lambda\lambda'\mathbf{k}\mathbf{k}'\mathbf{q}} V_{\mathbf{q}} a_{\lambda,\mathbf{k}+\mathbf{q}}^\dagger a_{\lambda',\mathbf{k}'-\mathbf{q}}^\dagger a_{\lambda',\mathbf{k}'} a_{\lambda,\mathbf{k}}. \quad (2.10)$$

The Coulomb matrix element in this case is simply the Fourier transform of the Coulomb potential without any additional form factors. Moreover, this Hamiltonian describes momentum (and spin) conserving transitions, $\mathbf{k} \rightarrow \mathbf{k} + \mathbf{q}$ and $\mathbf{k}' \rightarrow \mathbf{k}' - \mathbf{q}$. For an accurate description of the Coulomb interaction in a TMD monolayer, we consider the finite thickness of the material together with the dielectric properties of the surroundings and solve the corresponding Poisson equation to obtain the potential generated by a charge in the TMD, obtaining

$$V_{\mathbf{q}} = \frac{e_0^2}{2|\mathbf{q}|\epsilon(\mathbf{q})}. \quad (2.11)$$

This potential has the form of a 2D Coulomb potential with non-local (i.e. \mathbf{q} -dependent) dielectric screening [47] and is sometimes called after Rytova [48] and Keldysh [49] in literature. The exact form of $\epsilon(\mathbf{q})$ can be found in Refs. [48–50].

¹Note that inter-band processes are necessary for describing Auger scattering and electron-hole exchange (see Paper XIX and Refs. [45, 46]).

Electron–phonon interaction

The interaction between electrons and phonons appears in the theoretical model when we consider the interaction of electrons with the lattice beyond the static approximation. In particular, one takes into account the ion vibrations via the first-order Taylor expansion of the electron–ion interaction potential around the equilibrium ion positions [38]. The Hamiltonian for the electron–phonon interaction,

$$H_{\text{e-phon}} = \sum_{ijl} \left(g_l^{ij} a_i^\dagger a_j b_l + g_l^{ij*} a_j^\dagger a_i b_l^\dagger \right), \quad (2.12)$$

intuitively illustrates the possible electronic transitions assisted by the emission (b_l^\dagger) or absorption (b_l) of a phonon. The electron–phonon coupling element reads

$$g_l^{ij} = \sqrt{\frac{\hbar}{2\rho A \Omega_l}} \langle i | \Delta V_l | j \rangle, \quad (2.13)$$

where A is the area of the system, ρ is the mass density of the material, and ΔV_l is the scattering potential which contains the electron–ion interaction and the polarization vector of the phonon mode. Within the deformation potential approach [43, 51], we approximate the scattering potential to first order in momentum for long-wavelength acoustic phonons and to zeroth order for the remaining modes. Throughout this work, we use deformation potential parameters from *ab initio* calculations in Ref. [43] based on density functional perturbation theory.

Electron–photon interaction

The last important interaction that we introduce here is that between electrons and photons. This interaction can be conveniently described in either a semiclassical or a quantum mechanical approach, depending on the nature of the studied phenomenon.

Semiclassical approach

In order to describe the optical absorption of the material, it is sufficient to treat light as a classical electromagnetic field. Within this approach, the electron–light interaction can be expressed in the so-called minimal-coupling Hamiltonian [44],

$$H_{\text{e-light}} = \frac{e_0}{m_0} \sum_{ij} \mathbf{M}_{ij} \cdot \mathbf{A}(t) a_i^\dagger a_j, \quad (2.14)$$

where we have introduced the optical matrix element $\mathbf{M}_{ij} = \langle i | \mathbf{p} | j \rangle$ with the momentum operator \mathbf{p} , the electromagnetic vector potential $\mathbf{A}(t)$, the elementary charge e_0 , the free electron mass m_0 , and the reduced Planck constant \hbar . In order to arrive to this expression, we have considered the Coulomb gauge and assumed sufficiently weak excitations so that \mathbf{A}^2 terms are negligible. Moreover, we have applied the dipole approximation, in which the vector potential is assumed to vary weakly on the length scale of variations of the electronic wave functions.

In general, this Hamiltonian describes intra- or inter-band electronic transitions caused by the absorption of light. Here, we will overall focus on inter-band transitions, i.e. electrons being promoted from the valence band to the conduction band. The optical matrix element for inter-band transitions can be approximately written in terms of band structure parameters [52, 53] such as the band gap E_g and the electron-hole reduced mass $\mu^{-1} = m_e^{-1} + m_h^{-1}$, reading $|\mathbf{M}_{ij}| = m_0 \sqrt{E_g/2\mu}$. Importantly, TMD monolayers exhibit circular dichroism [54], where K and K' valleys couple to light with opposite circular polarization. This property, combined with the large spin-splitting of the valence bands, implies that electrons in a specific valley and with a specific spin can be selectively photoexcited by choosing the excitation energy and chirality of the circular polarization [55]. Although this is a very interesting aspect of TMDs, throughout this work we usually consider linearly polarized light, so that electrons in K and K' valleys are equally excited.

Quantum mechanical approach

Photoluminescence (PL), i.e. photon emission due to radiative recombination of electron-hole pairs, is experimentally used as a tool to access the thermal-

ization and recombination dynamics of electron-hole pairs [13]. Particularly interesting is the time evolution after the initial photoexcitation, when external fields are absent and the interband coherence or polarization has already decayed. In this regime, electron-hole pairs recombine by spontaneous emission of photons—a process that cannot be described classically. Therefore, PL must be described on a fully quantum mechanical approach, where the electromagnetic field is quantized and described in terms of photon creation and annihilation operators. The Hamiltonian describing the electron–photon interaction reads [44, 56]

$$H_{\text{e-photon}} = \sum_{ijl} \left(\mathcal{M}_l^{ij} a_i^\dagger a_j c_l + \mathcal{M}_l^{ij*} a_j^\dagger a_i c_l^\dagger \right), \quad (2.15)$$

with the electron–photon matrix element $\mathcal{M}_l^{ij} = \frac{e_0}{m_0} \sqrt{\frac{\hbar}{2\epsilon V \omega_l}} \mathbf{e}_l \cdot \mathbf{M}_{ij}$ containing the permittivity of the medium ϵ , the volume of the system V , and the Jones vector \mathbf{e}_l . In both semiclassical and quantum-mechanical approaches, we usually consider only terms that fulfill energy conservation, i.e. electron-hole annihilation with photon creation and electron-hole creation with photon annihilation, since other terms become negligible under a rotating wave approximation [44].

2.3 Equation of motion

The Hamilton operator provides access to the temporal dynamics of the system. In particular, one can exploit Heisenberg’s equation of motion to find the time evolution of an observable O , that is $i\hbar \frac{dO}{dt} = [O, H]$, where we have assumed that O does not depend explicitly on time. Typically, we are interested in the expectation value $\langle O \rangle$, which can be evaluated as $\langle O \rangle = \text{Tr}(\hat{\rho} O)$ with the density operator $\hat{\rho}$. The equation of motion for $\langle O \rangle$ is then simply

$$i\hbar \frac{d\langle O \rangle}{dt} = \langle [O, H] \rangle. \quad (2.16)$$

In practice, we will be interested in the temporal evolution of observables such as electron occupation $\rho_{\lambda, \mathbf{k}} = \langle a_{\lambda, \mathbf{k}}^\dagger a_{\lambda, \mathbf{k}} \rangle$, microscopic polarization $p_{\mathbf{k}} = \langle a_{c, \mathbf{k}}^\dagger a_{v, \mathbf{k}} \rangle$, and phonon number $n_{j, \mathbf{q}} = \langle b_{j, \mathbf{q}}^\dagger b_{j, \mathbf{q}} \rangle$. A detailed description of

the calculation of equations of motion within the density matrix formalism can be found in Ref. [57].

Cluster expansion

A usual difficulty that appears when treating many-particle systems is the so-called hierarchy problem. If we want to find the temporal evolution of a one-particle quantity, e.g. the electron occupation $\rho_{\lambda,\mathbf{k}}$, we will see that $\rho_{\lambda,\mathbf{k}}$ couples to two-particle expectation values of the form $\langle a_1^\dagger a_2^\dagger a_3 a_4 \rangle$. In order to solve the equation of motion for $\rho_{\lambda,\mathbf{k}}$, we thus need to find the corresponding equation for $\langle a_1^\dagger a_2^\dagger a_3 a_4 \rangle$, which couples to three-particle quantities, and so on. This gives rise to an infinite number of coupled equations, rendering the problem unsolvable. The solution to this problem is the cluster-expansion and truncation method [58], which we summarize below.

First, we express N -particle quantities in terms of independent single-particle quantities (singlets) and higher-order corrections that account for n -particle correlations, where $n = 2, 3, 4, \dots, N$. After this, we truncate the system to account for a relevant number of correlated particles that allows us to solve the equation of motion. A typical example of the cluster expansion and truncation is the Hartree-Fock approximation, where the two-electron expectation value $\langle a_1^\dagger a_2^\dagger a_3 a_4 \rangle$ is expanded in terms of singlets,

$$\langle a_1^\dagger a_2^\dagger a_3 a_4 \rangle = \langle a_2^\dagger a_3 \rangle \langle a_1^\dagger a_4 \rangle - \langle a_1^\dagger a_3 \rangle \langle a_2^\dagger a_4 \rangle + \langle a_1^\dagger a_2^\dagger a_3 a_4 \rangle^c, \quad (2.17)$$

and the two-particle correlation $\langle a_1^\dagger a_2^\dagger a_3 a_4 \rangle^c$ is neglected. This particular example simplifies the system into a single-electron problem, where the interaction with other electrons is approximated as a mean field. For this reason, this specific example is also called *mean-field approximation*.

Markov approximation

A way of including higher-order correlations in a solvable way is to use the Markov approximation [34, 37]. Let us take the problem of electron-phonon scattering as an example. When considering the electron-phonon interaction

in the equation of motion for the electron occupation $\rho_{\lambda,\mathbf{k}}$, we will see that $\rho_{\lambda,\mathbf{k}}$ couples to a two-particle correlation of the type $S = \langle a_1^\dagger a_2 b_3 \rangle^c$, describing an electronic transition from state 2 to 1 assisted by the absorption of a phonon. The equation of motion for S will have the form

$$\dot{S}(t) = (i\omega - \gamma)S(t) + Q(t), \quad (2.18)$$

where $Q(t)$ is the source of electron-phonon correlation². The analytical solution of this equation is

$$S(t) = \int_0^\infty d\tau e^{(i\omega - \gamma)\tau} Q(t - \tau). \quad (2.19)$$

The Markov approximation consists in neglecting the past values of Q , i.e. assuming $Q(t - \tau) \approx Q(t)e^{-i\omega_Q\tau}$. Although we neglect the memory of Q , note that we take into account its temporal oscillation with frequency ω_Q , which is essential for properly capturing the energy conservation of the scattering process³. Then, this complicated integral can be easily solved and we obtain

$$S(t) = -i \frac{Q(t)}{(\omega - \omega_Q) - i\gamma}. \quad (2.20)$$

In the limit where the decay rate γ goes to zero, the Sokhotski–Plemelj theorem can be applied to obtain

$$S(t) = \pi Q(t) \delta(\omega - \omega_Q) - i\mathcal{P} \left(\frac{Q(t)}{\omega - \omega_Q} \right). \quad (2.21)$$

Here \mathcal{P} denotes the Cauchy principal value. When $S(t)$ is plugged back in the equation of motion for the corresponding single-particle quantity (e.g. electron occupation or phonon number), the first term will give rise to a scattering rate with exact energy conservation, while the second one will result in the renormalization of the single-particle energy. In general, we will neglect the energy renormalization term, assuming that it is already accounted for in the single-particle energies.

²See Eq. (4.5) as an example for the case of exciton-phonon scattering.

³For example, if Q is a coherent quantity such as interband polarization, $Q \sim \langle a_{\mathbf{c}\mathbf{k}}^\dagger a_{\mathbf{v}\mathbf{k}} \rangle$, then $\hbar\omega_Q = E_{\mathbf{c}\mathbf{k}} - E_{\mathbf{v}\mathbf{k}}$. On the other hand, for incoherent quantities such as electron occupation, we have $Q \sim \langle a_{\mathbf{c}\mathbf{k}}^\dagger a_{\mathbf{c}\mathbf{k}} \rangle$ and $\hbar\omega_Q = 0$.

2.4 Effective few-body Hamiltonian

The physics of charge complexes such as excitons and trions can be described by directly exploiting Heisenberg's equation of motion together with the electron Hamiltonian (2.5) [58–61]. However, the equations of motion quickly become tedious as exciton and trion occupations are described by expectation values of four and six operators, respectively. A more effective approach consists in deriving an effective Hamiltonian limited to the relevant charge complexes. For example, in the undoped regime at low photoexcitation densities, all electron-hole pairs can be considered to be bound into excitons. Therefore, an effective Hamiltonian describing excitons should be appropriate to investigate this system. In this Section, we outline how such a Hamiltonian can be formally derived.

We start with the Hamiltonian for a system of interacting electrons and holes,

$$H_x = \sum_{\mathbf{k}} \left(E_{\mathbf{k}}^e e_{\mathbf{k}}^\dagger e_{\mathbf{k}} + E_{\mathbf{k}}^h h_{\mathbf{k}}^\dagger h_{\mathbf{k}} \right) - \sum_{\mathbf{k}\mathbf{k}'\mathbf{q}} V_{\mathbf{q}} e_{\mathbf{k}+\mathbf{q}}^\dagger h_{\mathbf{k}'-\mathbf{q}}^\dagger h_{\mathbf{k}'} e_{\mathbf{k}}. \quad (2.22)$$

Here, we have defined the electron and hole operators, $e_{\mathbf{k}}^\dagger = a_{\mathbf{c}\mathbf{k}}^\dagger$ and $h_{\mathbf{k}}^\dagger = a_{\mathbf{v},-\mathbf{k}}^\dagger$, respectively, and disregarded the electron–electron and hole–hole interactions which are not relevant at low densities in the undoped regime. We can already identify exciton or pair operators $P_{\mathbf{k}\mathbf{k}'} = h_{\mathbf{k}'} e_{\mathbf{k}}$ in the interaction term. The next step is to write the first term also in terms of pair operators or states. To do so, we expand the electron and hole operators in Fock space [62–64],

$$\begin{aligned} e_{\mathbf{k}}^\dagger e_{\mathbf{k}} &= |e_{\mathbf{k}}\rangle \langle e_{\mathbf{k}}| + \frac{1}{2} \sum_{\mathbf{k}'} |e_{\mathbf{k}} e_{\mathbf{k}'}\rangle \langle e_{\mathbf{k}} e_{\mathbf{k}'}| + \sum_{\mathbf{k}'} |e_{\mathbf{k}} h_{\mathbf{k}'}\rangle \langle e_{\mathbf{k}} h_{\mathbf{k}'}| + \dots \\ &\approx \sum_{\mathbf{k}'} |e_{\mathbf{k}} h_{\mathbf{k}'}\rangle \langle e_{\mathbf{k}} h_{\mathbf{k}'}| \end{aligned} \quad (2.23)$$

$$\begin{aligned} h_{\mathbf{k}}^\dagger h_{\mathbf{k}} &= |h_{\mathbf{k}}\rangle \langle h_{\mathbf{k}}| + \frac{1}{2} \sum_{\mathbf{k}'} |h_{\mathbf{k}} h_{\mathbf{k}'}\rangle \langle h_{\mathbf{k}} h_{\mathbf{k}'}| + \sum_{\mathbf{k}'} |h_{\mathbf{k}} e_{\mathbf{k}'}\rangle \langle h_{\mathbf{k}} e_{\mathbf{k}'}| + \dots \\ &\approx \sum_{\mathbf{k}'} |e_{\mathbf{k}'} h_{\mathbf{k}}\rangle \langle e_{\mathbf{k}'} h_{\mathbf{k}}| \end{aligned} \quad (2.24)$$

where we have used the completeness of Fock space,

$$\begin{aligned} \mathbb{1} = & |0\rangle \langle 0| + \sum_{\mathbf{k}} (|e_{\mathbf{k}}\rangle \langle e_{\mathbf{k}}| + |h_{\mathbf{k}}\rangle \langle h_{\mathbf{k}}|) + \sum_{\mathbf{k}'} |e_{\mathbf{k}}h_{\mathbf{k}'}\rangle \langle e_{\mathbf{k}}h_{\mathbf{k}'}| \\ & + \frac{1}{2} \sum_{\mathbf{k}\mathbf{k}'} (|e_{\mathbf{k}}e_{\mathbf{k}'}\rangle \langle e_{\mathbf{k}}e_{\mathbf{k}'}| + |h_{\mathbf{k}}h_{\mathbf{k}'}\rangle \langle h_{\mathbf{k}}h_{\mathbf{k}'}|) + \dots \end{aligned} \quad (2.25)$$

and truncated the expansion to the subspace of single electron-hole pair states $|e_{\mathbf{k}}h_{\mathbf{k}'}\rangle$.⁴ Applying this scheme to both terms in the Hamiltonian yields

$$H_x = \sum_{\mathbf{k}_e \mathbf{k}_h} \left[(E_{\mathbf{k}_e}^e + E_{\mathbf{k}_h}^h) |P_{\mathbf{k}_e \mathbf{k}_h}\rangle - \sum_{\mathbf{q}} V_{\mathbf{q}} |P_{\mathbf{k}_e + \mathbf{q}, \mathbf{k}_h - \mathbf{q}}\rangle \right] \langle P_{\mathbf{k}_e \mathbf{k}_h}|, \quad (2.26)$$

with the electron-hole pair state $|P_{\mathbf{k}_e \mathbf{k}_h}\rangle = |e_{\mathbf{k}_e} h_{\mathbf{k}_h}\rangle$. We now transform this state into the basis of exciton states $|X_{\nu \mathbf{Q}}\rangle$, that is

$$|P_{\mathbf{k}_e \mathbf{k}_h}\rangle = \sum_v \Phi_{\mathbf{Q}\mathbf{k}}^\nu |X_{\nu \mathbf{Q}}\rangle, \quad (2.27)$$

where we have introduced the center-of-mass and relative momentum coordinates, $\mathbf{Q} = \mathbf{k}_e + \mathbf{k}_h$ and $\mathbf{k} = \alpha_h \mathbf{k}_e - \alpha_e \mathbf{k}_h$, with the mass ratio $\alpha_{e(h)} = m_{e(h)}/(m_e + m_h)$. The exciton wave functions $\Phi_{\mathbf{Q}\mathbf{k}}^\nu$ are solutions of the electron-hole Schrödinger equation,

$$(E_{\alpha_e \mathbf{Q} + \mathbf{k}}^e + E_{\alpha_h \mathbf{Q} - \mathbf{k}}^h) \Phi_{\mathbf{Q}\mathbf{k}}^\nu - \sum_{\mathbf{q}} V_{\mathbf{q}} \phi_{\mathbf{Q}, \mathbf{k} + \mathbf{q}}^\nu = E_{\nu \mathbf{Q}}^x \Phi_{\mathbf{Q}\mathbf{k}}^\nu, \quad (2.28)$$

with the exciton energy $E_{\nu \mathbf{Q}}^x$. The Hamiltonian in exciton basis then reads

$$H_x = \sum_{\nu \mathbf{Q}} E_{\nu \mathbf{Q}}^x |X_{\nu \mathbf{Q}}\rangle \langle X_{\nu \mathbf{Q}}|. \quad (2.29)$$

The many-body problem of interacting electrons and holes has thus been reduced to a single-particle problem of free excitons. Finally, the single-exciton

⁴This truncation is valid as long as the system is undoped, i.e. there is an equal number of electrons and holes, and the exciton density is sufficiently low. The criterion for what constitutes a low exciton density is dictated by the inequality $n_x a_B^2 \ll 1$, that is, the exciton density n_x must be small compared to the inverse square of the exciton Bohr radius a_B . In other words, the single-exciton description works well as long as the distance between neighbouring excitons is much larger than the “size” of the exciton.

projector can be mapped into a pair of exciton creation and annihilation operators [64], i.e. $|X_{\nu\mathbf{Q}}\rangle\langle X_{\nu\mathbf{Q}}| \rightarrow X_{\nu\mathbf{Q}}^\dagger X_{\nu\mathbf{Q}}$, noting that these should only act on single-exciton states according to the level of truncation applied. The exciton operators can be shown to satisfy purely bosonic commutation relations, i.e. $[X_i, X_j^\dagger] = \delta_{ij}$, with corrections that only become relevant at larger densities [62–64]. The mapping into bosonic operators facilitates the derivation of equations of motion via conventional commutation of creation and annihilation operators.

While here we have introduced the exemplary case of free single excitons, we will apply this method to describe the interactions between single excitons or trions with phonons and photons. This facilitates the study of thermalization, diffusion, and radiative recombination of these quasiparticles. This scheme has also been used to describe exciton–exciton interactions by considering the subspace of two-exciton states [64] and, in principle, can be extended to consider different coexisting charge complexes.

CHAPTER 3

Optical response — Excitons and Mott transition

The response of a material to an optical excitation is dictated by the quasi-particles that can be excited in the system. In this Chapter, we discuss the optical absorption spectra of atomically thin semiconductors across a wide range of photoexcitation densities. In particular, we first introduce the characteristic optical spectra of excitonic states in the low density regime. In the second part of this Chapter, we present Paper II, where we investigate the impact of charge-carrier densities up to the Mott transition on the optical response of the system.

3.1 Excitonic optical spectra

The optical absorption at low photoexcitation densities is dominated by excitonic states. In this Section, we outline the derivation of the well known Elliot formula, which describes the excitonic optical absorption spectra.

Optical susceptibility in linear response

The electric field \mathbf{E} of the incident laser pulse induces a polarization \mathbf{P} in the material. We consider a sufficiently weak excitation, so that the material's response is linear, i.e. $\mathbf{P}(\omega) = \epsilon_0 \chi(\omega) \mathbf{E}(\omega)$, where χ is the electric susceptibility tensor which we have assumed to be isotropic. Using the relation between the electric field and the vector potential in the Coulomb gauge, $\mathbf{E} = -\dot{\mathbf{A}}$, and between the polarization and the current density, $\mathbf{j} = \dot{\mathbf{P}}$, the susceptibility can be written as

$$\chi(\omega) = \frac{P(\omega)}{\epsilon_0 E(\omega)} = \frac{j(\omega)}{\epsilon_0 \omega^2 A(\omega)} \quad (3.1)$$

The imaginary part of the susceptibility describes the optical absorption of the material via the relation $\alpha(\omega) = (\omega/n c) \text{Im}[\chi(\omega)]$,¹ where n is the refractive index of the medium and c the speed of light in vacuum. The current density in second quantization reads

$$\mathbf{j}(t) = \frac{e_0}{2Am_0} \sum_{ij} \langle i|\mathbf{p}|j \rangle \langle a_i^\dagger a_j \rangle(t) = \frac{e_0}{Am_0} \sum_{\mathbf{k}} \text{Re}[\mathbf{M}_{\mathbf{k}} p_{\mathbf{k}}(t)], \quad (3.2)$$

where $\mathbf{M}_{\mathbf{k}} = \langle c, \mathbf{k} | \mathbf{p} | v, \mathbf{k} \rangle$ and $p_{\mathbf{k}}(t) = \langle e_{\mathbf{k}}^\dagger h_{\mathbf{k}} \rangle(t)$ are the optical matrix element and the time-dependent microscopic polarization, respectively. Here, we have omitted the intraband current that becomes important only at THz frequencies and considered interband terms containing conduction and valence bands. Thus, it becomes clear that interband absorption is governed by the microscopic polarization or interband coherence generated by the incident light.

Microscopic polarization

An optical excitation in a semiconductor generates a microscopic polarization $p_{\mathbf{k}}$ or coherence between the valence and conduction bands. The absolute squared value of this quantity can be regarded as the probability for a

¹This relation holds as long as non-radiative dephasing processes dominate over radiative ones [58]. This is usually the case, as dephasing at room temperature is dominated by scattering with phonons [65, 66].

valence-band electron to be promoted to the conduction band. The equation of motion for a general $p_{\mathbf{k}_e\mathbf{k}_h} = \langle e_{\mathbf{k}_e}^\dagger h_{\mathbf{k}_h}^\dagger \rangle$, including the electron–hole and electron–light interactions, reads

$$i\hbar\dot{p}_{\mathbf{k}_e\mathbf{k}_h}(t) = - (E_{\mathbf{k}_e}^e + E_{\mathbf{k}_h}^h) p_{\mathbf{k}_e\mathbf{k}_h}(t) + \sum_{\mathbf{q}} V_{\mathbf{q}} p_{\mathbf{k}_e+\mathbf{q},\mathbf{k}_h-\mathbf{q}}(t) - \hbar\Omega_{\mathbf{k}_e}(t)\delta_{\mathbf{k}_e\mathbf{k}_h}, \quad (3.3)$$

where we have applied the Hartree-Fock approximation and assumed a full valence band and an empty conduction band, i.e. we consider a weak field that generates a small density of electrons and holes. This equation is the low-density limit of the semiconductor Bloch equations [57]. The first term describes the oscillation of $p_{\mathbf{k}_e\mathbf{k}_h}$ with a frequency corresponding to the energy of a free electron–hole pair. The second term is a self-coupling of the polarization that results from the Coulomb attraction between conduction-band electrons and valence-band holes. Finally, the last term accounts for the optical generation of polarization via the Rabi frequency $\hbar\Omega_{\mathbf{k}}(t) = \frac{e_0}{m_0}\mathbf{M}_{\mathbf{k}}^* \cdot \mathbf{A}(t)$, only allowing momentum-conserving transitions due to the negligible momentum of the incident photons.

Exciton basis

The self-coupling of $p_{\mathbf{k}_e\mathbf{k}_h}$ with different momenta suggests that a basis transformation similar to that introduced in Section 2.4 would enable an analytical solution of Eq. (3.3). First, though, we consider the effective mass approximation, so that the energy of a free electron–hole pair can be decomposed in two terms describing the motion of the center-of-mass and relative coordinates \mathbf{Q} and \mathbf{k} , that is

$$E_{\mathbf{k}_e}^e + E_{\mathbf{k}_h}^h = E_g + \frac{\hbar^2\mathbf{Q}^2}{2M} + \frac{\hbar^2\mathbf{k}^2}{2\mu}. \quad (3.4)$$

Here, $M = m_e + m_h$ and $\mu = m_em_h/M$ are the total and reduced exciton masses, respectively. We can now expand the microscopic polarization into the exciton basis via

$$p_{\mathbf{k}_e\mathbf{k}_h}(t) = \sum_{\nu} \phi_{\mathbf{k}}^{\nu} P_{\nu\mathbf{Q}}(t). \quad (3.5)$$

In contrast to the basis transformation introduced in Section 2.4, here the exciton wave functions $\phi_{\mathbf{k}}^{\nu}$ are solutions of the Schrödinger equation describing

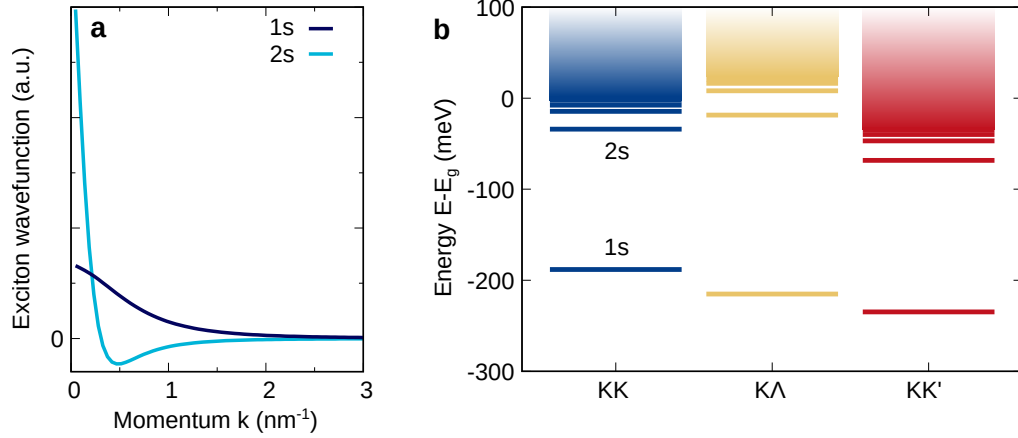


Figure 3.1: Excitons in WS_2 . **a**: Exciton wavefunction of 1s and 2s states in the KK valley. **b**: Exciton energy landscape including bright (KK) and momentum-dark ($\text{K}\Lambda$, KK') states.

the *relative* motion of an electron–hole pair,

$$\frac{\hbar^2 \mathbf{k}^2}{2\mu} \phi_{\mathbf{k}}^\nu - \sum_{\mathbf{q}} V_{\mathbf{q}} \phi_{\mathbf{k}+\mathbf{q}}^\nu = \varepsilon^\nu \phi_{\mathbf{k}}^\nu. \quad (3.6)$$

with the exciton binding energy ε^ν . This equation is commonly referred to as Wannier equation. In analogy to the hydrogen atom, the attractive interaction between electrons and holes results in a series of bound electron–hole (exciton) states with binding energies ε^ν , up to the scattering continuum where electrons and holes are not bound (see Fig. 3.1(b)). The exciton wavefunctions (Fig. 3.1(a)) resemble those of the hydrogen atom, although we remark here that the whole series of exciton states in a TMD cannot be described by the hydrogen model because of the non-local (momentum-dependent) dielectric function that arises from the finite thickness of the material.

The coordinate and basis transformation introduced here disregards the finite valley momentum of the electron and hole for simplicity, but can be generalized to consider the multi-valley band structure of TMDs. The resulting Wannier equation retains the form of Eq. (3.6) with a valley-specific reduced mass, giving rise to valley-dependent exciton binding energies. Due to the different binding energies in separate valleys, the exciton landscape can significantly differ from its free-electron counterpart. In particular, while

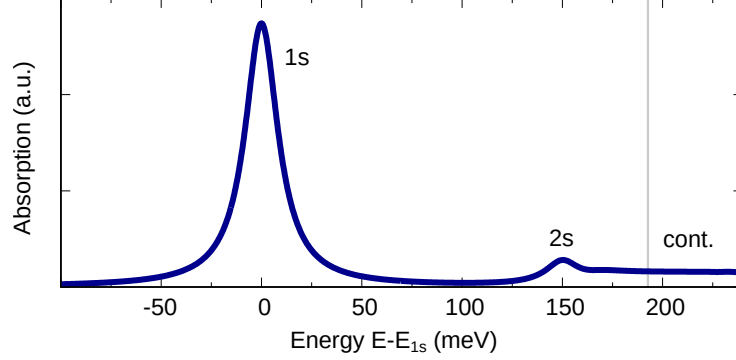


Figure 3.2: Optical absorption calculated for WS_2 encapsulated in hexagonal boron nitride (hBN). The 1s and 2s exciton peaks, as well as the scattering continuum are labeled. The grey line marks the single-particle band gap.

the free electron–hole energy in the $\text{K}\Lambda$ valley (i.e. K hole and Λ electron) is above that of KK , this situation is reversed in the exciton landscape of tungsten-based TMDs (cf. Fig. 3.1b). In this Chapter we focus on KK excitons, which are optically accessible due to their zero center-of-mass momentum. In Chapter 4, we will see that the multi-valley band structure of excitons in tungsten-based TMDs crucially impacts the exciton dynamics.

Excitonic resonances in optical spectra

After applying the exciton basis transformation to Eq. (3.3) we can easily find the excitonic polarization in the frequency domain,

$$P_{\mathbf{Q}}^{\nu}(\omega) = \frac{\Omega^{\nu}(\omega)\delta_{\mathbf{Q},0}}{\hbar\omega - E_{\text{g}} - \frac{\hbar^2\mathbf{Q}^2}{2M} - \varepsilon^{\nu} + i\gamma}, \quad (3.7)$$

where we have introduced the excitonic Rabi frequency, $\Omega^{\nu}(\omega) = \sum_{\mathbf{k}} \phi_{\mathbf{k}}^{\nu*} \Omega_{\mathbf{k}}(\omega)$. We also added a phenomenological damping γ to account for decoherence processes due to, e.g., phonon scattering. Now we can subsequently obtain the current density (3.2), the susceptibility (3.1), and the optical absorption

$$\alpha(\omega) = \frac{e_0^2}{nc\epsilon_0\omega m_0^2} \sum_{\nu} \frac{|M^{\nu}|^2 \gamma}{(\hbar\omega - E_0^{\nu})^2 + \gamma^2}. \quad (3.8)$$

Here we have defined the excitonic optical matrix element $M^\nu = \sum_{\mathbf{k}} \phi_{\mathbf{k}}^{\nu*} M_{\mathbf{k}}$ and the exciton resonance energy $E_0^\nu = E_g + \varepsilon^\nu$. This formula is usually known as Elliot formula². It illustrates that, due to the electron-hole attraction, optical absorption can occur only at particular energies E_0^ν corresponding to excitonic states ν that can be well below the band gap (see Fig. 3.2). Moreover, assuming a constant optical matrix element, $M_{\mathbf{k}}^{\text{cv}} \approx M_0$, the oscillator strength (area of the absorption peak) is given by $|M_0|^2 |\phi^\nu(\mathbf{0})|^2$, where $\phi^\nu(\mathbf{r}) = \sum_{\mathbf{k}} e^{i\mathbf{k}\cdot\mathbf{r}} \phi_{\mathbf{k}}^\nu$ is the probability to find an electron at a distance \mathbf{r} from a hole. The oscillator strength is thus given by the probability of an electron and a hole being at the same position. Therefore, the optical absorption at the exciton resonance is stronger for tightly-bound excitons, where the electron and the hole are more likely to be on top of each other.

3.2 Density-dependent spectra and the Mott transition

In the previous Section we have introduced the theoretical framework necessary to compute optical absorption, and applied it to the low-density regime to demonstrate the characteristic optical absorption of an excitonic semiconductor. Now, we allow for finite charge-carrier densities and investigate their impact on absorption spectra. In particular, we will see how the excitonic signatures become weak and eventually disappear at the Mott transition. Moreover, we study the possibility of achieving population inversion and the consequent optical gain that is a must for the realization of a laser. Here we present the main theoretical background and results. Further details can be found in Paper II and Refs. [35, 37, 58].

²We note that the Elliot formula is only approximately correct. When the light-matter coupling is strong, radiative dephasing becomes important and leads to an additional spectral broadening $\gamma \rightarrow \gamma + \gamma_{\text{rad}}^\nu$ in the denominator of Eq (3.8), with the radiative dephasing $\gamma_{\text{rad}}^\nu = e_0^2 / (2nc\epsilon_0 E_0^\nu m_0^2)$. This can be shown via a self-consistent treatment of the polarization and the electromagnetic wave [58].

Semiconductor Bloch equations

Strong photoexcitation generates a non-negligible population of conduction-band electrons and valence-band holes. In this regime, the microscopic polarization $p_{\mathbf{k}} = \langle e_{\mathbf{k}}^\dagger h_{\mathbf{k}} \rangle$ is described by the semiconductor Bloch equations,

$$\begin{aligned} \dot{p}_{\mathbf{k}} &= \left(\frac{i}{\hbar} \tilde{E}_{\mathbf{k}}^{\text{eh}} - \gamma_{\mathbf{k}} \right) p_{\mathbf{k}} + i (1 - f_{\mathbf{k}}^e - f_{\mathbf{k}}^h) \left(\Omega_{\mathbf{k}} - \frac{1}{\hbar} \sum_{\mathbf{q}} W_{\mathbf{q}} p_{\mathbf{k}+\mathbf{q}} \right), \\ \dot{f}_{\mathbf{k}}^\lambda &= 2 \operatorname{Im} \left[p_{\mathbf{k}} \tilde{\Omega}_{\mathbf{k}}^* \right] + \dot{f}_{\mathbf{k}}^\lambda \Big|_{\text{sc}} - \gamma_{\text{d}} f_{\mathbf{k}}^\lambda, \end{aligned} \quad (3.9)$$

where we have introduced the electron and hole occupations $f_{\mathbf{k}}^e = \langle e_{\mathbf{k}}^\dagger e_{\mathbf{k}} \rangle$ and $f_{\mathbf{k}}^h = \langle h_{\mathbf{k}}^\dagger h_{\mathbf{k}} \rangle$, respectively, and $\tilde{\Omega}_{\mathbf{k}}$ is the Rabi frequency renormalized by the Coulomb interaction. These equations describe the generation of interband polarization $p_{\mathbf{k}}$ due to the optical excitation and the transfer of coherent polarization into the incoherent population of electrons and holes. Importantly, finite carrier densities result in phase-space filling, dielectric screening, and renormalization of the free electron–hole pair energy. In the following, we describe these effects in detail:

- The **phase-space filling** factor $(1 - f_{\mathbf{k}}^e - f_{\mathbf{k}}^h)$ inhibits the generation of polarization by the incident light and the Coulomb binding that results in the formation of exciton states. In particular, when the electronic occupation in the conduction band is equal to that in the valence band ($f_{\mathbf{k}}^e = 1 - f_{\mathbf{k}}^h$), excitation and recombination processes induced by the external field cancel out, resulting in a complete suppression of optical absorption and excitonic effects. Moreover, population inversion ($f_{\mathbf{k}}^e > 1 - f_{\mathbf{k}}^h$) reverses the sign, resulting in an effectively repulsive electron–hole interaction and the stimulated emission of light.
- The additional³ **dielectric screening** is caused by the excited charge-carriers (electrons and holes), and results in the weakening of the Coulomb interaction, $W_{\mathbf{q}} = \epsilon_{\mathbf{q}}^{-1} V_{\mathbf{q}}$. The dielectric function $\epsilon_{\mathbf{q}}$ is obtained using the Lindhard formula in the static limit [67, 68]. While

³While the Coulomb interaction is already screened by the dielectric properties of the system in equilibrium, we are discussing here the additional screening coming from the excited charges.

this approach is sufficient to qualitatively describe the main effects of a large carrier density, a better quantitative description can, in principle, be obtained using more sophisticated approaches that consider dynamic effects [69] and screening arising from excitonic population [70, 71] (see also Paper XXI).

- The **energy renormalization** in $\tilde{E}_{\mathbf{k}}^{\text{eh}} = E_{\mathbf{k}}^{\text{e}} + E_{\mathbf{k}}^{\text{h}} + \Sigma_{\mathbf{k}}$ consists of two contributions, $\Sigma_{\mathbf{k}} = \Sigma_{\mathbf{k}}^{\text{CH}} + \Sigma_{\mathbf{k}}^{\text{SX}}$, commonly called Coulomb-hole (CH) and screened-exchange (SX) self-energies. The first term, $\Sigma_{\mathbf{k}}^{\text{CH}} = -\sum_{\mathbf{q}} (V_{\mathbf{q}} - W_{\mathbf{q}})$, describes a reduction of the band-gap due to the weakened electron–electron repulsion in the presence of many-particle dielectric screening. This is sometimes imagined as a *Coulomb hole* that surrounds the electron. The second term, $\Sigma_{\mathbf{k}}^{\text{SX}} = -\sum_{\mathbf{q}} W_{\mathbf{q}} (f_{\mathbf{k}+\mathbf{q}}^{\text{e}} + f_{\mathbf{k}+\mathbf{q}}^{\text{h}})$, describes a reduction of the electron and hole energies due to exchange interaction. Since the fermionic exchange interaction describes particles avoiding each other (Pauli-blocking), the decrease in energy is commonly described as a consequence of the *exchange hole* that surrounds each electron [35].⁴

We have also considered carrier–phonon scattering in the semiconductor Bloch equations which manifests in the dephasing $\gamma_{\mathbf{k}}$ and the scattering rate $\dot{f}_{\mathbf{k}}^{\lambda}|_{\text{sc}}$. These terms can be derived by exploiting the cluster expansion approach, considering carrier–phonon correlations of the form $\langle e_{\mathbf{k}}^{\dagger} e_{\mathbf{k}+\mathbf{q}} b_{\mathbf{q}}^{\dagger} \rangle^{\text{c}}$, truncating the remaining terms to single-particle expectation values, and finally applying the Markov approximation [34]. Moreover, we have added the phenomenological population decay γ_{d} to account for incoherent recombination processes.

⁴Both CH and SX terms can be obtained by considering the screened potential $W_{\mathbf{q}}$ at the level of the Hamiltonian and applying a Hartree-Fock approximation in the equation of motion. However, this formally leads to only the valence band being renormalized. The correct description—i.e. both conduction and valence bands become renormalized—is obtained by a consistent derivation of screening and renormalization considering the impact of correlations [62, 72].

Generalized Wannier equation and Elliot formula

The optical absorption can now be obtained using the procedure introduced in Section 3.1, i.e. expanding in exciton basis (3.5) and then calculating the current density. The exciton wave functions now satisfy a generalized Wannier equation,

$$\tilde{E}_{\mathbf{k}}^{\text{eh}} \phi_{\mathbf{k}}^{\nu(R)} - (1 - f_{\mathbf{k}}^{\text{e}} - f_{\mathbf{k}}^{\text{h}}) \sum_{\mathbf{q}} W_{\mathbf{q}} \phi_{\mathbf{k}+\mathbf{q}}^{\nu(R)} = \varepsilon^{\nu} \phi_{\mathbf{k}}^{\nu(R)}, \quad (3.10)$$

which takes into account the phase-space filling, dielectric screening, and energy renormalization effects. In particular, phase-space filling and dielectric screening weaken the formation of excitonic states, resulting in reduced or even vanishing exciton binding energies. Note that this eigenvalue problem is not Hermitian anymore and therefore demands distinct left and right eigenvectors [37, 58], $\phi_{\mathbf{k}}^{\nu(R)}$ and $\phi_{\mathbf{k}}^{\nu(L)}$.

The optical absorption now follows the generalized Elliot formula⁵,

$$\alpha(\omega) = \frac{e_0^2}{nc\epsilon_0\omega m_0^2} \gamma \sum_{\nu} \frac{\sum_{\mathbf{k}\mathbf{k}'} (1 - f_{\mathbf{k}}^{\text{e}} - f_{\mathbf{k}}^{\text{h}}) \phi_{\mathbf{k}}^{\nu(L)} M_{\mathbf{k}}^* \phi_{\mathbf{k}'}^{\nu(R)} M_{\mathbf{k}'}}{(\hbar\omega - E_0^{\nu})^2 + \gamma^2}. \quad (3.11)$$

Below population inversion, the complicated numerator can simply be expressed as $|M_0|^2 |\phi^{\nu(R)}(\mathbf{0})|^2$ if $M_{\mathbf{k}} \approx M_0$ is assumed and the relation $(1 - f_{\mathbf{k}}^{\text{e}} - f_{\mathbf{k}}^{\text{h}}) \phi_{\mathbf{k}}^{\nu(L)} = \phi_{\mathbf{k}}^{\nu(R)}$ is used [37, 58].

Visualizing the Mott transition in pump-probe spectroscopy

In Paper II, we consider an intense ultrashort optical excitation and investigate the evolution of the system. In experiments, the initial optical excitation is achieved by a strong pump pulse, whereas the time-resolved optical response of the system is measured via a delayed (weak) probe pulse. In

⁵The Elliot formula works well for undoped samples. In the presence of doping, trion signatures emerge in the optical absorption spectra. The evolution of exciton and trion absorption peaks as a function of doping can be well described in the Fermi-polaron picture, where the exciton is dressed by its interaction with the Fermi sea [73–76].

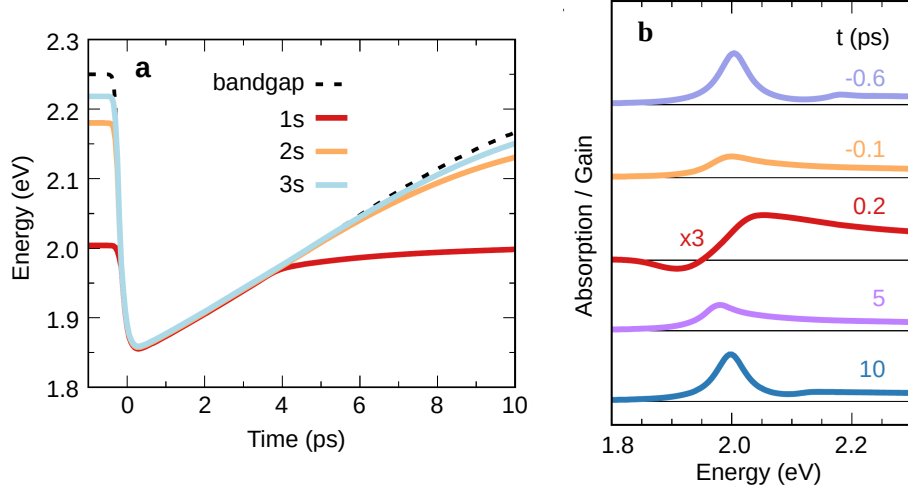


Figure 3.3: Influence of carrier density in the optical spectra of TMDs after an ultra-short optical excitation centered at $t = 0$. **a**: Time-dependent energy renormalization for the single-particle band gap and excitonic resonances. **b**: Absorption spectra at different times after the optical excitation. Adapted from Ref. [77] (Paper II).

our work, we obtain the time-dependent microscopic polarization and carrier occupations by solving the semiconductor Bloch equations (3.9), the excitonic binding energies and wave functions from the generalized Wannier equation (3.10), and the optical absorption from the generalized Elliot formula (3.11). The most illustrative results are shown in Fig. 3.3.

At moderate densities, the band gap renormalization (red-shift) is counteracted by the reduction of the exciton binding energy (blue-shift), resulting in a negligible shift of the 1s exciton resonance [37]. Here, however, we consider a very intense laser pulse that quickly generates a large carrier density, leading to the complete suppression of the exciton binding energies and to a large red-shift of the band gap (see Fig. 3.3a). The suppression of exciton binding energies marks the Mott transition from bound excitons to a plasma of unbound electrons and holes. After the optical excitation, the electrons and holes recombine and the excitonic states are slowly recovered.

In the optical absorption spectra, the 1s exciton peak is bleached due to phase-space filling and additionally weakened by the decrease of the oscillator

strength $\propto |\phi^{\nu(R)}(\mathbf{0})|^2$ as the exciton state becomes less bound (see Fig. 3.3b). Furthermore, in the extreme case of population inversion (which is achieved at $t = 0.2$ ps), the optical absorption reverses its sign, manifesting the effect of optical gain. Optical gain describes the situation in which the incident light, rather than being absorbed, stimulates the emission of more light. This effect is the basis for laser operation, and was experimentally observed in Ref. [26]. Besides bleaching and optical gain, we also capture the initial red-shift of the main absorption peak, followed by a blue-shift during the optical excitation, which has been experimentally observed [78]. While the red-shift directly follows from the band gap renormalization, the subsequent blue-shift is caused by the bleaching of the lowest possible transitions due to Pauli-blocking.

We have presented the main qualitative impact of finite carrier densities on optical absorption. In particular, we have shown how the Mott transition and even population inversion can be visualized in pump-probe spectroscopy. In Paper II, we also investigate the time evolution of carrier occupation and exciton wave functions. Moreover, we address the characteristic signatures of large carrier densities in differential absorption, which enables the visualization of weak changes in the spectra. Our work provides a framework to understand the features of high carrier densities and population inversion in the optical response of atomically thin semiconductors.

The methods and insights gained here have been later applied to other works. In particular, the calculations of density-dependent energy renormalization and suppression of exciton binding energy were employed to support the experimental observation of a continuous Mott transition in Paper XX. Furthermore, in Paper XXIII we have traced the large energy renormalization of the PL resonances in p-type InSe back to the large effective mass of holes, which leads to significant screening and Coulomb-hole renormalization.

CHAPTER 4

Exciton dynamics — Thermalization, dissociation, and propagation

After an optical excitation, the photogenerated excitons scatter with phonons and eventually reach thermal equilibrium with the lattice. This same scattering mechanism can induce the dissociation of excitons into unbound electron-hole pairs if the thermodynamic equilibrium between the two is broken (e.g. by a weak electric field dragging charge-carriers away). Furthermore, exciton-phonon scattering governs the diffusive propagation of excitons. A comprehensive understanding of the exciton thermalization, dissociation, and propagation dynamics would provide important insights into the potential and limitations of excitonic devices.

In this Chapter, we discuss these different aspects of exciton dynamics. First, we introduce the theoretical description of exciton-phonon scattering with an effective exciton Hamiltonian. After that, we examine the ultra-fast relaxation of excitons into energetically-favourable states that are optically inactive, which was observed in a joint theory-experiment collaboration (Paper III). We then tackle the problem of exciton dissociation assisted by

phonons (Paper IV). Finally, we present the theoretical description of exciton propagation and, in particular, unveil the origin of the ring-like exciton profile that arises at strong photoexcitation (Paper I).

4.1 Exciton–phonon scattering

At low photoexcitation densities, the dynamics of the system are governed by exciton–phonon scattering¹. One can follow the approach outlined in Section 2.4 to obtain the Hamiltonian describing a system of excitons and phonons,

$$\begin{aligned}
 H = & \sum_{\nu \mathbf{Q}} E_{\nu \mathbf{Q}} X_{\nu \mathbf{Q}}^{\dagger} X_{\nu \mathbf{Q}} + \sum_{j \mathbf{q}} \hbar \Omega_{j \mathbf{q}} b_{j \mathbf{q}}^{\dagger} b_{j \mathbf{q}} \\
 & + \sum_{j \nu \nu' \mathbf{Q} \mathbf{q}} G_{j \mathbf{q}}^{\nu \nu'} X_{\nu', \mathbf{Q} + \mathbf{q}}^{\dagger} X_{\nu \mathbf{Q}} \left(b_{j \mathbf{q}} + b_{j, -\mathbf{q}}^{\dagger} \right), \quad (4.1)
 \end{aligned}$$

where the exciton–phonon matrix element reads

$$\begin{aligned}
 G_{j \mathbf{q}}^{\nu \nu'} = & \langle \nu | \left(\delta_{\nu_h, \nu'_h} g_{j \mathbf{q}}^e e^{i \alpha_h \mathbf{q} \cdot \mathbf{r}} + \delta_{\nu_e, \nu'_e} g_{j \mathbf{q}}^h e^{-i \alpha_e \mathbf{q} \cdot \mathbf{r}} \right) | \nu' \rangle \\
 = & \sum_{\mathbf{k}} \phi_{\mathbf{k}}^{\nu *} \left(\delta_{\nu_h, \nu'_h} g_{j \mathbf{q}}^e \phi_{\mathbf{k} + \alpha_h \mathbf{q}}^{\nu'} + \delta_{\nu_e, \nu'_e} g_{j \mathbf{q}}^h \phi_{\mathbf{k} - \alpha_e \mathbf{q}}^{\nu'} \right). \quad (4.2)
 \end{aligned}$$

Here we have introduced the index ν containing both the exciton state (1s, 2s, 2p, ...) and valley configuration $\{\nu_h, \nu_e\}$ (KK, KK', K Λ , ...). The exciton–phonon coupling can be regarded as the sum of electron and hole components weighted by the wave function overlap of each transition. Importantly, electron (hole) scattering implies that the hole (electron) must remain in the same valley. Note that the hole-phonon coupling strength is related to that of valence-band electrons via $g_{j \mathbf{q}}^h = -g_{j \mathbf{q}}^v$. As mentioned in Section 2.2, the coupling to phonons is treated in a deformation potential approach. In order to account for the polar (non-polar) character of the interaction with optical (acoustic) phonons [51], we consider the electron and hole deformation potentials to have opposite (equal) sign. Finally, we note that the \mathbf{Q} -independent

¹In contrast, strong photoexcitation generates a large exciton density, giving rise to efficient exciton–exciton interactions. We have investigated the impact of exciton–exciton interaction on the recombination and propagation dynamics in Papers XIX, XXI, XXIV, and XXIX.

expression for the exciton-phonon coupling $G_{j\mathbf{q}}^{\nu\nu'}$ holds for intra- as well as inter-valley transitions as long as the initial and final states have a similar exciton mass [79].

Our aim is to describe the time evolution of the exciton population due to scattering with phonons. First of all, we note that the exciton population can be separated,

$$\langle X_{\nu\mathbf{Q}}^\dagger X_{\nu\mathbf{Q}} \rangle = \left| \langle X_{\nu\mathbf{Q}}^\dagger \rangle \right|^2 + \langle X_{\nu\mathbf{Q}}^\dagger X_{\nu\mathbf{Q}} \rangle^c, \quad (4.3)$$

that is, into an coherent part $P_{\mathbf{Q}}^\nu = \langle X_{\nu\mathbf{Q}}^\dagger \rangle$ describing excitonic interband polarization, and an incoherent part $N_{\mathbf{Q}}^\nu = \langle X_{\nu\mathbf{Q}}^\dagger X_{\nu\mathbf{Q}} \rangle^c$ describing the occupation of exciton states. The equation of motion for the exciton occupation $N_{\mathbf{Q}}^\nu$ due to exciton-phonon scattering reads

$$\left. \frac{dN_{\mathbf{Q}}^\nu}{dt} \right|_{\text{x-phon}} = \frac{2}{\hbar} \sum_{\nu'\mathbf{q}\pm} \text{Im} \left[G_{j\mathbf{q}}^{\nu'\nu} S_{\mathbf{Q}\mathbf{q}}^{\nu\nu'j\pm} \right], \quad (4.4)$$

where $S_{\mathbf{Q}\mathbf{q}}^{\nu\nu'j\pm} = \langle X_{\nu\mathbf{Q}}^\dagger X_{\nu'\mathbf{Q}-\mathbf{q}} b_{j,\pm\mathbf{q}}^{(\dagger)} \rangle^c$ (with $b_{\mathbf{q}}$ for the + sign) is the exciton-phonon correlation describing a phonon-assisted exciton transition. The equation of motion for S can be simplified by applying the cluster expansion and truncating to single-particle occupation numbers for excitons and phonons, yielding

$$\begin{aligned} i\hbar \frac{dS_{\mathbf{Q}\mathbf{q}}^{\nu\nu'j\pm}}{dt} &= (E_{\nu',\mathbf{Q}-\mathbf{q}} - E_{\nu\mathbf{Q}} \pm \hbar\Omega_{j\mathbf{q}}) S_{\mathbf{Q}\mathbf{q}}^{\nu\nu'j\pm} \\ &\quad + G_{j,-\mathbf{q}}^{\nu\nu'} \left(N_{\mathbf{Q}}^\nu \eta_{j\mathbf{q}}^\pm - N_{\mathbf{Q}-\mathbf{q}}^{\nu'} \eta_{j\mathbf{q}}^\mp \right), \end{aligned} \quad (4.5)$$

where $\eta_{j\mathbf{q}}^\pm = \langle b_{j\mathbf{q}}^\dagger b_{j\mathbf{q}} \rangle^c + (1 \pm 1)/2$ is the effective phonon number for absorption (−) and emission (+) processes. Here, we have further assumed that coherent phonons (which describe a net displacement of the whole lattice) are not present in the system, and disregarded nonlinear terms in the exciton occupation which should be relevant mostly at large densities and low temperature. The equation for S can be now analytically solved with the Markov approximation introduced in Section 2.3. The resulting equation for

the exciton occupation reads

$$\begin{aligned} \left. \frac{dN_{\mathbf{Q}}^{\nu}}{dt} \right|_{\text{x-phon}} &= \frac{2\pi}{\hbar} \sum_{\nu' \mathbf{q} \pm} \left| G_{j\mathbf{q}}^{\nu'\nu} \right|^2 (N_{\nu', \mathbf{Q}-\mathbf{q}} \eta_{j\mathbf{q}}^{\mp} - N_{\mathbf{Q}}^{\nu} \eta_{j\mathbf{q}}^{\pm}) \\ &\times \delta(E_{\nu', \mathbf{Q}-\mathbf{q}} - E_{\nu, \mathbf{Q}} \pm \hbar \Omega_{j\mathbf{q}}), \end{aligned} \quad (4.6)$$

i.e. within the approximations applied, we obtain the exciton–phonon scattering rate in the form of Fermi’s golden rule. Here, we can identify the in-scattering rate from $|\nu', \mathbf{Q} - \mathbf{q}\rangle$ into $|\nu, \mathbf{Q}\rangle$ and the opposite out-scattering rate. Solving this equation gives access to the time-, momentum- and energy-resolved exciton dynamics.

The optical excitation can be included in the model by taking into account the generation of excitonic polarization $P_{\mathbf{Q}}^{\nu}$ by the incident light. The polarization-to-population transfer appears naturally in the model when considering the exciton–phonon interaction in the equation of motion for $P_{\mathbf{Q}}^{\nu}$. The resulting equations of motion for coherent and incoherent exciton populations can be found in the supplementary material of Paper III.

4.2 Exciton thermalization

In this Section, we apply our model to investigate exciton thermalization mediated by exciton–phonon scattering. In particular, we discuss the ultrafast relaxation of bright excitons into dark states, which was investigated in a joint experiment–theory work in Paper III. First, we introduce the exciton energetic landscape to illustrate the relevance of momentum-dark excitons. After that, we provide an overview of Paper III.

Exciton landscape

In Section 2.2, we introduced the band structure of TMDs (Fig. 2.1), which exhibits conduction-band minima at the $K^{(\prime)}$ and $\Lambda^{(\prime)}$ points of the Brillouin zone and valence-band maxima at $K^{(\prime)}$ and Γ . Excitonic states exist in all possible combinations of electron and hole valleys, e.g. KK , $K\Lambda$, KK' , ΓK ,

etc. However, due to the small momentum carried by photons, only KK and K'K' excitons with zero center-of-mass momentum can be optically active. For this reason, these are called bright states, while states with a momentum too large to be accessed by light are called momentum-dark states.²

Due to the dependence of the exciton binding energy on the valley-specific reduced mass, exciton states might lie in a different ordering than the corresponding free electron-hole states. In particular, in tungsten-based TMDs, exciton states at the KA and KK' valleys are the ones with lowest energy (as was introduced already in Fig. 3.1). Therefore, these materials exhibit an indirect band gap. This fact has major implications for the exciton dynamics [12]. In particular, optically generated excitons at KK will relax into the energetically lower dark states (see Fig. 4.1(a)), which will then dominate the recombination and propagation dynamics. Since excitons in such states cannot directly recombine and emit light [83], the radiative recombination time in these materials is rather slow [84, 85]. This property is very relevant for optoelectronic devices such as photodetectors and solar cells, where the recombination is desired to be slow in order not to lose the charge carriers that generate electric current.

Visualizing dark exciton formation in ARPES

The experimental detection of dark exciton states has been until recently only indirect, via optical features such as absorption linewidth [66] and phonon-assisted photoluminescence [83]. For example, in Paper XI we showed that the formation of dark excitons can be indirectly visualized in time-resolved PL spectra via the emergence of phonon sidebands. A tool that allows to directly map the whole energy and momentum landscape is angle-resolved photoemission spectroscopy (ARPES), where the electron energy and momentum is accurately determined. Time-resolved (tr)ARPES has recently

²Bright excitons in TMDs are composed of an electron and a hole with opposite spin (in other words, conduction- and valence-band states with equal spin)—therefore they are sometimes called singlet excitons. Excitons formed by electrons and holes with equal spin are dark (or couple weakly to light polarized in the direction perpendicular to the layer) and are commonly referred to as triplet excitons [80]. Throughout this work we disregard the effect of spin-dark states in the dynamics since their formation time is expected to be slow compared to states where electron and hole have the same spin [81, 82].

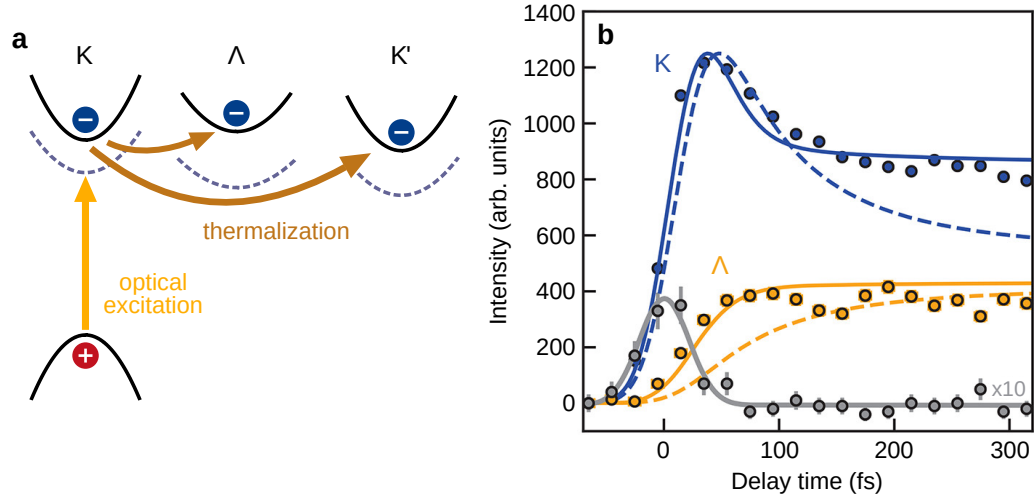


Figure 4.1: Dark-exciton formation resolved by trARPES. **a**: Illustration of the process. An optical excitation generates an electron-hole pair that thermalizes throughout the Brillouin zone. The solid (dashed) lines represent single-particle bands (exciton binding). **b**: ARPES signal (circles) and theoretical simulations of the electron occupation (dashed and solid lines) around each symmetry point. Gray dots and line are measurements and a Gaussian fit of the ARPES signal at the Γ point, which is a replica of the valence band that appears during the pulse excitation. Figure adapted from Ref. [86] (Paper III).

been exploited to visualize the formation of momentum-dark $K\Lambda$ excitons in monolayer WSe_2 after photoexcitation [87]. In Paper III, Robert Wal-lauer and colleagues (Marburg, Germany) directly observed the formation of momentum-dark excitons in WS_2 at room temperature with an impressive temporal resolution on the order of 10s of femtoseconds. In the trARPES experiment, a coherent exciton population at the KK and $K'K'$ valleys is generated by a linearly-polarized laser pulse. Coherent excitons with zero center-of-mass momentum quickly scatter with phonons and are transferred into incoherent population with finite momenta at the energetically lower KK' , $K\Lambda$ states³ (see Fig. 4.1(a)) and their opposite-spin counterparts in the $K'K$ and $K'\Lambda'$ valleys. The experiment, however, probes electrons and not whole excitons. Following the expansion scheme introduced in Section 2.4, the electron occupation at the valley v and with momentum \mathbf{k} can be ex-

³Note that in Paper III Σ is used for the symmetry point that we call Λ . In literature, this symmetry point is called Σ , Λ , or Q .

pressed in terms of the exciton occupation,

$$f_{\mathbf{k}}^v = \sum_{\nu_v \mathbf{Q}} |\phi_{\mathbf{k}-\alpha_e \mathbf{Q}}^{\nu_v}|^2 (|P_{\mathbf{0}}^{\nu_v}|^2 \delta_{\mathbf{Q} \mathbf{0}} + N_{\mathbf{Q}}^{\nu_v}), \quad (4.7)$$

where ν_v refers to any exciton state with an electron in the valley v . Thus, the electron occupation probed by the trARPES experiment reflects both coherent and incoherent exciton populations modeled by our microscopic theory.

The measured and predicted electron occupations at K and Λ are shown in Fig. 4.1(b), where the ultra-fast relaxation in a timescale of tens of femtoseconds is clearly observed. Concretely, one can see that the electron population at the K valley rises during the optical excitation. Shortly after, the K population decreases slightly, while the Λ population increases as electrons scatter from K into Λ . This can be understood in the exciton picture as KK excitons being optically generated and then scattering into the energetically favourable K Λ and K K' states. Due to the linear polarization of the pump pulse, K' K' excitons are also optically generated and scatter into the K' Λ' and K' K states. Therefore, the ARPES signal in the K $^{(\prime)}$ valley remains large, reflecting the dominating population of K K' and K' K excitons, while the lower but significant signal in the Λ valley reflects the important population of K Λ and K' Λ' excitons. The time-resolved visualization of exciton thermalization across the Brillouin zone thus provides a direct measure of the characteristic exciton–phonon scattering rates for intervalley transitions in TMDs. In Paper III, we discuss the formation of dark excitons in detail and, in addition, provide insights on the impact of off-resonant excitations.

4.3 Phonon-assisted exciton dissociation

Electrons and holes in TMDs are tightly-bound, forming excitons. Due to their charge neutrality, excitons cannot generate an electric current—only unbound electrons and holes can. Therefore, in order to generate an electric current, excitons must first *dissociate* into free electrons and holes. Since the dissociation process can be slow compared to transport, it poses a fundamental limit for the photoresponse in TMD-based photodetectors.

Previous works have studied the dissociation of excitons assisted by an external (in-plane) electric field [88–90]. This mechanism consists in bound excitons tunneling into the continuum of unbound electron-hole states—a process that is facilitated by the bending of the potential landscape caused by the applied field. However, extremely large electric fields are needed to dissociate tightly bound excitons with binding energies of hundreds of meV. For smaller electric fields—more suitable for technological applications—dissociation will still occur but by other means. The mechanism that dominates at small electric fields and low exciton densities is *phonon-assisted* dissociation. In Paper IV, we tackle the problem of exciton dissociation via scattering with phonons and disentangle the most important underlying mechanisms. Here, we outline the theoretical description of this process and summarize the main results of our work.

Plane wave approximation for unbound states

While up to now we have focused on the lowest exciton states (i.e., 1s), here we need to consider the whole Rydberg-like series of states, from the 1s state to the continuum of unbound states (cf. Fig. 3.1). As sketched in Fig. 4.2, excitons scatter with phonons to reach higher energetic states, and eventually dissociate into unbound electrons and holes by scattering into the continuum. The wave functions of both bound and continuum exciton states enter our model through the exciton–phonon matrix elements (4.2). All these states are obtained by numerically solving the Wannier equation. However, the wave functions of continuum states are badly resolved in momentum space because they resemble a Dirac delta and their implementation in the exciton–phonon matrix elements is numerically demanding. To overtake this problem, one can describe the continuum states as plane waves—that is, the exciton index can be mapped into a continuous momentum (wavevector), i.e. $\nu \rightarrow \mathbf{p}$, and we specify the wave function of continuum states as $\psi_{\mathbf{k}}^{\mathbf{p}} \sim \delta_{\mathbf{p}\mathbf{k}}$. This corresponds to treating electrons and holes as being completely free and uncorrelated. Although this description does not capture characteristic features of Coulomb-correlated electron-hole pairs such as the Sommerfeld enhancement of optical absorption [91, 92], it reduces the numerical complexity of the problem significantly. The exciton wave function for continuum states is

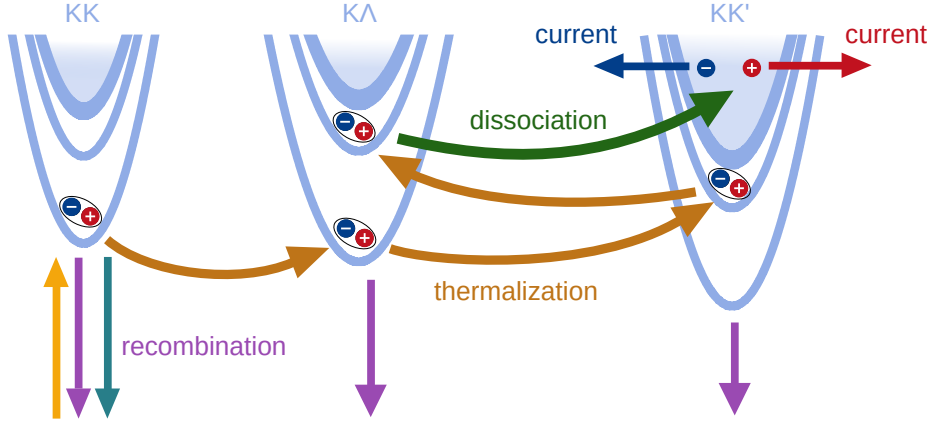


Figure 4.2: Schematic representation of exciton thermalization and dissociation in tungsten-based TMDs. Excitons are generated by an optical excitation in the KK valley. Then they scatter with phonons to reach a thermal equilibrium distribution, even dissociating into unbound electrons and holes. A weak external electric field drags the free carriers away, breaking the thermodynamic equilibrium and forcing a continuous dissociation. Excitons can recombine radiatively at KK or non-radiatively all around the Brillouin zone. Figure taken from Ref. [94] (Paper IV).

thus described by orthogonalized plane waves (OPWs),

$$\phi_{\mathbf{k}}^{\nu} \rightarrow \psi_{\mathbf{k}}^{\mathbf{p}} = \delta_{\mathbf{k}\mathbf{p}} - \sum_{\nu}^{N_b} \phi_{\mathbf{p}}^{\nu*} \phi_{\mathbf{k}}^{\nu}, \quad (4.8)$$

where $\phi_{\mathbf{k}}^{\nu}$ is the wave function of the bound state ν and N_b is the number of bound states considered. The first term corresponds to the momentum representation of a plane wave, whereas the second term ensures that continuum states are orthogonal with respect to the bound states. This orthogonalization is necessary to obtain a complete set of wave functions and thus avoid unphysical overlaps [93]. More details on the OPW approach can be found in the supplementary material of Paper IV.

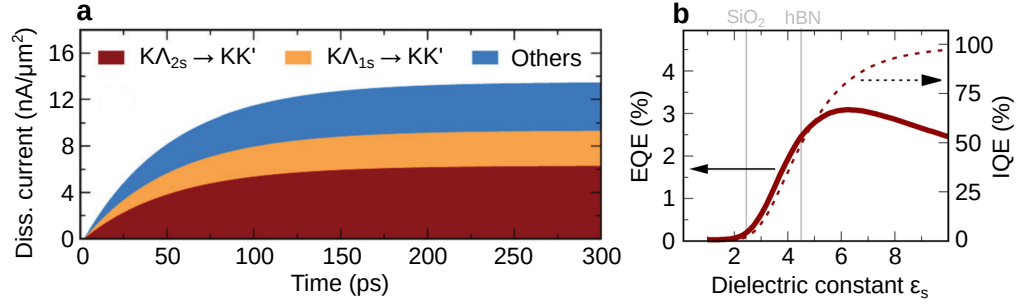


Figure 4.3: **a**: Dissociation current as a function of time, disentangled into the main channels. **b**: External (solid) and internal (dashed) quantum efficiencies as a function of the dielectric constant of the substrate or environment. Gray lines mark the dielectric constants corresponding to a SiO_2 substrate and hBN encapsulation. All simulations were performed for hBN-encapsulated WSe_2 . Figure adapted from Ref. [94] (Paper IV).

Exciton dissociation

In Paper IV, we consider a continuous optical excitation and study the microscopic mechanisms that govern exciton dissociation in the stationary state⁴. We compute the dissociation current and disentangle it into the main contributions (see Fig. 4.3(a)). In this way, we are able to identify the main dissociation channels. In particular, for WSe_2 we find that most dissociation originates from excitons in the KA valley that scatter into the unbound continuum of KK' . This is a consequence of the strong coupling with phonons of this inter-valley scattering channel. Furthermore, we are able to discern that it is mostly excitons in the $2s$ state that dissociate because of a trade-off between larger dissociation rates and lower occupation at higher energies closer to the continuum. The similarity between the dissociation-limited response time obtained of 50-100 ps and the one reported in Ref. [88] at small electric fields supports the validity of our model.

⁴In equilibrium conditions, at non-zero temperatures below the Mott transition, there is always a finite population of unbound electron-hole pairs due to entropy ionization [71, 95–97]. We assume that the thermodynamic equilibrium between bound and unbound populations is broken by a weak external electric field. With this assumption we can consider the continuum states to be completely empty, as dissociated charge-carriers are immediately dragged away by the electric field.

These findings are important to understand and predict the limitations and tunability of TMD-based photodetectors. For instance, the relative position of the Λ valley is strongly influenced by strain [98]. Thus, strain is a powerful knob that can be exploited to tune the photoresponse of TMDs. In Paper IV, we study the influence of excitation energy, non-radiative recombination, dielectric screening, temperature, and strain on the photoresponse. Here, we show the impact of the dielectric constant of the environment, ε_s . We evaluate the external (EQE) and internal quantum efficiency (IQE), which are the ratio of excitons that dissociate with respect to the number of incident and absorbed photons, respectively. Raising the dielectric constant ε_s , we find that both EQE and IQE increase (see Fig. 4.3(b)), reflecting the more efficient dissociation of less bound excitons that lie energetically closer to the continuum. For even stronger screening, however, we find that the EQE decreases due to the weakening of the optical absorption (weakly bound excitons exhibit lower oscillator strength). The trade-off between dissociation and optical absorption results in the prediction that, for photodetectors, hBN encapsulation is a more optimal environment than a SiO_2 substrate.

In Paper IV, we thoroughly describe the microscopic mechanisms behind exciton dissociation. Besides disentangling the main dissociation channels and understanding why they dominate, we also resolve the exciton pathway by identifying the transitions with strongest scattering rate. Moreover, we provide a comprehensive study on the tunability of key quantities (EQE, IQE, response time) with external knobs and compare the performance of the four most relevant semiconducting TMDs.

4.4 Exciton propagation

So far, we have considered that the system is homogeneously excited, i.e. the exciton density is the same in all positions. However, it is interesting to consider inhomogeneous excitations as they open the door to the study of propagation phenomena. In experiments, the system is optically excited with a laser spot that is significantly smaller than the sample. Excitons generated in the excitation spot diffuse away into the unpopulated (unexcited) regions. As excitons recombine radiatively and emit light, their propagation can be directly tracked in spatially- and temporally-resolved photoluminescence (PL)

measurements. In this Chapter, we introduce the Wigner function framework, which allows us to describe spatiotemporal dynamics, and present our work on exciton diffusion (Paper I).

Wigner function

The single-particle density or probability distribution $n(\mathbf{r})$ is defined as

$$n(\mathbf{r}) = \langle \Psi^\dagger(\mathbf{r}) \Psi(\mathbf{r}) \rangle. \quad (4.9)$$

Transforming the field operator into momentum space, $\Psi(\mathbf{r}) = \sum_{\mathbf{k}} e^{i\mathbf{k}\cdot\mathbf{r}} a_{\mathbf{k}}$, we obtain an expression for $n(\mathbf{r})$ depending only on the momentum-space creation and annihilation operators,

$$n(\mathbf{r}) = \sum_{\mathbf{k}\mathbf{k}'} e^{i(\mathbf{k}'-\mathbf{k})\cdot\mathbf{r}} \langle a_{\mathbf{k}}^\dagger a_{\mathbf{k}'} \rangle. \quad (4.10)$$

It is very important to note here that a homogeneous distribution, $n(\mathbf{r}) = n(0)$, implies that only diagonal components of the expectation value—i.e. occupation numbers—are non-zero. Therefore, off-diagonal components $\langle a_{\mathbf{k}}^\dagger a_{\mathbf{k}'} \rangle$ contain information about spatial inhomogeneities. In this context, we introduce the Wigner function,

$$f_{\mathbf{k}}(\mathbf{r}) = \sum_{\mathbf{q}} e^{i\mathbf{q}\cdot\mathbf{r}} \langle a_{\mathbf{k}-\frac{1}{2}\mathbf{q}}^\dagger a_{\mathbf{k}+\frac{1}{2}\mathbf{q}} \rangle, \quad (4.11)$$

which provides a much more intuitive framework to describe the spatial dependence. The Wigner function is a quasiprobability distribution in the phase-space of position \mathbf{r} and momentum \mathbf{k} . The density now simply reads

$$n(\mathbf{r}) = \sum_{\mathbf{k}} f_{\mathbf{k}}(\mathbf{r}). \quad (4.12)$$

While the equations of motion for $\langle a_{\mathbf{k}}^\dagger a_{\mathbf{k}'} \rangle$ can be obtained directly from Heisenberg's equation of motion, their numerical solution is highly demanding. On the other hand, the respective equations for $f_{\mathbf{k}}(\mathbf{r})$ are numerically solvable but their derivation requires some efforts. One approach is to use Moyal brackets [99]. The approach we use was first introduced by Hess and

Kuhn [100] and consists in first finding the equation of motion for $\langle a_{\mathbf{k}}^\dagger a_{\mathbf{k}'} \rangle$ and then Fourier-transforming to obtain the Wigner function $f_{\mathbf{k}}(\mathbf{r})$. By Taylor-expanding the appearing terms, one can find the lowest-order contributions⁵, which we will directly write below.

Conventional diffusion

The equation of motion for the exciton Wigner function $N_{\mathbf{Q}}(\mathbf{r})$ can be obtained following Ref. [100] and reads

$$\dot{N}_{\mathbf{Q}}(\mathbf{r}, t) = -\mathbf{v}_{\mathbf{Q}} \cdot \nabla_{\mathbf{r}} N_{\mathbf{Q}}(\mathbf{r}, t) + \dot{N}_{\mathbf{Q}}(\mathbf{r}, t) \Big|_{\text{x-phon}}. \quad (4.13)$$

The first term describes propagation of excitons with velocity $\mathbf{v}_{\mathbf{Q}} = \hbar \mathbf{Q} M_X^{-1}$, where M_X is the total exciton mass. The second term contains contributions accounting for exciton–phonon scattering, which we assume to be local and are thus the same as in Eq. (4.6). Here we assumed low exciton densities so that exciton–exciton interactions can be ruled out.⁶ Moreover, while in general one should consider multiple exciton valleys to describe the dynamics, in Paper IX we found that exciton diffusion in WS_2 is dominated by KA excitons, which constitute the majority of the population.

We now consider that the initial exciton Wigner function follows a spatial Gaussian profile determined by the laser pulse. Moreover, the system is at room temperature where exciton–phonon scattering is very efficient. Therefore, the exciton distribution can be assumed to be in thermal equilibrium already at the beginning of the simulation. Spatial profiles of the exciton density obtained by numerically solving (4.13) with these initial conditions are shown in Fig. 4.4a. One can clearly see that the exciton density retains the initial Gaussian shape and broadens as excitons diffuse away from the

⁵Higher-order terms in the Taylor expansion usually become relevant for spatially-narrow distributions or potentials and describe phenomena such as non-local scattering and tunneling [101].

⁶Exciton–exciton interactions become relevant at large exciton densities ($\sim 10^{12} \text{ cm}^{-2}$). They are particularly important for interlayer excitons in van der Waals heterostructures, where the repulsive exciton–exciton interaction enhances the exciton diffusion (see Papers XXI, XXIV, and XXIX).

excitation spot (cf. red arrow). Note that the distribution is normalized at each time frame to illustrate the broadening.

While we solve Eq. (4.13) as it is, the problem can be significantly simplified by taking some realistic assumptions. In particular, it can be assumed that the exciton distribution becomes thermalized immediately in the time scale of propagation [100]. Then, one finds that the time evolution of the exciton density, $N(\mathbf{r}, t) = \sum_{\mathbf{Q}} N_{\mathbf{Q}}(\mathbf{r}, t)$, obeys Fick's law,

$$\dot{N}(\mathbf{r}, t) = D \nabla^2 N(\mathbf{r}, t). \quad (4.14)$$

The exciton diffusion coefficient D can be related to the band structure and exciton–phonon scattering rates. Assuming a momentum-independent scattering rate τ^{-1} , one recovers the well known relation $D = \tau k_B T M_X^{-1}$. Considering that the initial exciton spatial distribution follows a Gaussian profile with a variance σ_0 , exciton diffusion leads to a broadening of the Gaussian profile with the variance evolving linearly in time, $\sigma^2(t) = \sigma_0^2 + 4Dt$. In summary, exciton propagation is in general diffusive (as in Fig. 4.4(a)) at low densities and room temperature, where exciton–phonon scattering is efficient, and can be simply described by the conventional Fick's law. Several experiments have studied the propagation of excitons by performing time- and space-resolved photoluminescence (PL) measurements [95, 102–105]. These works reported the diffusive propagation of excitons at low densities with diffusion coefficients on the order of $1 - 10 \text{ cm}^2/\text{s}$, in agreement with our theoretical predictions in Papers I, IX, X, XVII, and XIII. In Papers IX and XVIII, we investigate the impact of non-equilibrium distributions and slow thermalization times on exciton propagation, finding interesting phenomena such as negative diffusion (i.e. shrinking of the exciton spatial profile).

Non-linear propagation and halo formation

Conventional diffusion has been experimentally verified for low exciton densities. However, Kulig et al. observed that increasing the excitation density results in a faster diffusion and, eventually, the formation of ring-shaped PL profiles or halos in WS_2 [102]. This first study already pointed to exciton–exciton annihilation (EEA) as the possible origin of this phenomenon. However, EEA by itself could only explain the flattening of the Gaussian-like profile, but not the formation of halos.

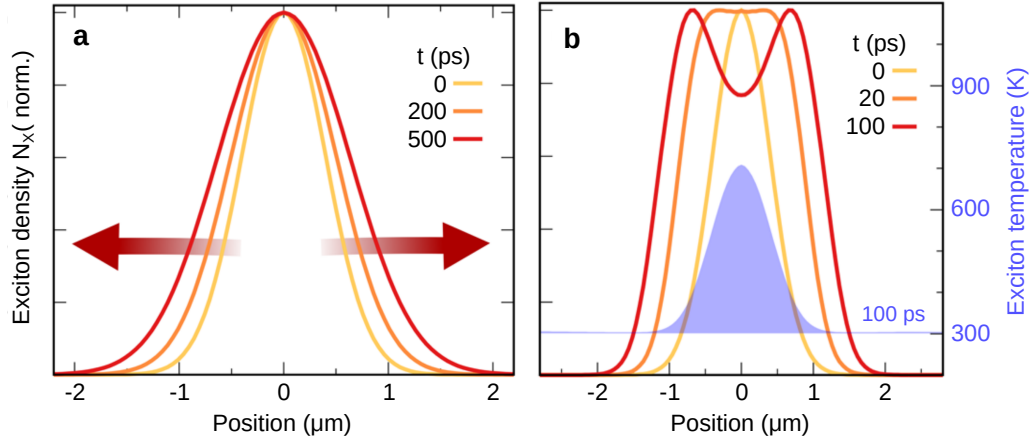


Figure 4.4: Time snaps of the spatial exciton distribution at **a**: low and **b**: high densities. The red arrows in **a** illustrate the diffusion process. The blue-shaded curve in **b** corresponds to exciton temperature (right axis). Figure adapted from Ref. [106] (Paper I).

EEA is an Auger-like recombination process where two excitons scatter and one of them is annihilated whereas the other gains the corresponding energy. The exciton density thus decays following $\dot{N}(\mathbf{r}, t) = -r_A N^2(\mathbf{r}, t)$. Since the Auger coefficient r_A can be extracted from time-dependent photoluminescence measurements [104], we can set up a semi-phenomenological model to describe the Auger recombination of an exciton with momentum \mathbf{Q} , that is $\dot{N}_{\mathbf{Q}}(\mathbf{r}, t) \Big|_A = -r_A N_{\mathbf{Q}}(\mathbf{r}, t) N(\mathbf{r}, t)$. This equation describes the annihilation of an exciton at \mathbf{Q} with an exciton in any state. We do not directly resolve the resulting high-energy exciton, but model its effect in the following way. The high-energy exciton resulting from Auger recombination will relax toward the ground state by emitting a cascade of phonons. Until now, we have treated phonons as a thermal bath. However, this sort of process where many excitons dissipate a large amount of energy by scattering with phonons will result in significantly increased non-equilibrium phonon populations that overheat the excitons. We take this into account by considering the equation of motion for the phonon number, including phonon emission cascade in a phenomenological manner by assuming that the exciton energy is completely transferred to the phonons. The final equations of motion describing the system can be found in Paper I.

Solving the coupled equations of motion for excitons and phonons indeed gives rise to the formation of exciton halos at elevated densities (see Fig. 4.4b). Remarkably, the formation and evolution of the exciton halo as a function of excitation density predicted by our model is in very good agreement with experimental measurements provided by the group of Alexey Chernikov (see Fig. 4 in Paper I). Moreover, we compute an effective exciton temperature, allowing us to identify that Auger recombination and the subsequent phonon emission cascade results in the heating of the exciton distribution. Importantly, the heating is more pronounced at the center of the excitation area, where the exciton density is largest, resulting in a temperature gradient (see blue shaded area in Fig. 4.4b). In order to obtain an intuitive understanding of the connection between the temperature gradient and the evolution of the exciton profile into a halo, we derive a macroscopic transport equation similar to Eq. (4.14). While the conventional diffusion equation only considers a density gradient, we now need to consider the temperature gradient as well. Taking into account that the exciton equilibrium distribution has a space-dependent temperature $T(\mathbf{r})$, the current density reads

$$\mathbf{j}(\mathbf{r}, t) = -D\nabla_{\mathbf{r}}N(\mathbf{r}, t) - s\nabla_{\mathbf{r}}T(\mathbf{r}, t), \quad (4.15)$$

where we have introduced the exciton Seebeck coefficient $s \approx \tau k_{\text{B}} N M_{\text{X}}^{-1}$. The term $s\nabla T$ describes thermal drift and accounts for excitons moving from hotter to colder regions. This simple equation provides a good understanding of the non-linear propagation and halo formation. Initially, a strong thermal drift will result in a flat (super-Gaussian) density distribution, as excitons in the hot central region will propagate out faster than excitons in colder outer regions. This phenomenon already results in non-linear propagation, i.e. $\sigma^2(t)$ does not evolve linearly with time. Moreover, if thermal drift is strong enough, the central region will continue to be depleted at a faster pace than excitons diffusing back. A significant temperature gradient can thus lead to the formation of a ring-like shape in the spatial exciton distribution (see Fig. 4.5). Our microscopic model was able to prove that the Auger-recombination and the subsequent hot-phonon emission can heat the exciton population, leading to the observed non-trivial exciton propagation at large excitation densities.

In a later work, we have showed that the heating effects are not so strong in hBN-encapsulated TMDs due to the suppressed Auger scattering in this dielectric environment (Paper X). Furthermore, in Paper XIX we have unveiled

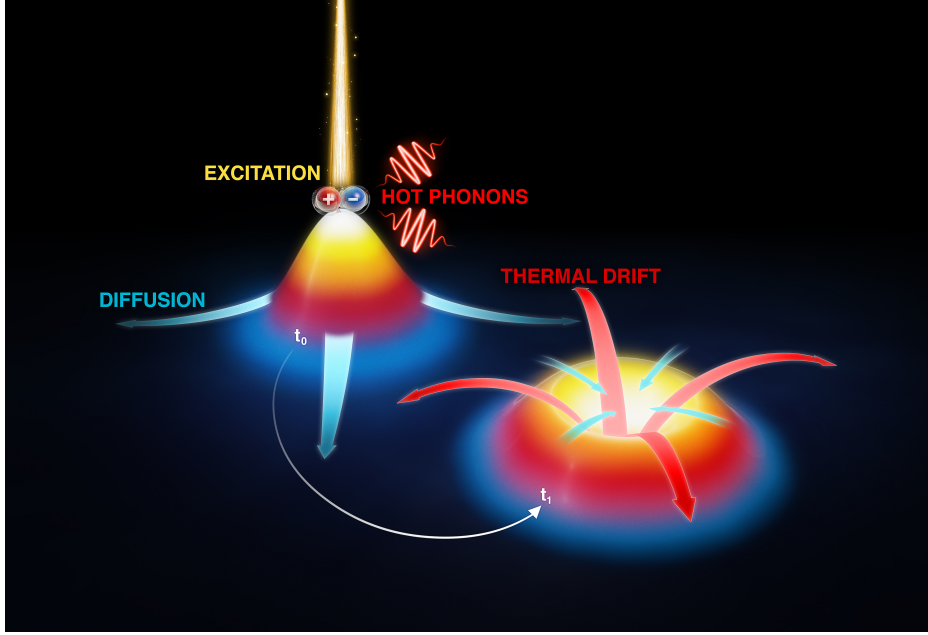


Figure 4.5: Schematic illustration of exciton propagation and halo formation. First, an optical excitation generates excitons that diffuse in order to homogenize the spatial distribution (t_0). Auger scattering and relaxation via phonon emission creates a long-lived spatial gradient in the exciton temperature (color gradient). The temperature gradient results in a strong thermal drift that drags excitons out of the central region, giving rise to the formation of a ring-shaped exciton distribution (t_1). Figure taken from Ref. [106] (Paper I).

the mechanisms behind Auger recombination, and showed that the reduced Auger recombination in hBN compared to SiO_2 substrate is a result of the weaker Coulomb interaction and less optimal energetic landscape.

CHAPTER 5

Trion dynamics — Trion–phonon scattering, transport, and photoluminescence

In the presence of doping, photogenerated excitons bind to additional charges and form trions. In this Chapter, we discuss different aspects of trion dynamics that have a significant impact on a material’s properties.

First, we introduce Paper V. Here, we reveal the substructure of ground and excited trion states. Focusing on the ground state, we investigate the trion–phonon interaction and its impact on transport. Moreover, we address the influence of the fermionic nature of trions on diffusion.

Finally, we present Paper VI, where we develop a model to describe the radiative recombination of bright and dark trions via direct recombination or assisted by phonons. In this work, we predict so far unseen signatures of trions in PL spectra. Moreover, we study how the stability and PL resonance of trions are influenced by the mass imbalance between the two electrons within the trion.

5.1 Trion–phonon scattering and transport

In this Section, we discuss Paper V. The aim of this work is to provide a framework to describe trion dynamics. For that purpose, we derive a trion Hamiltonian following the Fock space truncation scheme described in Section 2.4.

We start by considering the Hamiltonian of the system of interacting electrons and holes, where the two electrons forming the trion are located in two distinct valleys¹. We adopt the notation $e_{\mathbf{k}}$ and $e'_{\mathbf{k}}$ to refer to electron operators acting on states in the two distinct valleys. The Hamiltonian for this system reads

$$H_t = \sum_{\mathbf{k}} \left(E_{\mathbf{k}}^e e_{\mathbf{k}}^\dagger e_{\mathbf{k}} + E_{\mathbf{k}}^{e'} e_{\mathbf{k}}'^\dagger e_{\mathbf{k}}' + E_{\mathbf{k}}^h h_{\mathbf{k}}^\dagger h_{\mathbf{k}} \right) + \sum_{\mathbf{k}\mathbf{k}'\mathbf{q}} V_{\mathbf{q}} \left(e_{\mathbf{k}+\mathbf{q}}^\dagger e_{\mathbf{k}'-\mathbf{q}}'^\dagger e_{\mathbf{k}'}' e_{\mathbf{k}} - e_{\mathbf{k}+\mathbf{q}}^\dagger h_{\mathbf{k}'-\mathbf{q}}^\dagger h_{\mathbf{k}'} e_{\mathbf{k}} - e_{\mathbf{k}+\mathbf{q}}'^\dagger h_{\mathbf{k}'-\mathbf{q}}^\dagger h_{\mathbf{k}'} e_{\mathbf{k}}' \right), \quad (5.1)$$

where the first line describes free electrons and holes, and the second line accounts for electron–electron and electron–hole interactions. Hole–hole interactions are disregarded as we consider a low density of negatively-charged trions. We now truncate the Fock space to the subspace of single trion states $|h_{\mathbf{k}_h} e_{\mathbf{k}_e} e_{\mathbf{k}_e}'\rangle$, providing an accurate description of the system in the case where all charges are bound into trions and the trion density is small. In order to gain microscopic access into the internal substructure of trion states and facilitate the numerics, we transform electron–electron–hole states into the exciton–electron picture (see Fig. 5.1a-b), that is

$$|h_{\mathbf{k}_h} e_{\mathbf{k}_e} e_{\mathbf{k}_e}'\rangle = \sum_{\nu} \phi_{\mathbf{k}_x}^{\nu} |X_{\nu\mathbf{Q}_x} e_{\mathbf{k}_e}'\rangle, \quad (5.2)$$

where \mathbf{k}_x and \mathbf{Q}_x are the relative and center-of-mass momentum coordinates of the exciton formed by the electron e and the hole. By applying this transformation, we get rid of a part of the problem—that is, the interaction between the electron e and the hole, which is now encoded in the exciton state ν . The expansion of exciton–electron states into the trion basis with

¹Trions with the two electrons in the same valley are usually unstable or exhibit a small binding energy [107].

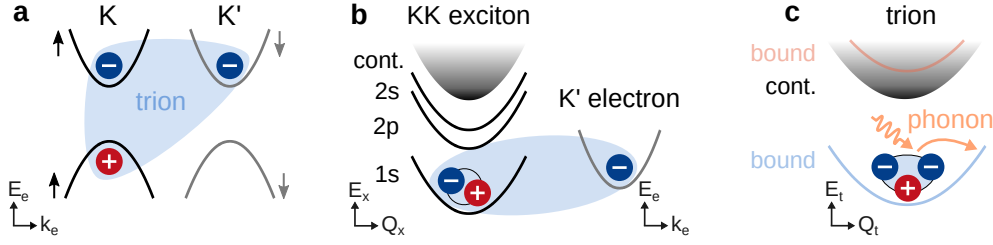


Figure 5.1: Trion configuration in the **a**: electron-hole and **b**: exciton-electron picture in monolayer MoSe₂. **c**: Trion states consisting of the ground (blue) and excited (red) bound states as well as the scattering continuum. A trion can scatter within its center-of-mass dispersion by absorbing or emitting a phonon (cf. orange arrow). Figure adapted from Ref. [108] (Pape V).

trion states $|T_{\lambda\mathbf{Q}}\rangle$ reads

$$|X_{\nu,\mathbf{Q}_x}e'_{\mathbf{k}_e}\rangle = \sum_{\lambda} \psi_{\nu,\beta_e\mathbf{Q}_x-\beta_x\mathbf{k}_e}^{\lambda} |T_{\lambda,\mathbf{Q}_x+\mathbf{k}_e}\rangle, \quad (5.3)$$

with $\beta_e = m_e/M_t$, $\beta_x = M_x/M_t$, $M_t = M_x + m_e$ is the trion's total mass, and m_e is the mass of the electron e' . The trion wave functions $\psi_{\nu,\mathbf{k}_t}^{\lambda}$ and eigenenergies ε_t^{λ} in this picture fulfill the exciton-electron Schrödinger equation,

$$\left(\varepsilon_x^{\nu} + \frac{\hbar^2\mathbf{k}_t^2}{2m_{x-e}}\right) \psi_{\nu,\mathbf{k}_t}^{\lambda} + \sum_{\mu\mathbf{q}} \tilde{V}_{\mathbf{q}}^{\nu\mu} \psi_{\mu,\mathbf{k}_t+\mathbf{q}}^{\lambda} = \varepsilon_t^{\lambda} \psi_{\nu,\mathbf{k}_t}^{\lambda}, \quad (5.4)$$

where $m_{x-e} = M_x m_e / M_t$ is the exciton-electron reduced mass. The exciton-electron interaction potential,

$$\begin{aligned} \tilde{V}_{\mathbf{q}}^{\nu\mu} &= V_{\mathbf{q}} \langle \nu | (e^{i\alpha_h\mathbf{q}\cdot\mathbf{r}} - e^{-i\alpha_e\mathbf{q}\cdot\mathbf{r}}) | \mu \rangle \\ &= V_{\mathbf{q}} \sum_{\mathbf{k}_x} \phi_{\mathbf{k}_x}^{\nu*} (\phi_{\mathbf{k}_x+\alpha_h\mathbf{q}}^{\mu} - \phi_{\mathbf{k}_x-\alpha_e\mathbf{q}}^{\mu}), \end{aligned} \quad (5.5)$$

is the sum of the electron-electron ($e-e'$) and electron-hole ($e'-h$) interaction terms weighted by the overlap between exciton wave functions $\phi_{\mathbf{k}_x}^{\nu}$. Importantly, this interaction leads to the mixing of different exciton states ν . In particular, the interaction is maximized for the coupling between s- and p-like exciton states and can be shown to resemble a classical dipole-charge interaction [109, 110]. The advantage of considering the full series of exciton states with finite angular momentum is that it provides a microscopic

description of the exciton–electron interaction [61, 109]. Other works have significantly simplified the problem by considering a short-range or contact interaction between 1s excitons and free electrons [73–75].

After mapping single-trion projectors into trion operators ($|T\rangle\langle T| \rightarrow T^\dagger T$) the obtained Hamiltonian describing the system of trions and phonons reads

$$H = \sum_{\lambda\mathbf{Q}} E_{\mathbf{Q}}^\lambda T_{\lambda\mathbf{Q}}^\dagger T_{\lambda\mathbf{Q}} + \sum_{\mathbf{q}} \hbar\Omega_{\mathbf{q}} b_{\mathbf{q}}^\dagger b_{\mathbf{q}} + \sum_{\mathbf{Q}\mathbf{q}\lambda\lambda'} G_{\mathbf{t},\mathbf{q}}^{\lambda\lambda'} T_{\lambda,\mathbf{Q}+\mathbf{q}}^\dagger T_{\lambda',\mathbf{Q}} (b_{\mathbf{q}} + b_{-\mathbf{q}}^\dagger). \quad (5.6)$$

Here, the first term describes free trions with energy $E_{\mathbf{Q}}^\lambda = \varepsilon_t^\lambda + \frac{\hbar^2 \mathbf{Q}^2}{2M_t}$ (cf. Fig. 5.1c) and corresponds to Eq. (5.1) after the Fock space truncation and transformation into trion basis. The trion operators $T_{\lambda\mathbf{Q}}^{(\dagger)}$ fulfill fermionic anti-commutation relations at low trion densities. The second and third terms describe free phonons and the trion–phonon interaction, respectively. The trion–phonon matrix element $G_{\mathbf{t},\mathbf{q}}^{\lambda\lambda'}$ contains electron–phonon coupling strengths weighted by wave function overlaps between the initial and final trion states, λ and λ' . With this effective trion Hamiltonian, one can derive equations of motion for the trion occupation through the standard methods involving the cluster expansion and Markov approximation, gaining access to the trion dynamics. Details on the derivation of the Hamiltonian and the exact form of $G_{\mathbf{t},\mathbf{q}}^{\lambda\lambda'}$ can be found in the appendices of Paper V.

Trion states in the exciton-electron picture

We consider hBN-encapsulated monolayer MoSe₂ as exemplary material for our study. In this material, the trion state with lowest energy is formed by electrons and holes at the K and K' valleys (cf. Fig. 5.1a) and is optically bright. Before studying the trion–phonon interaction, we want to understand the quantum structure of trions. For that purpose, we solve Eq. (5.4) and obtain the series of trion eigenstates (Fig. 5.2a). We obtain a bound trion state 17 meV below the 1s exciton energy, in agreement with previous theoretical works [61, 111]. In Paper V, we find that the electron-hole pair forming this state has mostly 1s exciton character but also a significant contribution from the 2p state. The mixing between 1s and 2p exciton states describes the polarization of the exciton due to the potential generated by the additional electron.

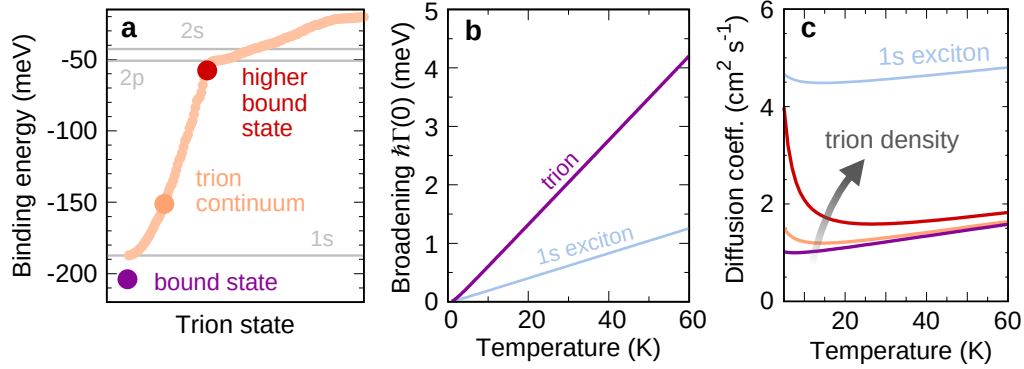


Figure 5.2: **a**: Trion eigenstates in hBN-encapsulated MoSe₂. The ground (higher) bound state is marked by a purple (red) dot, and the exciton–electron scattering states are denoted in orange. The 1s, 2p, and 2s exciton binding energies are shown as a reference. **b**: Temperature-dependent phonon-induced spectral broadening of the ground trion and exciton states. **c**: Temperature dependence of the trion diffusion coefficient in the low-density limit (purple) and for trion densities of $1 \times 10^{11} \text{ cm}^{-2}$ (orange) and $4 \times 10^{11} \text{ cm}^{-2}$ (red). The low-density exciton diffusion coefficient is shown in light-blue. Figure adapted from Ref. [108].

The 1s exciton energy corresponds to the onset of the trion continuum. In general, the trion continuum is composed of exciton–electron scattering states, where the exciton and the electron are not bound. However, we identify a bound state (through its wave function shape and excitonic composition) within the continuum, 16 meV below the 2s exciton state. This excited trion state has been observed in optical spectra [112–115] and has previously been theoretically predicted [61, 110]. Resolving the whole series of trion states shows promise for modeling the trion dynamics across a wide range of energies and states.

Trion-phonon scattering

While we have computed the whole series of trion states, and our model principally allows us to evaluate the trion dynamics considering all states, we restrict our study to the ground trion state. At low temperatures, almost all the trion population resides in this state and transitions into excited states via

phonon absorption are negligible. Considering the trion Hamiltonian (5.6) and using the standard Heisenberg equation and cluster expansion method, we find the equation of motion for the trion occupation. In the resulting equation, one can identify the out-scattering rate, which considering low occupation reads

$$\Gamma_{\mathbf{Q}} = \frac{2\pi}{\hbar} \sum_{\mathbf{q}\pm} |G_{\mathbf{t},\mathbf{q}}|^2 \eta_{\mathbf{q}}^{\pm} \delta(E_{\mathbf{Q}-\mathbf{q}} - E_{\nu\mathbf{Q}} \pm \hbar\Omega_{\mathbf{q}}). \quad (5.7)$$

In Paper V, we calculate the trion-phonon coupling $G_{\mathbf{t},\mathbf{q}}$ and the momentum-dependent scattering rate $\Gamma_{\mathbf{Q}}$. Here, we focus on the scattering rate at the bottom of the trion dispersion, $\Gamma_{\mathbf{0}}$, which results in the spectral broadening of this state (Fig. 5.2b). In particular, we find that trion-phonon scattering is 3-4 times stronger than exciton-phonon scattering. This is mainly a result of the larger mass of trions compared to excitons, resulting in a larger density of states. In addition, the phonon coupling element is stronger for trions due to the additional electron.

Furthermore, we benchmark our model by computing the trion cooling time following Ref. [116]. In short, the cooling time τ_c is determined by the rate at which the excess trion heat dissipates into the lattice, that is $Q = \tau_c^{-1} n_{\mathbf{t}} (T - T_L)$, where $Q = A^{-1} \sum_{\mathbf{q}} \hbar\Omega_{\mathbf{q}} \dot{n}_{\mathbf{q}}$ is the cooling power or heat dissipation rate, $n_{\mathbf{t}}$ is the trion density, T (T_L) the trion (lattice) temperature, and $n_{\mathbf{q}}$ is the phonon number. The good agreement between our theoretical prediction (4-10 ps for temperatures up to 50 K) and experimental measurements (5-15 ps) supports the predictive character of our microscopic theory.

Trion transport and Fermi pressure effect

The computed trion-phonon scattering rates are a key ingredient to calculate the diffusion coefficient and mobility of trions. These quantities can be evaluated following the work of Hess and Kuhn [100] and are determined by the scattering rates, trion mass, and trion occupation. In general, we predict trion transport to be slow compared to that of excitons and free electrons (cf. Fig. 5.2c). This is a direct consequence of the large mass (i.e. low velocity) of trions and the efficient trion-phonon scattering hindering propagation. We also observe a subtle increase of the diffusion coefficient as temperature is

raised, resulting from the less efficient scattering at higher kinetic energies (see Paper V for details). In particular, we predict a low-temperature diffusion coefficient of $1 \text{ cm}^2/\text{s}$ for trions compared to $4.5 \text{ cm}^2/\text{s}$ for excitons. The calculated value for excitons is within the error bars of experimentally determined diffusion coefficients [117]. The trion diffusion coefficient reported in experiments at similar conditions [118] is, however, 4-5 times larger than our prediction. This discrepancy could be related to non-equilibrium effects present in the experiment or, as we show in the following, due to the fermionic enhancement of diffusion.

The fermionic nature of trions has a significant impact on trion diffusion. At low temperatures the trion gas becomes degenerate, i.e. states with low kinetic energy are full, forcing the occupation of higher states. Since the velocity of these higher states is larger, the overall diffusion of the trion gas is enhanced (cf. Fig. 5.2c). This effect can also be understood as a build-up of a large pressure by the degenerate trion gas². In particular, at temperatures approaching the absolute zero ($T \rightarrow 0 \text{ K}$) the degenerate gas exerts a finite pressure $P = n_t E_F/2$, as opposed to a classical gas with $P = n_t k_B T \rightarrow 0$. Here we introduced the trion density n_t and the Fermi level E_F . The current $\mathbf{j} = -(\tau/M)\nabla P$ (with τ being the thermalization time) is then driven by the large pressure gradient in the degenerate gas. One can further show that the diffusion is characterized by the diffusion coefficient $D = (\tau/M)E_F$, clearly increasing with the Fermi level as opposed to the classical expression $D = (\tau/M)k_B T$. In Paper V, we thus predict the fermionic enhancement of trion diffusion, which still remains to be experimentally verified.³

5.2 Trion photoluminescence

The electron-hole pair within a trion can recombine, emitting a photon and leaving behind the additional electron which then becomes free. The energy

²An interesting analogy can be found in neutron stars, where the degenerate fermion gas exerts a large outwards pressure, stabilizing the star against gravitational collapse.

³The fermionic enhancement of diffusion has otherwise been observed for holes in strongly excited $\text{MoSe}_2/\text{WSe}_2$ van der Waals heterostructures in Paper XXVIII, where we supported the experimental observations with microscopic simulations of spatiotemporal dynamics including Pauli blocking and hole-hole repulsion.

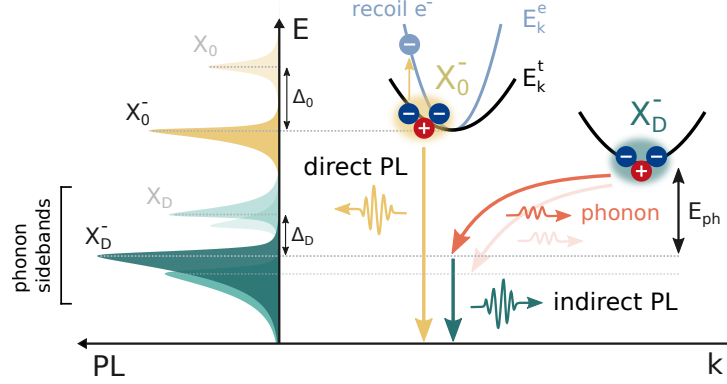


Figure 5.3: Illustration of direct and phonon-assisted trion recombination mechanisms. A bright trion (left, X_0^-) can directly recombine by emitting a photon and leaving a recoil electron behind. A dark trion (right, X_D^-) can recombine by scattering with a phonon into a virtual bright state and then emit a photon, leaving a recoil electron behind. The PL spectrum resulting from the recombination of excitons (X_0 , X_D) and trions is sketched on the left. Figure adapted from Paper VI.

conservation of this process dictates that the sum of the photon and electron energies is equal to the trion energy, i.e. $\hbar\omega + E_e = E_t$. Considering the trion as a bound exciton–electron complex with energy $E_t = E_x + E_e - \Delta$, the energy conservation of the process reads $\hbar\omega = E_x - \Delta$, where Δ is the trion binding energy or, in other words, the energy needed to remove the additional (non-recombining) electron from the trion. The trion PL peak therefore appears below the exciton peak separated by the trion binding energy Δ (cf. Fig. 5.3) [27, 28].⁴ The additional electron can acquire the whole momentum of the trion, implying that trions with any momentum can recombine (as opposed to excitons which need zero center-of-mass momentum), cf. Fig. 5.3. This effect is known as electron recoil and gives rise to a characteristic low-energy tail in the PL peak that reflects the temperature of the trion gas [119, 120].

The direct recombination of a trion is generally only allowed when the recombining electron and hole are located in the same valley and occupy bands with the same spin.⁵ Otherwise, trions can still recombine by first scattering

⁴This holds at low doping and photoexcitation densities. The separation between exciton and trion peaks in PL increases with doping due to polaronic effects [73–76].

⁵Spin-conserving optical transitions couple to light propagating in the out-of-plane

into a virtual bright state with a phonon providing the necessary momentum or spin (cf. Fig. 5.3), in analogy to the phonon-assisted recombination of dark excitons [83]. The energetic position of the resulting phonon sidebands in PL spectra, $\hbar\omega = E_x - \Delta + \hbar\Omega$, can be traced back to the energy $\hbar\Omega$ of the different phonon modes involved [121]. Moreover, the shift of the PL resonances under magnetic field is related to the spin and valley of the recombining electron and hole and can therefore be used to identify the spin-valley configuration of the trion [122]. Despite the relatively good understanding of the trion PL signatures, a microscopic model consistently describing the peak positions, lineshape, and intensity of bright and dark trions in n- and p-doped samples has been missing so far.

In Paper VI, we bridge this gap by developing a microscopic theory of trion recombination. We apply our model to WSe₂ and compute the trion energy landscape in this material. Furthermore, we provide insights into the impact of mass imbalance between equal charges within the trion on the stability and PL resonance of trions. Finally, we compute the PL spectra and predict intriguing signatures of trions with an electron located at the Λ point.

Trion landscape in WSe₂ and impact of mass imbalance

The multi-valley band structure of WSe₂ hosts dark trions (X_D^-) as the most energetically favourable species [123–125] (cf. Fig. 5.4a). While X_D^- contains two electrons with equal effective mass at the $K\downarrow$ and $K'\uparrow$ bands, bright trions $X_{K(\Lambda)}^-$ contain two electrons with different mass at the $K\uparrow$ and $K\downarrow$ ($\Lambda\uparrow$) bands. In the following, we describe how the eigenenergies of trion states with such mass imbalance can be computed.

We obtain the trion eigenenergies ε_ν and wave functions $\Psi_\nu(\mathbf{r}_1, \mathbf{r}_2)$ for each spin-valley configuration $\nu = \{\nu_h, \nu_{e1}, \nu_{e2}\}$ from a variational solution of the Schrödinger equation, $\mathcal{H}_\nu \Psi_\nu(\mathbf{r}_1, \mathbf{r}_2) = \varepsilon_\nu \Psi_\nu(\mathbf{r}_1, \mathbf{r}_2)$. Here,

$$\mathcal{H}_\nu = -\frac{\hbar^2 \nabla_{\mathbf{r}_1}^2}{2\mu_1} - \frac{\hbar^2 \nabla_{\mathbf{r}_2}^2}{2\mu_2} - \frac{\hbar^2 \nabla_{\mathbf{r}_1} \cdot \nabla_{\mathbf{r}_2}}{m_h} + V(\mathbf{r}_1 - \mathbf{r}_2) - V(\mathbf{r}_1) - V(\mathbf{r}_2) \quad (5.8)$$

direction. Spin-flip transitions are not completely forbidden but exhibit weak oscillator strengths and couple to light traveling in the direction of the material's plane [80].

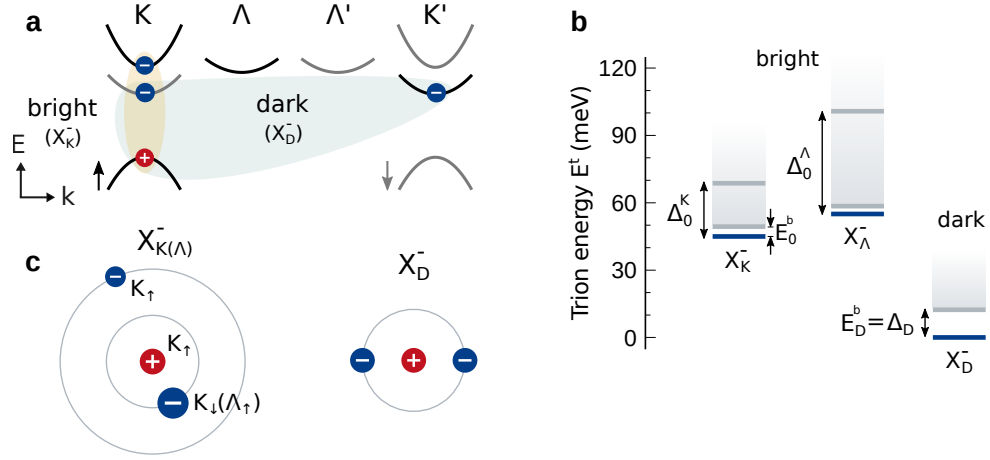


Figure 5.4: **a:** Spin–valley configuration of bright (X_K^-) and dark (X_D^-) trions in the band structure of WSe₂. **b:** Trion energies (blue lines) with respect to the lowest trion state. Exciton states are denoted by grey lines, and the exciton–electron continuum is represented by the grey shaded area. Trion binding energies are denoted by $E_{0(D)}^b$, and the energy difference with the bright exciton is denoted by $\Delta_0^{K(\Lambda)}$. **c:** Illustration of the Bohr radii of electrons within the trion in the case of $X_{K(\Lambda)}^-$ (mass imbalance) and X_D^- (mass balance). Figure adapted from Paper VI.

is the Hamiltonian for an electron–electron–hole complex [126], with the relative electron–hole mass $\mu_{1(2)}^{-1} = m_h^{-1} + m_{e1(2)}^{-1}$. The energy ε_ν is minimized considering the ansatz

$$\Psi_\nu(\mathbf{r}_1, \mathbf{r}_2) = \mathcal{N} \left(e^{-|\mathbf{r}_1|/a_1} e^{-|\mathbf{r}_2|/a_2} + C e^{-|\mathbf{r}_1|/b_1} e^{-|\mathbf{r}_2|/b_2} \right), \quad (5.9)$$

with $\mathbf{r}_{1(2)}$ being the relative electron–hole coordinate for the electron in the spin–valley state $\nu_{e1(2)}$. We also introduced the variational parameters a_1 , a_2 , b_1 , b_2 , C and the normalization factor \mathcal{N} . Note that $\Psi_\nu(\mathbf{r}_1, \mathbf{r}_2)$ is formally an envelope function and therefore does not need to fulfill fermionic anti-symmetry [110]. The ansatz for $\Psi_\nu(\mathbf{r}_1, \mathbf{r}_2)$ introduced here is similar to the symmetrized product of hydrogenic wave functions [126, 127] but allows for a mass imbalance between the two equal charges within a trion by introducing the weight factor C and by removing the restriction $b_1 = a_2, b_2 = a_1$.

In Fig. 5.4b we show the most relevant trion states in n-type WSe₂, together with the respective exciton energies. Our model correctly predicts that dark trions (X_D^-) are the energetically favourable species, with a binding energy

of 12 meV in good agreement with experiments [124, 125]. The higher-lying bright trions (X_K^- , X_A^-) exhibit a suppressed binding energy (E_0^b). This phenomenon can be understood as follows. The mass imbalance between electrons results in the preferential binding of the hole with the heavy electron due to its low kinetic energy. As the heavy electron becomes more tightly bound with the hole, the lighter electron is pushed away due to the repulsive electron–electron interaction (cf. Fig. 5.4c). The lighter electron then sees the heavy-electron-hole pair as a neutral cloud with which it interacts and binds weakly. Therefore, trions become less stable when there is a mass imbalance between the two equal charges. This intuitive explanation is supported by the calculations of Bohr radii and average interaction energies in Paper VI.

Besides reducing the trion stability, the mass imbalance between equal charges can have an intriguing consequence in PL spectra. As we explained above, the trion PL peak appears below the exciton resonance separated by the trion binding energy. In the case of mass imbalance, however, one must be more specific. The exciton–trion separation in PL is determined by the energy needed to remove the non-recombining or recoil electron from the trion (Δ in Fig. 5.4b). In the case of bright trions in WSe_2 , the non-recombining electron is heavier than the recombining one, and therefore it is more tightly bound with the hole. The energy needed to extract the heavy electron is hence larger than the actual trion binding energy (compare Δ_0^K and E_0^b in Fig. 5.4b) and significantly increases when the mass imbalance is accentuated (observe that $\Delta_0^A > \Delta_0^K$). We thus predict that the exciton–trion separation in PL is larger for bright trions than for dark ones due to the mass imbalance. Furthermore, despite having a higher three-body energy, X_A^- will appear in PL spectra below X_K^- .

Photoluminescence spectra of trions in WSe_2

The trion energy landscape in WSe_2 suggests the presence of interesting features in PL, such as the difference in exciton–trion energy separation for the bright and dark states due to mass imbalance. In order to provide a description of these PL signatures, we develop a microscopic model for the radiative recombination of trions, including phonon-assisted recombination

of dark trions. Here, we outline the main steps, while the detailed derivation can be found in the supplementary information of Paper VI.

We make use of the Fock space truncation scheme, considering the subspaces of single-trion and single-electron states. These states describe the initial and final states of the recombination process where an electron-hole pair within the trion recombines, leaving behind an electron. Making use of the Fock space truncation scheme, we obtain the following Hamiltonian describing the system of trions, electrons, photons, and phonons, $H = H_0 + H_{\text{t-phot}} + H_{\text{t-phon}}$, with

$$H_0 = \sum_{\nu\mathbf{Q}} E_{\nu\mathbf{Q}}^{\text{t}} T_{\nu\mathbf{Q}}^{\dagger} T_{\nu\mathbf{Q}} + \sum_{\nu_e\mathbf{k}_e} E_{\nu_e\mathbf{k}_e}^{\text{e}} e_{\nu_e\mathbf{k}_e}^{\dagger} e_{\nu_e\mathbf{k}_e} + \sum_{\kappa} \hbar\omega_{\kappa} c_{\kappa}^{\dagger} c_{\kappa} + \sum_{\mathbf{q}} \hbar\Omega_{\mathbf{q}} b_{\mathbf{q}}^{\dagger} b_{\mathbf{q}}, \quad (5.10)$$

$$H_{\text{t-phot}} = \sum_{\nu\nu_e\mathbf{k}\kappa} \tilde{\mathcal{M}}_{\mathbf{k}\kappa}^{\nu\nu_e} e_{\nu_e\mathbf{k}}^{\dagger} T_{\nu\mathbf{k}+\kappa_{\parallel}} c_{\kappa}^{\dagger} + \text{H.c.}, \quad (5.11)$$

$$H_{\text{t-phon}} = \sum_{\nu\nu'\mathbf{Q}\mathbf{q}} G_{\text{t},\mathbf{q}}^{\nu\nu'} T_{\nu'\mathbf{Q}+\mathbf{q}}^{\dagger} T_{\nu\mathbf{Q}} (b_{\mathbf{q}} + b_{-\mathbf{q}}^{\dagger}). \quad (5.12)$$

Here, H_0 accounts for free trions, electrons, phonons, and photons. The second term, $H_{\text{t-phot}}$, describes the recombination of a trion with the emission of a photon and the creation of a free electron, as well as the Hermitian conjugate of this process. The trion-photon matrix element $\tilde{\mathcal{M}}_{\mathbf{k}\kappa}^{\nu\nu_e}$ is determined by the wave function overlap between the non-recombining electron within the trion and a plane wave describing the free electron. The trion-photon matrix element also contains the optical selection rules $\delta_{\nu_{\text{h}},\nu_{\text{e1}}}\delta_{\nu_e,\nu_{\text{e2}}}$ or $\delta_{\nu_{\text{h}},\nu_{\text{e2}}}\delta_{\nu_e,\nu_{\text{e1}}}$ enforcing that the recombining electron and hole are located in the same valley and identifying the remaining charge as the recoil electron. The last term, $H_{\text{t-phon}}$, describes the trion-phonon interaction with the matrix element $G_{\text{t},\mathbf{q}}^{\nu\nu'}$. The exact form of the matrix elements can be found in the supplementary information of Paper VI. Note that the interaction between free electrons and phonons has been disregarded as it only has a negligible impact on the spectral broadening.

The PL intensity is determined by the photon emission rate via the relation $I_{\text{PL}}(\omega) = \sum_{\kappa} \delta(\omega - \omega_{\kappa}) \dot{n}_{\kappa}$, where $n_{\kappa} = \langle c_{\kappa}^{\dagger} c_{\kappa} \rangle$ is the photon number. Therefore, we need to find the equation of motion for n_{κ} . Similar to the case of

excitons [83], we apply the cluster expansion scheme and truncate to account for processes involving a single phonon and a single photon, while considering higher-order correlations via the renormalization and spectral broadening of trion energies. The intermediate steps can be found in Paper VI, while here we directly provide the resulting PL formula,

$$I_{\text{PL}}(\omega) = \frac{2}{\hbar} \sum_{\nu\nu_e\mathbf{k}} \frac{|\tilde{\mathcal{M}}_{\mathbf{k}}^{\nu\nu_e}|^2}{(E_{\nu\mathbf{k}}^t - E_{\nu_e\mathbf{k}}^e - \hbar\omega)^2 + (\gamma_{\nu\mathbf{k}}^t)^2} \times \left[N_{\nu\mathbf{k}} \gamma_{\nu\mathbf{k}}^{\text{t-phot}} + \sum_{\nu'j\mathbf{q}\pm} \frac{N_{\nu'\mathbf{k}+\mathbf{q}} |G_{t,\mathbf{q}}^{\nu'\nu}|^2 \eta_{j\mathbf{q}}^{\pm} \gamma_{\nu'\mathbf{k}+\mathbf{q}}^t}{(E_{\nu'\mathbf{k}+\mathbf{q}}^t - E_{\nu_e\mathbf{k}}^e - \hbar\omega \mp \hbar\Omega_{j\mathbf{q}})^2 + (\gamma_{\nu'\mathbf{k}+\mathbf{q}}^t)^2} \right]. \quad (5.13)$$

The first term in this equation describes the direct recombination of a trion with energy $E_{\nu\mathbf{k}}^t$ via the emission of a photon with energy $\hbar\omega$ and the recoil of an electron into the free-electron state with energy $E_{\nu_e\mathbf{k}}^e$. The spectral resonance is broadened by the dephasing $\gamma_{\nu\mathbf{k}}^t = \gamma_{\nu\mathbf{k}}^{\text{t-phot}} + \gamma_{\nu\mathbf{k}}^{\text{t-phon}}$ arising from trion–photon and trion–phonon interactions, respectively. The second term in the brackets describes the recombination of a trion in the state ν' via the scattering with a phonon with mode j , momentum \mathbf{q} , and energy $\hbar\Omega_{j\mathbf{q}}$ into the virtual bright state ν (cf. Fig. 5.3). The trion in the virtual bright state recombines by emitting a photon, leaving a recoil electron behind. The resulting PL peak appears offset from the dark trion resonance by the energy of the phonon involved. The PL intensity is governed by the product of trion occupation $N_{\nu\mathbf{k}} = \langle T_{\nu\mathbf{Q}}^\dagger T_{\nu\mathbf{Q}} \rangle$ and transition matrix elements. In order to simplify the calculations while describing a realistic scenario, we consider that the trion gas is in thermal equilibrium with the lattice and is therefore well described by a Boltzmann distribution in the considered low-density regime. Moreover, we only consider recombination of bound trions since the oscillator strength of the exciton–electron continuum becomes suppressed with doping [73, 75].

In Fig. 5.5 we show the computed trion PL spectra for n- and p-type WSe₂ as a function of temperature. At low temperatures, most of the trion population resides in the dark state, leading to PL spectra dominated by phonon sidebands appearing below the dark trion resonance (X_D^\pm). Both p- and n-type dark trions have a similar spin–valley composition and binding energy, resulting in similar PL spectra. As the temperature is raised, higher-lying dark states are occupied, giving rise to signatures that are distinct for p- and

n-type doping (more details in Paper VI). Further increasing the temperature leads to the occupation of bright trions that then dominate the PL. Here, the impact of mass imbalance is crucial. On the one hand, p-type bright trions (X_0^+) exhibit mass balance and a binding energy of 12 meV, corresponding to the energetic offset with respect to the bright exciton in PL (cf. Δ_0 in Fig. 5.5a). On the other hand, n-type bright trions exhibit a significant large imbalance, resulting in the large energetic offset for X_K^- and X_Λ^- . Importantly, the higher three-body energy of X_Λ^- compared to X_K^- implies that it becomes populated and produces a visible PL signal at higher temperatures. Interestingly, however, the large mass of the Λ electron results in a larger offset (compare Δ_0^Λ with Δ_0^K in Fig. 5.5b), implying that the PL signal of X_Λ^- appears below that of X_K^- .

Our results agree well with experimental observations. In particular, we quantitatively reproduce the binding energy of dark trions, and qualitatively describe the larger exciton–trion PL offset for bright n-type trions compared to p-type ones⁶. However, the predicted signatures from X_Λ^- and other trion states with Λ electrons have not been observed in experiments so far. The presence of non-equilibrium distributions or the uncertainty in the energetic offset between K and Λ valleys could explain this discrepancy. Nevertheless, we expect that Λ -point trions play an important role in the thermalization dynamics, similar to Λ excitons [87] (as we have seen in Paper III), and could therefore be observed in time-resolved PL experiments (as excitons in Paper XI). Furthermore, strain engineering of the K- Λ energetic offset [128] should shed light on the role of the Λ valley on the trion landscape and dynamics. We expect that the gained microscopic insights will trigger further experimental and theoretical studies addressing the impact of the Λ valley on the physics of charge complexes in atomically thin semiconductors.

⁶A better quantitative agreement is expected when considering the exchange interaction that leads to the splitting of degenerate trion states [45].

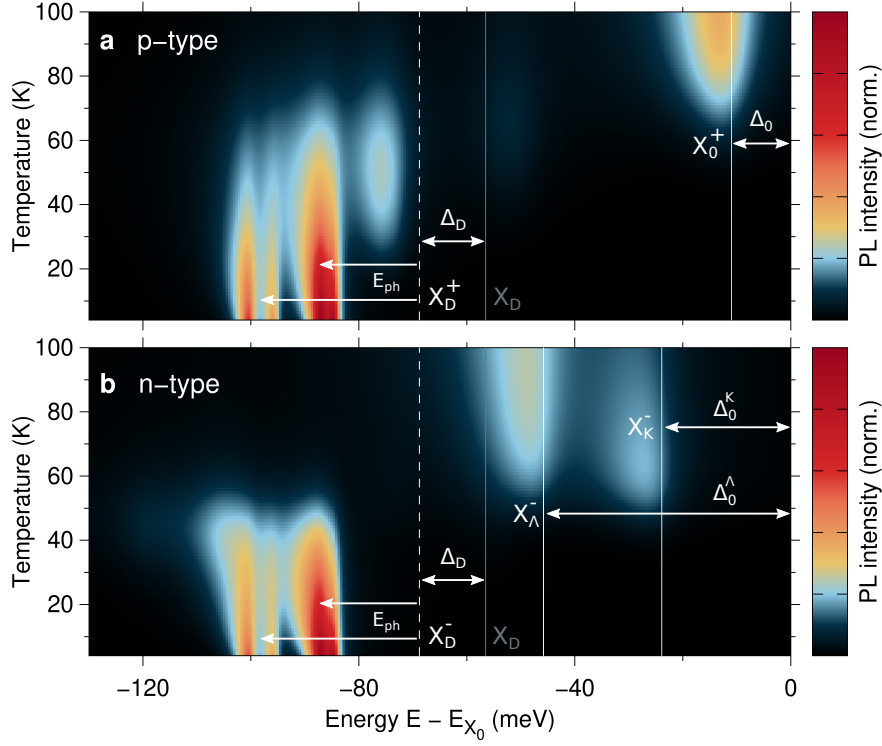


Figure 5.5: Temperature-dependent PL spectra in **a**: p- and **b**: n-type WSe₂, exhibiting bright (X_0^\pm , solid white lines) and dark (X_D^\pm , dashed white lines) trion resonances. The spectra have been normalized to the integrated PL for each temperature. The origin is offset to the bright exciton resonance (X_0), while the grey line denotes the dark exciton resonance (X_D). The separation between trion and exciton resonances is denoted by Δ . Furthermore, the phonon energy E_{ph} determines the position of the phonon sidebands associated with dark trions. Figure adapted from Paper VI.

CHAPTER 6

Conclusion and outlook

In this thesis, we have provided a microscopic understanding of fundamental many-particle phenomena that govern the optics, dynamics, and transport in atomically-thin materials, with particular focus on TMDs. The theoretical approach presented here describes a system of interacting electrons, holes, phonons, and photons, where electrons and holes can be bound into charge complexes such as excitons and trions. In particular, our work provides relevant insights on the formation, thermalization, propagation, and recombination of excitons and trions in TMDs. We have unravelled the formation dynamics of dark excitons after photoexcitation and resolved the main pathways of phonon-assisted exciton dissociation. Furthermore, we have traced the emergence of photoluminescence halos back to the significant heating and thermal drift of excitons at strong excitation. Finally, we have investigated the trion dynamics in doped materials, focusing on trion diffusion and photoluminescence. Importantly, we have predicted so-far unobserved luminescence signatures that could shed light on the internal structure of trions. The microscopic description of these processes represents a step forward in the understanding of the physics of charge complexes and contributes to

determining the optimal operation conditions, limitations and tunability of TMD-based devices.

The recent progress in the study of charge complexes in atomically-thin materials has opened up new questions and challenges. In particular, the coexistence of different charge complexes at arbitrary photoexcitation densities and doping could have important implications that have started to be addressed only recently, such as interaction-driven energy shifts, activation of additional scattering channels [120, 129], and modification of the overall diffusion properties of electron-hole pairs [130]¹. In principle, the theoretical framework presented here can be applied to describe coexisting complexes by extending the Fock space truncation scheme.

Moreover, while in this thesis we have focused on monolayers, a lot of the current research efforts are directed towards van der Waals heterostructures. These structures host charge complexes consisting of a superposition of intra- and interlayer states (i.e. spatially separated charges residing in different layers) that can be tuned by an electric field [131–136]. Additionally, the moiré potential emerging in these materials offers a periodic potential landscape that can trap [137] and even separate charges [138]. The periodic localization of interacting quasiparticles constitutes an experimental realization of a Hubbard model of fermions (electrons) and/or bosons (excitons), and could give rise to exotic phases of matter [18, 134, 139–143]. The microscopic description of single excitons and trions provided in this work serves as a starting point to describe layer-hybridized charge complexes in a moiré lattice. The extension towards interacting charge complexes should contribute to the understanding of Hubbard physics in Fermi–Bose mixtures.

¹See also Paper X, where the presence of free electrons and holes due to entropy ionization enhances the diffusion at low densities.

Acknowledgments

First of all, I would like to thank my supervisor, Ermin Malic, for his constant support, motivation, and guidance. I would also like to thank Samuel Brem for his important insights and stimulating discussions.

I further thank my examiner, Jari Kinaret, for carefully reading my thesis and for his kind career advice. I am very grateful to my opponent (Atac Imamoglu) and the members of the grading committee (Thorsten Deilmann, Doris Reiter, Janine Splettstoesser, and Mats Granath) for taking their valuable time to read my thesis and participate in my defense. I would also like to thank the Excellence Initiative (now Area of Advance) Nano at Chalmers for funding my PhD position within the Excellence PhD program.

Moreover, I thank all the members of the Ultrafast Quantum Dynamics group in Marburg and Chalmers, especially Daniel and Joakim for the daily conversations during coffee and lunch breaks.

Finally, the people that give me strength during the good and bad days are my family, friends and, most of all, Gemma. Gràcies per tot!

Bibliography

- [1] Kostya S Novoselov, Andre K Geim, Sergei V Morozov, De-eng Jiang, Yanshui Zhang, Sergey V Dubonos, Irina V Grigorieva, and Alexandr A Firsov. Electric field effect in atomically thin carbon films. *Science*, 306(5696):666–669, 2004.
- [2] Kostya S Novoselov, D Jiang, F Schedin, TJ Booth, VV Khotkevich, SV Morozov, and Andre K Geim. Two-dimensional atomic crystals. *Proceedings of the National Academy of Sciences*, 102(30):10451–10453, 2005.
- [3] Kin Fai Mak, Changgu Lee, James Hone, Jie Shan, and Tony F Heinz. Atomically thin MoS₂: a new direct-gap semiconductor. *Physical Review Letters*, 105(13):136805, 2010.
- [4] Andrea Splendiani, Liang Sun, Yuanbo Zhang, Tianshu Li, Jonghwan Kim, Chi-Yung Chim, Giulia Galli, and Feng Wang. Emerging photoluminescence in monolayer MoS₂. *Nano Letters*, 10(4):1271–1275, 2010.
- [5] Qing Hua Wang, Kouros Kalantar-Zadeh, Andras Kis, Jonathan N Coleman, and Michael S Strano. Electronics and optoelectronics of two-

- dimensional transition metal dichalcogenides. *Nature Nanotechnology*, 7(11):699–712, 2012.
- [6] Andre K Geim and Irina V Grigorieva. Van der Waals heterostructures. *Nature*, 499(7459):419–425, 2013.
 - [7] Xiaofeng Qian, Junwei Liu, Liang Fu, and Ju Li. Quantum spin Hall effect in two-dimensional transition metal dichalcogenides. *Science*, 346(6215):1344–1347, 2014.
 - [8] K S Novoselov, A Mishchenko, A Carvalho, and AH Castro Neto. 2D materials and van der Waals heterostructures. *Science*, 353(6298):aac9439, 2016.
 - [9] Branimir Radisavljevic, Aleksandra Radenovic, Jacopo Brivio, Valentina Giacometti, and Andras Kis. Single-layer MoS₂ transistors. *Nature Nanotechnology*, 6(3):147–150, 2011.
 - [10] Oriol Lopez-Sanchez, Dominik Lembke, Metin Kayci, Aleksandra Radenovic, and Andras Kis. Ultrasensitive photodetectors based on monolayer MoS₂. *Nature Nanotechnology*, 8(7):497–501, 2013.
 - [11] Kin Fai Mak and Jie Shan. Photonics and optoelectronics of 2D semiconductor transition metal dichalcogenides. *Nature Photonics*, 10(4):216–226, 2016.
 - [12] Thomas Mueller and Ermin Malic. Exciton physics and device application of two-dimensional transition metal dichalcogenide semiconductors. *npj 2D Materials and Applications*, 2(1):1–12, 2018.
 - [13] Gang Wang, Alexey Chernikov, Mikhail M Glazov, Tony F Heinz, Xavier Marie, Thierry Amand, and Bernhard Urbaszek. Colloquium: Excitons in atomically thin transition metal dichalcogenides. *Reviews of Modern Physics*, 90(2):021001, 2018.
 - [14] Alexey Chernikov, Timothy C Berkelbach, Heather M Hill, Albert Rigosi, Yilei Li, Ozgur Burak Aslan, David R Reichman, Mark S Hybertsen, and Tony F Heinz. Exciton binding energy and nonhydrogenic Rydberg series in monolayer WS₂. *Physical Review Letters*, 113(7):076802, 2014.

- [15] Keliang He, Nardeep Kumar, Liang Zhao, Zefang Wang, Kin Fai Mak, Hui Zhao, and Jie Shan. Tightly bound excitons in monolayer WSe₂. *Physical Review Letters*, 113(2):026803, 2014.
- [16] Raul Perea-Causin, Daniel Erkensten, Jamie M Fitzgerald, Joshua JP Thompson, Roberto Rosati, Samuel Brem, and Ermin Malic. Exciton optics, dynamics, and transport in atomically thin semiconductors. *APL Materials*, 10(10):100701, 2022.
- [17] Yilei Li, Alexey Chernikov, Xian Zhang, Albert Rigosi, Heather M Hill, Arend M Van Der Zande, Daniel A Chenet, En-Min Shih, James Hone, and Tony F Heinz. Measurement of the optical dielectric function of monolayer transition-metal dichalcogenides: MoS₂, MoSe₂, WS₂, and WSe₂. *Physical Review B*, 90(20):205422, 2014.
- [18] Emma C Regan, Danqing Wang, Eunice Y Paik, Yongxin Zeng, Long Zhang, Jihang Zhu, Allan H MacDonald, Hui Deng, and Feng Wang. Emerging exciton physics in transition metal dichalcogenide heterobilayers. *Nature Reviews Materials*, 7(10):778–795, 2022.
- [19] Sangwan Sim, Jusang Park, Jeong-Gyu Song, Chihun In, Yun-Shik Lee, Hyungjun Kim, and Hyunyong Choi. Exciton dynamics in atomically thin MoS₂: interexcitonic interaction and broadening kinetics. *Physical Review B*, 88(7):075434, 2013.
- [20] Galan Moody, Chandriker Kavir Dass, Kai Hao, Chang-Hsiao Chen, Lain-Jong Li, Akshay Singh, Kha Tran, Genevieve Clark, Xiaodong Xu, Gunnar Berghäuser, Ermin Malic, Andreas Knorr, and Xiaoqin Li. Intrinsic homogeneous linewidth and broadening mechanisms of excitons in monolayer transition metal dichalcogenides. *Nature Communications*, 6(1):8315, 2015.
- [21] Florian Katsch, Malte Selig, and Andreas Knorr. Exciton-scattering-induced dephasing in two-dimensional semiconductors. *Physical Review Letters*, 124(25):257402, 2020.
- [22] Daniel Erkensten, Samuel Brem, and Ermin Malic. Exciton-exciton interaction in transition metal dichalcogenide monolayers and van der Waals heterostructures. *Physical Review B*, 103(4):045426, 2021.

- [23] Yumeng You, Xiao-Xiao Zhang, Timothy C Berkelbach, Mark S Hybertsen, David R Reichman, and Tony F Heinz. Observation of biexcitons in monolayer WSe₂. *Nature Physics*, 11(6):477–481, 2015.
- [24] Kai Hao, Judith F Specht, Philipp Nagler, Lixiang Xu, Kha Tran, Akshay Singh, Chandriker Kavir Dass, Christian Schüller, Tobias Korn, Marten Richter, Andreas Knorr, Xiaoqin Li, and Galan Moody. Neutral and charged inter-valley biexcitons in monolayer MoSe₂. *Nature Communications*, 8(1):15552, 2017.
- [25] Matteo Barbone, Alejandro R-P Montblanch, Dhiren M Kara, Carmen Palacios-Berraquero, Alisson R Cadore, Domenico De Fazio, Benjamin Pingault, Elaheh Mostaani, Han Li, Bin Chen, Kenji Watanabe, Takashi Taniguchi, Sefaattin Tongay, Gang Wang, Andrea C. Ferrari, and Mete Atatüre. Charge-tuneable biexciton complexes in monolayer WSe₂. *Nature Communications*, 9(1):3721, 2018.
- [26] Alexey Chernikov, Claudia Ruppert, Heather M Hill, Albert F Rigosi, and Tony F Heinz. Population inversion and giant bandgap renormalization in atomically thin WS₂ layers. *Nature Photonics*, 9(7):466–470, 2015.
- [27] Kin Fai Mak, Keliang He, Changgu Lee, Gwan Hyoung Lee, James Hone, Tony F Heinz, and Jie Shan. Tightly bound trions in monolayer MoS₂. *Nature Materials*, 12(3):207–211, 2013.
- [28] Jason S Ross, Sanfeng Wu, Hongyi Yu, Nirmal J Ghimire, Aaron M Jones, Grant Aivazian, Jiaqiang Yan, David G Mandrus, Di Xiao, Wang Yao, and Xiaodong Xu. Electrical control of neutral and charged excitons in a monolayer semiconductor. *Nature Communications*, 4(1):1474, 2013.
- [29] Roberto Rosati, Robert Schmidt, Samuel Brem, Raúl Perea-Causín, Iris Niehues, Johannes Kern, Johann A Preuß, Robert Schneider, Stefan Michaelis de Vasconcellos, Rudolf Bratschitsch, and Ermin Malic. Dark exciton anti-funneling in atomically thin semiconductors. *Nature Communications*, 12(1):7221, 2021.
- [30] Roberto Rosati, Ioannis Paradisanos, Libai Huang, Ziyang Gan, Antony George, Kenji Watanabe, Takashi Taniguchi, Laurent Lombez,

- Pierre Renucci, Andrey Turchanin, Bernhard Urbaszek, and Ermin Malic. Interface engineering of charge-transfer excitons in 2d lateral heterostructures. *Nature Communications*, 14(1):2438, 2023.
- [31] Ermin Malic, Raul Perea-Causin, Roberto Rosati, Daniel Erkensten, and Samuel Brem. Exciton transport in atomically thin semiconductors. *Nature Communications*, 2023.
- [32] Daniele Sanvitto, Fabio Pulizzi, Andrew J Shields, Peter CM Christensen, Stuart N Holmes, Michelle Y Simmons, David A Ritchie, Jan C Maan, and Michael Pepper. Observation of charge transport by negatively charged excitons. *Science*, 294(5543):837–839, 2001.
- [33] Guanghui Cheng, Baikui Li, Zijing Jin, Meng Zhang, and Jiannong Wang. Observation of diffusion and drift of the negative trions in monolayer WS₂. *Nano Letters*, 21(14):6314–6320, 2021.
- [34] Ermin Malic and Andreas Knorr. *Graphene and carbon nanotubes: ultrafast optics and relaxation dynamics*. John Wiley & Sons, 2013.
- [35] Hartmut Haug and Stephan W Koch. *Quantum theory of the optical and electronic properties of semiconductors*. World Scientific Publishing Company, 2009.
- [36] Wolfgang Nolting and William D Brewer. *Fundamentals of Many-body Physics*. Springer, 2008.
- [37] Mackillo Kira and Stephan W Koch. *Semiconductor quantum optics*. Cambridge University Press, 2011.
- [38] Gerald D Mahan. *Many-Particle Physics*. Springer US, 2000.
- [39] Walter Kohn and Lu Jeu Sham. Self-consistent equations including exchange and correlation effects. *Physical Review*, 140(4A):A1133, 1965.
- [40] Andor Kormányos, Guido Burkard, Martin Gmitra, Jaroslav Fabian, Viktor Zólyomi, Neil D Drummond, and Vladimir Fal’ko. $k \cdot p$ theory for two-dimensional transition metal dichalcogenide semiconductors. *2D Materials*, 2(2):022001, 2015.

- [41] Paolo Giannozzi, Stefano De Gironcoli, Pasquale Pavone, and Stefano Baroni. Ab initio calculation of phonon dispersions in semiconductors. *Physical Review B*, 43(9):7231, 1991.
- [42] Alejandro Molina-Sanchez and Ludger Wirtz. Phonons in single-layer and few-layer MoS₂ and WS₂. *Physical Review B*, 84(15):155413, 2011.
- [43] Zhenghe Jin, Xiaodong Li, Jeffrey T Mullen, and Ki Wook Kim. Intrinsic transport properties of electrons and holes in monolayer transition-metal dichalcogenides. *Physical Review B*, 90(4):045422, 2014.
- [44] Marlan O Scully and M Suhail Zubairy. Quantum optics, 1999.
- [45] Hongyi Yu, Gui-Bin Liu, Pu Gong, Xiaodong Xu, and Wang Yao. Dirac cones and dirac saddle points of bright excitons in monolayer transition metal dichalcogenides. *Nature Communications*, 5(1):1–7, 2014.
- [46] Diana Y Qiu, Ting Cao, and Steven G Louie. Nonanalyticity, valley quantum phases, and lightlike exciton dispersion in monolayer transition metal dichalcogenides: Theory and first-principles calculations. *Physical Review Letters*, 115(17):176801, 2015.
- [47] Pierluigi Cudazzo, Ilya V Tokatly, and Angel Rubio. Dielectric screening in two-dimensional insulators: Implications for excitonic and impurity states in graphane. *Physical Review B*, 84(8):085406, 2011.
- [48] N S. Rytova. The screened potential of a point charge in a thin film. *Moscow University Physics Bulletin*, 3(3):18, 1967.
- [49] L. V. Keldysh. Coulomb interaction in thin semiconductor and semimetal films. *Soviet Journal of Experimental and Theoretical Physics Letters*, 29:658, June 1979.
- [50] Samuel Brem, Jonas Zipfel, Malte Selig, Archana Raja, Lutz Waldecker, Jonas D Ziegler, Takashi Taniguchi, Kenji Watanabe, Alexey Chernikov, and Ermin Malic. Intrinsic lifetime of higher excitonic states in tungsten diselenide monolayers. *Nanoscale*, 11(25):12381–12387, 2019.
- [51] Kristen Kaasbjerg, Kristian S Thygesen, and Karsten W Jacobsen. Phonon-limited mobility in n-type single-layer MoS₂ from first principles. *Physical Review B*, 85(11):115317, 2012.

- [52] Wang Yao, Di Xiao, and Qian Niu. Valley-dependent optoelectronics from inversion symmetry breaking. *Physical Review B*, 77(23):235406, 2008.
- [53] Timothy C Berkelbach, Mark S Hybertsen, and David R Reichman. Bright and dark singlet excitons via linear and two-photon spectroscopy in monolayer transition-metal dichalcogenides. *Physical Review B*, 92(8):085413, 2015.
- [54] Ting Cao, Gang Wang, Wenpeng Han, Huiqi Ye, Chuanrui Zhu, Junren Shi, Qian Niu, Pingheng Tan, Enge Wang, Baoli Liu, and Ji Feng. Valley-selective circular dichroism of monolayer molybdenum disulfide. *Nature Communications*, 3(1):1–5, 2012.
- [55] John R Schaibley, Hongyi Yu, Genevieve Clark, Pasqual Rivera, Jason S Ross, Kyle L Seyler, Wang Yao, and Xiaodong Xu. Valleytronics in 2d materials. *Nature Reviews Materials*, 1(11):1–15, 2016.
- [56] M Kira, F Jahnke, and SW Koch. Microscopic theory of excitonic signatures in semiconductor photoluminescence. *Physical Review Letters*, 81(15):3263, 1998.
- [57] M Lindberg and Stephan W Koch. Effective bloch equations for semiconductors. *Physical Review B*, 38(5):3342, 1988.
- [58] Mackillo Kira and Stephan W Koch. Many-body correlations and excitonic effects in semiconductor spectroscopy. *Progress in Quantum Electronics*, 30(5):155–296, 2006.
- [59] A Esser, R Zimmermann, and E Runge. Theory of trion spectra in semiconductor nanostructures. *physica status solidi (b)*, 227(2):317–330, 2001.
- [60] Matthias Florian, Malte Hartmann, Alexander Steinhoff, Julian Klein, Alexander W Holleitner, Jonathan J Finley, Tim O Wehling, Michael Kaniber, and Christopher Gies. The dielectric impact of layer distances on exciton and trion binding energies in van der Waals heterostructures. *Nano Letters*, 18(4):2725–2732, 2018.

- [61] Florian Katsch and Andreas Knorr. Excitonic theory of doping-dependent optical response in atomically thin semiconductors. *Physical Review B*, 105(4):045301, 2022.
- [62] Hartmut Haug and Stefan Schmitt-Rink. Electron theory of the optical properties of laser-excited semiconductors. *Progress in Quantum Electronics*, 9(1):3–100, 1984.
- [63] AL Ivanov and H Haug. Self-consistent theory of the biexciton optical nonlinearity. *Physical Review B*, 48(3):1490, 1993.
- [64] Florian Katsch, Malte Selig, Alexander Carmele, and Andreas Knorr. Theory of exciton–exciton interactions in monolayer transition metal dichalcogenides. *physica status solidi (b)*, 255(12):1800185, 2018.
- [65] Tomasz Jakubczyk, Valentin Delmonte, Maciej Koperski, Karol Nogajewski, Clément Faugeras, Wolfgang Langbein, Marek Potemski, and Jacek Kasprzak. Radiatively limited dephasing and exciton dynamics in MoSe₂ monolayers revealed with four-wave mixing microscopy. *Nano Letters*, 16(9):5333–5339, 2016.
- [66] Malte Selig, Gunnar Berghäuser, Archana Raja, Philipp Nagler, Christian Schüller, Tony F Heinz, Tobias Korn, Alexey Chernikov, Ermin Malic, and Andreas Knorr. Excitonic linewidth and coherence lifetime in monolayer transition metal dichalcogenides. *Nature Communications*, 7(1):1–6, 2016.
- [67] Jens Lindhard. On the properties of a gas of charged particles. *Kgl. Danske Videnskab. Selskab Mat.-fys. Medd.*, 28:8, 1954.
- [68] Frank Stern. Polarizability of a two-dimensional electron gas. *Physical Review Letters*, 18(14):546, 1967.
- [69] Mikhail M Glazov and Alexey Chernikov. Breakdown of the static approximation for free carrier screening of excitons in monolayer semiconductors. *physica status solidi (b)*, 255(12):1800216, 2018.
- [70] G Röpke and R Der. The influence of two-particle states (excitons) on the dielectric function of the electron—hole plasma. *physica status solidi (b)*, 92(2):501–510, 1979.

- [71] Alexander Steinhoff, Matthias Florian, Malte Rösner, Gunnar Schönhoff, Tim Oliver Wehling, and Frank Jahnke. Exciton fission in monolayer transition metal dichalcogenide semiconductors. *Nature Communications*, 8(1):1166, 2017.
- [72] Lars Hedin. New method for calculating the one-particle green’s function with application to the electron-gas problem. *Physical Review*, 139(3A):A796, 1965.
- [73] Dmitry K Efimkin and Allan H MacDonald. Many-body theory of trion absorption features in two-dimensional semiconductors. *Physical Review B*, 95(3):035417, 2017.
- [74] Meinrad Sidler, Patrick Back, Ovidiu Cotlet, Ajit Srivastava, Thomas Fink, Martin Kroner, Eugene Demler, and Atac Imamoglu. Fermi polaron-polaritons in charge-tunable atomically thin semiconductors. *Nature Physics*, 13(3):255–261, 2017.
- [75] Mikhail M Glazov. Optical properties of charged excitons in two-dimensional semiconductors. *The Journal of Chemical Physics*, 153(3):034703, 2020.
- [76] Atac Imamoglu, Ovidiu Cotlet, and Richard Schmidt. Exciton-polarons in two-dimensional semiconductors and the tavis-cummings model. *Comptes Rendus. Physique*, 22(S4):1–8, 2021.
- [77] Raül Perea-Causín, Samuel Brem, and Ermin Malic. Microscopic modeling of pump-probe spectroscopy and population inversion in transition metal dichalcogenides. *physica status solidi (b)*, 257(12):2000223, 2020.
- [78] E. J. Sie, A. Steinhoff, C. Gies, C. H. Lui, Q. Ma, M. Rösner, G. Schönhoff, F. Jahnke, T. O. Wehling, Y.-H. Lee, J. Kong, P. Jarillo-Herrero, and N. Gedik. Observation of exciton redshift-blueshift crossover in monolayer WS₂. *Nano Letters*, 17(7):4210–4216, 2017.
- [79] Samuel Brem. *Microscopic theory of exciton dynamics in two-dimensional materials*. PhD thesis, Chalmers Tekniska Hogskola (Sweden), 2020.

- [80] Gang Wang, Cédric Robert, Mikhail M Glazov, Fabian Cadiz, Emmanuel Courtade, Thierry Amand, Delphine Lagarde, Takashi Taniguchi, Kenji Watanabe, Bernhard Urbaszek, and Xavier Marie. In-plane propagation of light in transition metal dichalcogenide monolayers: optical selection rules. *Physical Review Letters*, 119(4):047401, 2017.
- [81] Yang Song and Hanan Dery. Transport theory of monolayer transition-metal dichalcogenides through symmetry. *Physical Review Letters*, 111(2):026601, 2013.
- [82] Roberto Rosati, Koloman Wagner, Samuel Brem, Raul Perea-Causin, Edith Wietek, Jonas Zipfel, Jonas D Ziegler, Malte Selig, Takashi Taniguchi, Kenji Watanabe, Andreas Knorr, Alexey Chernikov, and Ermin Malic. Temporal evolution of low-temperature phonon sidebands in transition metal dichalcogenides. *ACS Photonics*, 7(10):2756–2764, 2020.
- [83] Samuel Brem, August Ekman, Dominik Christiansen, Florian Katsch, Malte Selig, Cedric Robert, Xavier Marie, Bernhard Urbaszek, Andreas Knorr, and Ermin Malic. Phonon-assisted photoluminescence from indirect excitons in monolayers of transition-metal dichalcogenides. *Nano Letters*, 20(4):2849–2856, 2020.
- [84] Malte Selig, Gunnar Berghäuser, Marten Richter, Rudolf Bratschitsch, Andreas Knorr, and Ermin Malic. Dark and bright exciton formation, thermalization, and photoluminescence in monolayer transition metal dichalcogenides. *2D Materials*, 5(3):035017, 2018.
- [85] Xiao-Xiao Zhang, Yumeng You, Shu Yang Frank Zhao, and Tony F Heinz. Experimental evidence for dark excitons in monolayer WSe₂. *Physical Review Letters*, 115(25):257403, 2015.
- [86] Robert Wallauer, Raul Perea-Causin, Lasse Münster, Sarah Zajusch, Samuel Brem, Jens Gütde, Katsumi Tanimura, Kai-Qiang Lin, Rupert Huber, Ermin Malic, and Ulrich Höfer. Momentum-resolved observation of exciton formation dynamics in monolayer WS₂. *Nano Letters*, 21(13):5867–5873, 2021.

- [87] Julien Madéo, Michael K. L. Man, Chakradhar Sahoo, Marshall Campbell, Vivek Pareek, E. Laine Wong, Abdullah Al-Mahboob, Nicholas S. Chan, Arka Karmakar, Bala Murali Krishna Mariserla, Xiaoqin Li, Tony F. Heinz, Ting Cao, and Keshav M. Dani. Directly visualizing the momentum-forbidden dark excitons and their dynamics in atomically thin semiconductors. *Science*, 370(6521):1199–1204, 2020.
- [88] Mathieu Massicotte, Fabien Violla, Peter Schmidt, Mark B Lundeberg, Simone Latini, Sten Haastrup, Mark Danovich, Diana Davydovskaya, Kenji Watanabe, Takashi Taniguchi, Vladimir I. Fal’ko, Kristian S. Thygesen, Thomas G. Pedersen, and Frank H. L. Koppens. Dissociation of two-dimensional excitons in monolayer WSe₂. *Nature Communications*, 9(1):1–7, 2018.
- [89] Sten Haastrup, Simone Latini, Kirill Bolotin, and Kristian S Thygesen. Stark shift and electric-field-induced dissociation of excitons in monolayer MoS₂ and h-BN/MoS₂ heterostructures. *Physical Review B*, 94(4):041401, 2016.
- [90] Høgni C Kamban and Thomas G Pedersen. Field-induced dissociation of two-dimensional excitons in transition metal dichalcogenides. *Physical Review B*, 100(4):045307, 2019.
- [91] RJ Elliott. Intensity of optical absorption by excitons. *Physical Review*, 108(6):1384, 1957.
- [92] Masaki Shinada and Satoru Sugano. Interband optical transitions in extremely anisotropic semiconductors. I. Bound and unbound exciton absorption. *Journal of the Physical Society of Japan*, 21(10):1936–1946, 1966.
- [93] HC Schneider, WW Chow, and SW Koch. Many-body effects in the gain spectra of highly excited quantum-dot lasers. *Physical Review B*, 64(11):115315, 2001.
- [94] Raül Perea-Causín, Samuel Brem, and Ermin Malic. Phonon-assisted exciton dissociation in transition metal dichalcogenides. *Nanoscale*, 13(3):1884–1892, 2021.
- [95] Jonas Zipfel, Marvin Kulig, Raül Perea-Causín, Samuel Brem, Jonas D. Ziegler, Roberto Rosati, Takashi Taniguchi, Kenji Watanabe,

- Mikhail M. Glazov, Ermin Malic, and Alexey Chernikov. Exciton diffusion in monolayer semiconductors with suppressed disorder. *Physical Review B*, 101(11):115430, 2020.
- [96] JB Mock, GA Thomas, and M Combescot. Entropy ionization of an exciton gas. *Solid State Communications*, 25(5):279–282, 1978.
- [97] Meghnad Saha and BN Srivastava. Treatise on heat. 1935.
- [98] Zahra Khatibi, Maja Feierabend, Malte Selig, Samuel Brem, Christopher Linderälv, Paul Erhart, and Ermin Malic. Impact of strain on the excitonic linewidth in transition metal dichalcogenides. *2D Materials*, 6(1):015015, 2018.
- [99] José E Moyal. Quantum mechanics as a statistical theory. In *Mathematical Proceedings of the Cambridge Philosophical Society*, volume 45, pages 99–124. Cambridge University Press, 1949.
- [100] Ortwin Hess and Tilmann Kuhn. Maxwell-Bloch equations for spatially inhomogeneous semiconductor lasers. I. Theoretical formulation. *Physical Review A*, 54(4):3347, 1996.
- [101] Roberto Rosati and Fausto Rossi. Scattering nonlocality in quantum charge transport: Application to semiconductor nanostructures. *Physical Review B*, 89(20):205415, 2014.
- [102] Marvin Kulig, Jonas Zipfel, Philipp Nagler, Sofia Blanter, Christian Schüller, Tobias Korn, Nicola Paradiso, Mikhail M Glazov, and Alexey Chernikov. Exciton diffusion and halo effects in monolayer semiconductors. *Physical Review Letters*, 120(20):207401, 2018.
- [103] F. Cadiz, C. Robert, E. Courtade, M. Manca, L. Martinelli, T. Taniguchi, K. Watanabe, T. Amand, A. C. H. Rowe, D. Paget, B. Urbaszek, and X. Marie. Exciton diffusion in WSe₂ monolayers embedded in a van der Waals heterostructure. *Applied Physics Letters*, 112(15):152106, 2018.
- [104] Shinichiro Mouri, Yuhei Miyauchi, Minglin Toh, Weijie Zhao, Goki Eda, and Kazunari Matsuda. Nonlinear photoluminescence in atomically thin layered WSe₂ arising from diffusion-assisted exciton-exciton annihilation. *Physical Review B*, 90(15):155449, 2014.

- [105] Long Yuan, Ti Wang, Tong Zhu, Mingwei Zhou, and Libai Huang. Exciton dynamics, transport, and annihilation in atomically thin two-dimensional semiconductors. *The Journal of Physical Chemistry Letters*, 8(14):3371–3379, 2017.
- [106] Raul Perea-Causin, Samuel Brem, Roberto Rosati, Roland Jago, Marvin Kulig, Jonas D Ziegler, Jonas Zipfel, Alexey Chernikov, and Ermin Malic. Exciton propagation and halo formation in two-dimensional materials. *Nano Letters*, 19(10):7317–7323, 2019.
- [107] E. Courtade, M. Semina, M. Manca, M. M. Glazov, C. Robert, F. Cadiz, G. Wang, T. Taniguchi, K. Watanabe, M. Pierre, W. Escoffier, E. L. Ivchenko, P. Renucci, X. Marie, T. Amand, and B. Urbaszek. Charged excitons in monolayer WSe₂: Experiment and theory. *Physical Review B*, 96(8):085302, 2017.
- [108] Raul Perea-Causin, Samuel Brem, and Ermin Malic. Trion-phonon interaction in atomically thin semiconductors. *Physical Review B*, 106(11):115407, 2022.
- [109] Dmitry K Efimkin, Emma K Laird, Jesper Levinsen, Meera M Parish, and Allan H MacDonald. Electron-exciton interactions in the exciton-polaron problem. *Physical Review B*, 103(7):075417, 2021.
- [110] Christian Fey, Peter Schmelcher, Atac Imamoglu, and Richard Schmidt. Theory of exciton-electron scattering in atomically thin semiconductors. *Physical Review B*, 101(19):195417, 2020.
- [111] Dinh Van Tuan, Min Yang, and Hanan Dery. Coulomb interaction in monolayer transition-metal dichalcogenides. *Physical Review B*, 98(12):125308, 2018.
- [112] Ashish Arora, Thorsten Deilmann, Till Reichenauer, Johannes Kern, Steffen Michaelis de Vasconcellos, Michael Rohlfing, and Rudolf Bratschkitsch. Excited-state trions in monolayer WS₂. *Physical Review Letters*, 123(16):167401, 2019.
- [113] Koloman Wagner, Edith Wietek, Jonas D Ziegler, Marina A Semina, Takashi Taniguchi, Kenji Watanabe, Jonas Zipfel, Mikhail M Glazov,

- and Alexey Chernikov. Autoionization and dressing of excited excitons by free carriers in monolayer WSe₂. *Physical Review Letters*, 125(26):267401, 2020.
- [114] Thomas Goldstein, Yueh-Chun Wu, Shao-Yu Chen, Takashi Taniguchi, Kenji Watanabe, Kalman Varga, and Jun Yan. Ground and excited state exciton polarons in monolayer MoSe₂. *The Journal of Chemical Physics*, 153(7):071101, 2020.
 - [115] Erfu Liu, Jeremiah van Baren, Zhengguang Lu, Takashi Taniguchi, Kenji Watanabe, Dmitry Smirnov, Yia-Chung Chang, and Chun Hung Lui. Exciton-polaron Rydberg states in monolayer MoSe₂ and WSe₂. *Nature Communications*, 12(1):6131, 2021.
 - [116] Kristen Kaasbjerg, KS Bhargavi, and SS Kubakaddi. Hot-electron cooling by acoustic and optical phonons in monolayers of MoS₂ and other transition-metal dichalcogenides. *Physical Review B*, 90(16):165436, 2014.
 - [117] Takato Hotta, Shohei Higuchi, Akihiro Ueda, Keisuke Shinokita, Yuhei Miyauchi, Kazunari Matsuda, Keiji Ueno, Takashi Taniguchi, Kenji Watanabe, and Ryo Kitaura. Exciton diffusion in h bn-encapsulated monolayer MoSe₂. *Physical Review B*, 102(11):115424, 2020.
 - [118] Bumho Kim, Yue Luo, Daniel Rhodes, Yusong Bai, Jue Wang, Song Liu, Abraham Jordan, Baili Huang, Zhaochen Li, Takashi Taniguchi, Kenji Watanabe, Jonathan Owen, Stefan Strauf, Katayun Barmak, Xiaoyang Zhu, and James Hone. Free trions with near-unity quantum yield in monolayer MoSe₂. *ACS Nano*, 16(1):140–147, 2022.
 - [119] Axel Esser, Erich Runge, Roland Zimmermann, and Wolfgang Langbein. Photoluminescence and radiative lifetime of trions in GaAs quantum wells. *Physical Review B*, 62(12):8232, 2000.
 - [120] Jonas Zipfel, Koloman Wagner, Marina A Semina, Jonas D Ziegler, Takashi Taniguchi, Kenji Watanabe, Mikhail M Glazov, and Alexey Chernikov. Electron recoil effect in electrically tunable MoSe₂ monolayers. *Physical Review B*, 105(7):075311, 2022.
 - [121] Minhao He, Pasqual Rivera, Dinh Van Tuan, Nathan P Wilson, Min Yang, Takashi Taniguchi, Kenji Watanabe, Jiaqiang Yan, David G

- Mandrus, Hongyi Yu, Hanan Dery, Wang Yao, and Xiaodong Xu. Valley phonons and exciton complexes in a monolayer semiconductor. *Nature Communications*, 11(1):618, 2020.
- [122] Jonathan Förste, Nikita V Tepliakov, Stanislav Yu Kruchinin, Jessica Lindlau, Victor Funk, Michael Förg, Kenji Watanabe, Takashi Taniguchi, Anvar S Baimuratov, and Alexander Högele. Exciton g-factors in monolayer and bilayer WSe₂ from experiment and theory. *Nature Communications*, 11(1):4539, 2020.
- [123] Thorsten Deilmann and Kristian Sommer Thygesen. Dark excitations in monolayer transition metal dichalcogenides. *Physical Review B*, 96(20):201113, 2017.
- [124] Erfu Liu, Jeremiah van Baren, Zhengguang Lu, Mashael M Altairy, Takashi Taniguchi, Kenji Watanabe, Dmitry Smirnov, and Chun Hung Lui. Gate tunable dark trions in monolayer WSe₂. *Physical Review Letters*, 123(2):027401, 2019.
- [125] Zhipeng Li, Tianmeng Wang, Zhengguang Lu, Mandeep Khatoniar, Zhen Lian, Yuze Meng, Mark Blei, Takashi Taniguchi, Kenji Watanabe, Stephen A. McGill, Sefaattin Tongay, Vinod M. Menon, Dmitry Smirnov, and Su-Fei Shi. Direct observation of gate-tunable dark trions in monolayer WSe₂. *Nano Letters*, 19(10):6886–6893, 2019.
- [126] Timothy C Berkelbach, Mark S Hybertsen, and David R Reichman. Theory of neutral and charged excitons in monolayer transition metal dichalcogenides. *Physical Review B*, 88(4):045318, 2013.
- [127] S Chandrasekhar. Some remarks on the negative hydrogen ion and its absorption coefficient. *Astrophysical journal*, 100:176–180, 1944.
- [128] Maja Feierabend, Alexandre Morlet, Gunnar Berghäuser, and Ermin Malic. Impact of strain on the optical fingerprint of monolayer transition-metal dichalcogenides. *Physical Review B*, 96(4):045425, 2017.
- [129] Di Huang, Kevin Sampson, Yue Ni, Zhida Liu, Danfu Liang, Kenji Watanabe, Takashi Taniguchi, Hebin Li, Eric Martin, Jesper Levinsen, Meera M. Parish, Emanuel Tutuc, Dmitry K. Efimkin, and Xiaoqin

- Li. Quantum dynamics of attractive and repulsive polarons in a doped MoSe₂ monolayer. *Physical Review X*, 13:011029, Mar 2023.
- [130] Koloman Wagner, Zakhar A Iakovlev, Jonas D Ziegler, Marzia Cuccu, Takashi Taniguchi, Kenji Watanabe, Mikhail M Glazov, and Alexey Chernikov. Diffusion of excitons in a two-dimensional fermi sea of free charges. *Nano Letters*, 2023.
- [131] Evgeny M Alexeev, David A Ruiz-Tijerina, Mark Danovich, Matthew J Hamer, Daniel J Terry, Pramoda K Nayak, Seongjoon Ahn, Sangyeon Pak, Juwon Lee, Jung Inn Sohn, Maciej R. Molas, Maciej Koperski, Kenji Watanabe, Takashi Taniguchi, Kostya S. Novoselov, Roman V. Gorbachev, Hyeon Suk Shin, Vladimir I. Fal’ko, and Alexander I. Tartakovskii. Resonantly hybridized excitons in moiré superlattices in van der Waals heterostructures. *Nature*, 567(7746):81–86, 2019.
- [132] Philipp Merkl, Fabian Mooshammer, Philipp Steinleitner, Anna Girnghuber, K-Q Lin, Philipp Nagler, Johannes Holler, Christian Schüller, John M Lupton, Tobias Korn, Simon Ovesen, Samuel Brem, Ermin Malic, and Rupert Huber. Ultrafast transition between exciton phases in van der Waals heterostructures. *Nature Materials*, 18(7):691–696, 2019.
- [133] Samuel Brem, Kai-Qiang Lin, Roland Gillen, Jonas M Bauer, Janina Maultzsch, John M Lupton, and Ermin Malic. Hybridized intervalley moiré excitons and flat bands in twisted WSe₂ bilayers. *Nanoscale*, 12(20):11088–11094, 2020.
- [134] Ido Schwartz, Yuya Shimazaki, Clemens Kuhlenkamp, Kenji Watanabe, Takashi Taniguchi, Martin Kroner, and Ataç Imamoglu. Electrically tunable feshbach resonances in twisted bilayer semiconductors. *Science*, 374(6565):336–340, 2021.
- [135] David Schmitt, Jan Philipp Bange, Wiebke Bennecke, AbdulAziz Al-Mutairi, Giuseppe Meneghini, Kenji Watanabe, Takashi Taniguchi, Daniel Steil, D Russell Luke, R Thomas Weitz, Sabine Steil, G. S. Matthijs Jansen, Samuel Brem, Ermin Malic, Stephan Hofmann, Marcel Reutzel, and Stefan Mathias. Formation of moiré interlayer excitons in space and time. *Nature*, 608(7923):499–503, 2022.

- [136] Fedele Tagarelli, Edoardo Lopriore, Daniel Erkensten, Raül Perea-Causín, Samuel Brem, Joakim Hagel, Zhe Sun, Gabriele Pasquale, Kenji Watanabe, Takashi Taniguchi, Ermin Malic, and Andras Kis. Electrical control of hybrid exciton transport in a van der Waals heterostructure. *Nature Photonics*, pages 1–7, 2023.
- [137] Jue Wang, Qianhui Shi, En-Min Shih, Lin Zhou, Wenjing Wu, Yuesong Bai, Daniel Rhodes, Katayun Barmak, James Hone, Cory R. Dean, and X.-Y. Zhu. Diffusivity reveals three distinct phases of interlayer excitons in $\text{MoSe}_2/\text{WSe}_2$ heterobilayers. *Physical Review Letters*, 126(10):106804, 2021.
- [138] Mit H Naik, Emma C Regan, Zuocheng Zhang, Yang-Hao Chan, Zhenglu Li, Danqing Wang, Yoseob Yoon, Chin Shen Ong, Wenyu Zhao, Sihan Zhao, M. Iqbal Bakti Utama, Beini Gao, Xin Wei, Mohammed Sayyad, Kentaro Yumigeta, Kenji Watanabe, Takashi Taniguchi, Sefaattin Tongay, Felipe H. da Jornada, Feng Wang, and Steven G. Louie. Intralayer charge-transfer moiré excitons in van der Waals superlattices. *Nature*, 609(7925):52–57, 2022.
- [139] Fengcheng Wu, Timothy Lovorn, Emanuel Tutuc, and Allan H MacDonald. Hubbard model physics in transition metal dichalcogenide moiré bands. *Physical Review Letters*, 121(2):026402, 2018.
- [140] Yanhao Tang, Lizhong Li, Tingxin Li, Yang Xu, Song Liu, Katayun Barmak, Kenji Watanabe, Takashi Taniguchi, Allan H MacDonald, Jie Shan, and Kin Fai Mak. Simulation of hubbard model physics in WSe_2/WS_2 moiré superlattices. *Nature*, 579(7799):353–358, 2020.
- [141] Kin Fai Mak and Jie Shan. Semiconductor moiré materials. *Nature Nanotechnology*, 17(7):686–695, 2022.
- [142] Yuya Shimazaki, Ido Schwartz, Kenji Watanabe, Takashi Taniguchi, Martin Kroner, and Ataç Imamoğlu. Strongly correlated electrons and hybrid excitons in a moiré heterostructure. *Nature*, 580(7804):472–477, 2020.
- [143] Yihang Zeng, Zhengchao Xia, Roei Dery, Kenji Watanabe, Takashi Taniguchi, Jie Shan, and Kin Fai Mak. Exciton density waves in Coulomb-coupled dual moiré lattices. *Nature Materials*, pages 1–5, 2023.

